A Study of the Effects of Position Resolution and Energy Resolution on Compton Imaging using a Single Planar Strip Detector

Thesis submitted in accordance with the requirements of the University of Liverpool for the degree of Doctor in Philosophy

by

Jonathan Paul Wright

Department of Physics
University of Liverpool
United Kingdom

November 2016

Acknowledgements

I owe my thanks to my supervisory team of Drs. Andy Boston and Eddie Paul for their continued support and guidance throughout my PhD.

I would also like to thank Drs. Carl Unsworth and Samantha Colosimo for their helpful discussions regarding ADL and general support in the lab.

Thank you to those who proof read this thesis and provided helpful feedback including Drs. Andy Boston, Laura Harkness-Brennan and Dan Judson.

Thank you to all members of the nuclear physics group, past and present, without whom this experience would have been a lot less entertaining and enjoyable.

Finally, thanks go out to my family for always being there when I needed them, no matter how infrequently I called home. I promise that I'll get a real job one day. Special mentions to Sophie Lewis, you've been with me throughout this whole process, always supporting me no matter what the problem.

Contents

List of Figures

List of Tables

Abstract

The feasibility of single element Compton imaging using a Double Sided Germanium Strip Detector (DSGSD) has been investigated, with potential use in assisting particle identification as part of Phase III DEGAS at DESPEC in mind. DEGAS is a proposed high-purity germanium tracking array for use in the DEcay SPECtroscopy (DESPEC) experiment at FAIR. The concept of γ-ray tracking within a DSGSD has been proved viable, with Compton images reconstructed from partial energy depositions within the detector volume. Using the raw positional information provided by the segmentation of the detector, initial source locations were unable to be resolved, with the resulting image displaying multiple 'hotspots' resulting from the selection criteria imposed. The causes of these features have been explored and explained in terms of scattering angles using the simulation package GAMOS.

The effects of Pulse Shape Analysis, as a means of improving position sensitivity, have also been investigated, using a simulated database in conjunction with a grid search algorithm. Detailed electric field simulations were created, enabling a simulated pulse shape database to be generated using the ADL software package. Experimental data were sorted to locate potential Compton events, with charge pulses for each events stored using a digital electronics setup. Experimental pulses were compared to pulses from the simulated database using a FoM minimisation grid search algorithm. This improved the position resolution of interactions within the detector, thus improving the effectiveness of the resulting Compton reconstructions. With the application of PSA, initial source positions were located to within $\sim$ 10 mm, with the image resolution found to be of the order $\sim$ 100 mm for a range of initial γ-ray energies. Initial results appear promising, with future work required to improve the efficiency of the method.

Additionally, Monte Carlo simulations have been performed to study the individual contributions of both energy and position resolution on the final reconstructed Compton image. Simulations were performed for three energy resolutions; 0, 3 and 50 keV, with a fixed position resolution of $2 \times 2 \times 10$ mm, in addition to three position resolutions; 1, 2 and 5 mm^3, with a fixed

energy resolution of 5 keV. The results of these showed that the position sensitivity of the detector has a much more significant impact of both the location and resolution of the reconstructed Compton image.

1 Introduction

Nuclear physics is the study of the atomic nucleus and the interactions therein. Although still in its infancy, the impact it has had on the world is astounding. From nuclear power to weaponry to security, the fundamental principles of nuclear physics are present in many aspects of our everyday lives.

Studying something as small as the atomic nucleus, $\sim 10^{-15}$ m, presents many challenges and it should be clear that direct imaging is impossible with current technology. In response to this constraint, indirect measurements have been developed which study the way the nucleus behaves and interacts as a result of a perturbation from its initial configuration. Nuclei in an excited state will always move to reduce their energy and return to the most stable configuration available. This is achieved through processes such as fission, particle or radiation emission and internal conversion. By inducing controlled perturbations to the nuclear system, we can measure the way in which the nucleus returns to stability and thus gain an insight into the internal structure present. In the field of high spin γ-ray spectroscopy, the nucleus is imparted with large amounts of energy and angular momentum. The subsequent decay is via the emission of particles and γ-radiation, which can be measured using detectors constructed using materials such as germanium. A deeper understanding of this is presented in Chapter 2.

The behaviour of nuclei at the extremes of angular momentum remains one of the most intriguing areas of nuclear research. Due to the current collection of nuclear accelerators and high efficiency γ-ray spectrometers, the boundaries of high spin research are constantly being expanded. For decades γ-ray spectroscopy has played a crucial role in developing our understanding of the atomic nucleus. From the first observation of superdeformed bands in ^{152}Dy [1] in 1986, to the more recent results showing evidence for triaxiality in the Lu nuclei, e.g. ^{163}Lu [2]. These experimental results have worked in tandem with theoretical predictions to deepen our understanding of such phenomena. The major driving force behind these discoveries comes from the continuous advances made in developing innovative detector arrays. Figure 1.1 illustrates the history of germanium arrays,

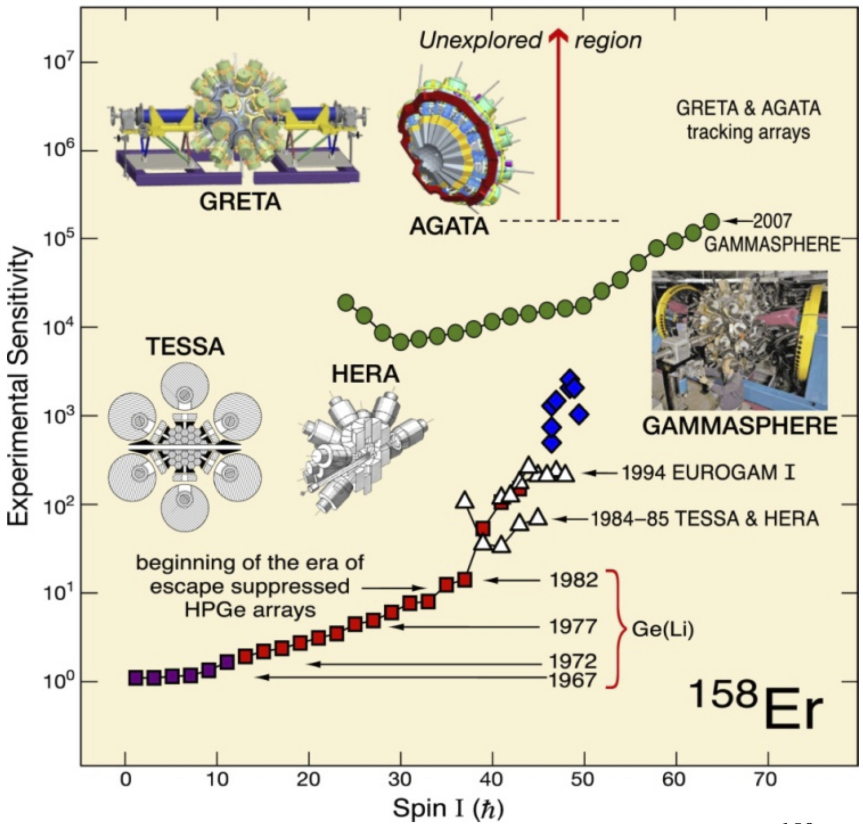

Figure 1.1: Evolution of experimental sensitivity and observed angular momentum as a result of improved detector arrays [3]

demonstrating the ever increasing sensitivity available to researchers with progressive technologies. This increase in sensitivity directly correlates to the observation of weaker states at higher spins.

Future discoveries in γ-ray spectroscopy will require further advances in the field of nuclear instrumentation, with improved detection methods illuminating previously unseen phenomena. Current research focusses on the construction of large 4π Ge tracking arrays such as AGATA (Advanced GAmma Tracking Array) [4] and GRETINA/GRETA (Gamma Ray Energy Tracking Array) [5]. These arrays will be capable of tracking each γ-ray from start to finish, with complex algorithms used to reconstruct the paths taken and reconstruct energies from partial depositions. As with any detector system, its functionality and scope can be significantly expanded through the addition of ancillary detectors.

Recent research has attempted to use the excellent tracking capabilities of

AGATA in combination with a pixelated, planar HPGe detector, for use as a Compton camera. The aim of this research was to reconstruct Compton events originating from exotic nuclei implanted in the implantation detector AIDA (Advanced Implantation Detector Array) at the DESPEC (Decay Spectroscopy) [6] experiment. The reconstructed Compton events would be used to pair recoils in AIDA with γ-rays detected in the Ge array. This was investigated by S. Moon *et al.* at the University of Liverpool in 2011 [7], using an AGATA B-type detector, B009 in conjunction with the SmartPET double sided planar detector [8].

DESPEC is currently under construction for use at FAIR (Facility for Antiproton and Ion Research), GSI Darmstadt, Germany, and is part of the NuSTAR (Nuclear STructure, Astrophysics and Reactions) project. One of the essential components of FAIR will be the Super-FRS (Fragment Recoil Separator) [9], which will be capable of separating exotic beams in-flight enabling the production of relativistic radioactive ion beams for use in nuclear spectroscopy experiments.

One of the major requirements for DESPEC is a germanium spectrometer to pair with AIDA, known as DEGAS (DESPEC Germanium Array Spectrometer). DEGAS [10] was proposed in 2014 and the construction will take place in three phases. Phase I plans to re-use the EUROBALL Cluster detectors, with phase II utilising AGATA-type tracking detectors in place of the EUROBALL Cluster. Detailed simulations for these configurations are presented in [11]. The final phase is not covered in the current funding scheme, however it could be the result of a long term research and development project into planar germanium stack and point contact germanium detectors.

The work presented in this thesis provides a proof of concept for single element Compton imaging using a double sided germanium strip detector. This work can be considered part of the long term research and development required for Phase III of DEGAS. The appeal of this configuration is the reduced size of the system, with the strip detector measuring just $60 \times 60 \times 20$ mm^3.

Chapter 2 provides a detailed look at the physical processes behind the instrumentation used in this work, whilst Chapter 3 presents the theory and processes

required for generating the pulse shape database. The results of the experimental work are presented in Chapter 4 in addition to the discussion and interpretation.

Although experimental nuclear physics provides the driving force for this work, this system also provides features of interest to the nuclear industry. Products capable of locating radioactive sources are of particular interest in the field of nuclear decommissioning. The ability to understand both the energy and location of nuclear waste enables proper analysis of a nuclear site and provides an insight into the most appropriate steps to take.

Two examples of such detectors currently in production are GeGI [12] by PHDS Co and Polaris H [13] by H3D. Both devices provide the user with the ability to image radioactive sources and determine their location in three dimensions. For areas with large quantities of radioactive material, the user is able to specify the specific γ-ray energy they are interested in imaging and the system omits all background. The major difference between the two is in the choice of crystal material, GeGi is made of germanium, with Polaris H being constructed of 3D position sensitive CdZnTe (CZT).

There are two main limitations on the imaging capabilities of both of these systems and also the one discussed in this thesis; energy and position resolution. The energy resolution is largely down to the choice of crystal material used in the system, with the position resolution coming from any segmentation contained within the detector. There are no real methods to significantly alter the energy resolution of a detector, however the position sensitivity can be improved enormously through the use of techniques such as pulse shape analysis. For germanium semiconductors, the position resolution can be improved down to sub 1 mm through the comparison of simulated charge pulses with experimental charge pulses. The contributions of both energy resolution and position resolution on reconstructed Compton images are discussed in Chapter 5.2.

2 Experimental Methods

2.1 Introduction

Nuclear instrumentation plays a crucial role in advancing our understanding of the universe. It is only through advancements in our detection methods that we can study the finer details of nuclear systems. This is best demonstrated by Figure 2.1, illustrating the progression of discoveries made in the rare earth nucleus ^{158}Er as a function of increasing experimental sensitivity. When viewed alongside Figure 1.1, the correlation between advancements in nuclear instrumentation and discoveries in nuclear structure physics is clear to see. With greater experimental sensitivity, the ability to observe and characterise weaker structures in nuclei increases.

Although this plot only demonstrates the significance of detector advancements, there are many other experimental processes that factor into advancing our understanding of nuclear structure. Perhaps the most significant of these is in the development of particle accelerators and ion sources. Accelerator facilities are now capable of providing more focussed, higher purity ion beams with increased energy, intensity and current. Due to these advancements, the potential beam target combinations now available are allowing researchers to explore new and more exciting regions of the nuclear landscape.

This section will cover the physics behind the experimental procedures relevant to the contents of this thesis, along with a detailed presentation of the instrumentation used.

2.2 Interaction of Gamma-rays with Matter

Electromagnetic radiation covers a wide spectrum of energies and frequencies, making the task of detecting it more challenging. The most primitive radiation detector, the human eye, is only sensitive to a small fraction of the spectrum. This biological limit has lead to the necessity to develop technologies that are capable of observing the remainder of the spectrum. Such detectors should produce an output that not only indicates the presence of radiation, but also relates to the

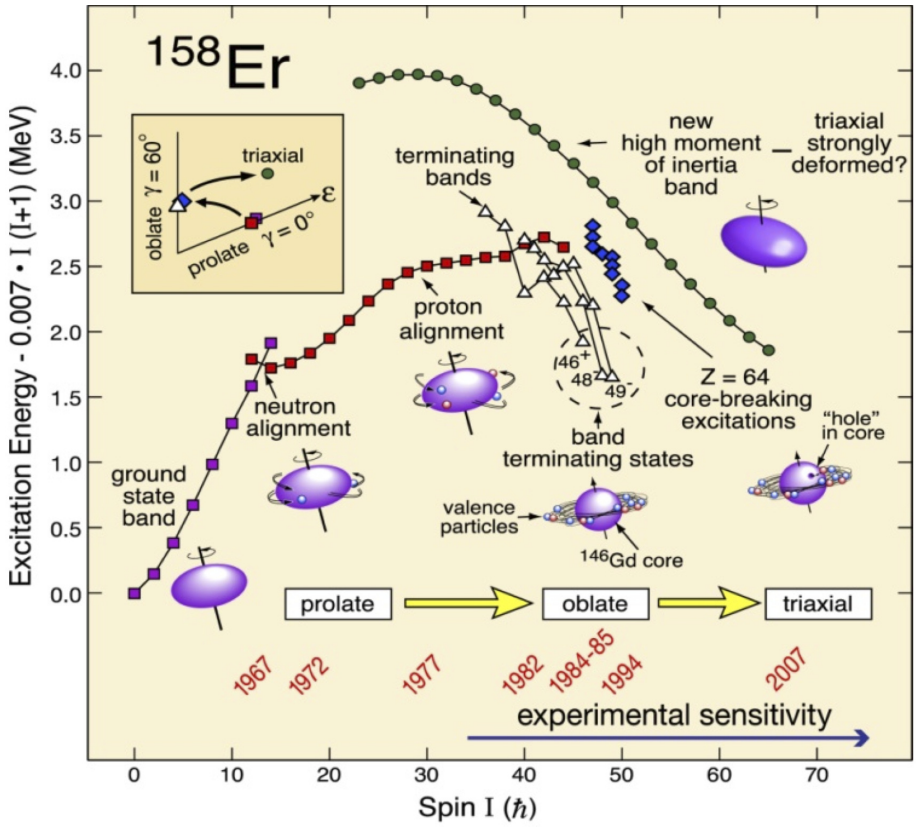

Figure 2.1: Timeline of the significant discoveries in high-spin γ-ray spectroscopy as a function of experimental sensitivity. This increase in sensitivity corresponds to the development of new detector arrays as illustrated in Figure 1.1 [3]

energy of the incoming radiation. To develop such technologies requires a thorough understanding of the methods through which radiation interacts with matter.

The internal structure of a nucleus is a complex environment, presenting a challenge for anyone interested in exploring it. The standard way to approach this is to perturb the nucleus in a controlled manner and observe the aftermath. Since γ-radiation is associated with nuclear transitions, it is crucial that we are capable of detecting it efficiently. There are many mechanisms through which γ-radiation interacts with matter, however three dominate over the remainder; photoelectric absorption, Compton scattering and pair production. The probability for each of these interactions varies dramatically with γ-ray energy and the atomic mass of the absorbing material. This is demonstrated by Figure 2.2, which illustrates the dominant interaction as a function of both energy and atomic number. From the plot it can be seen that both photoelectric absorption (lower energy) and pair production (higher energy) become more favoured Z increases, with Compton scattering being more dominant for low Z nuclei. The plot also highlights the line for $Z = 32$ (germanium), showing the boundaries where the dominant interaction changes. From the plot, photoelectric absorption is only dominant below $\sim$ 200 keV with Compton scatter being the most likely interaction up to $\sim$ 8 MeV. For γ-rays above $\sim$ 10 MeV pair production starts to become favoured. The next section will explain each of these interactions and the effect they have on measurements.

2.2.1 Photoelectric Absorption

Photoelectric absorption is the process through which an incoming γ-ray interacts with an electron from a bound atom depositing all of its energy. The absorbed energy is used to free the electron from the atom with any excess energy given to the electron in the form of kinetic energy. The process is very dependent on the energy of the incoming γ-ray, with the ejected electron having a kinetic energy, E_e of

$$E_e = E_\gamma - E_b \tag{1}$$

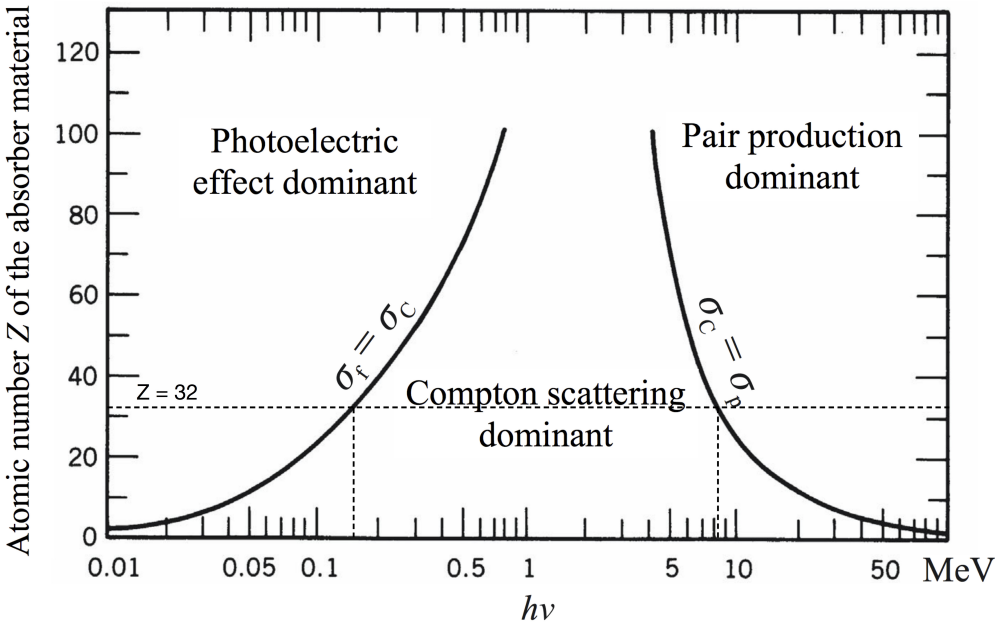

Figure 2.2: Relative importance of the three major forms of γ-ray interaction as a function of γ-ray energy and atomic number, with the boundaries for Z = 32 added. Adapted from reference [14]

where E_γ is the energy of the incoming radiation and E_b is the binding energy of the electron in its atomic shell. The most probable origin of the electron is from the most strongly bound shell, the k-shell. This is due to the proximity of this shell to the nucleus of the atom, with the binding energy for a k-shell electron in germanium being $\sim$ 11 keV.

In addition to the escaped electron, we must also consider the corresponding hole left behind in the now ionised atom. This hole can be filled through one of two methods; the capture of a free electron or electrons falling from outer shells. If by the latter method then x-rays will be generated through this cascading process. These x-rays are subsequently detected by the system and show up as distinct low energy peaks in the resulting energy spectrum.

Photoelectric absorption is the ideal method of interaction due to the full energy of the incoming radiation being absorbed by a single detector crystal. The probability, τ, of a γ-ray interacting in this manner can be roughly estimated as

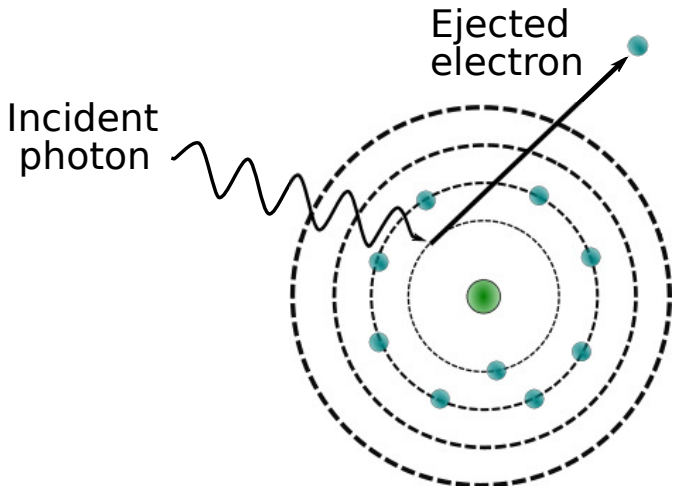

Figure 2.3: Schematic illustration of photoelectric absorption, showing the emission of an electron from the K shell

$$\tau \approx constant \times \frac{Z^n}{E_\gamma^{3.5}} \tag{2}$$

where Z is the atomic mass of the absorber material and the value of n varies between 4 and 5. From this equation it is clear that photoelectric absorption is dominant for γ-rays of low energy. Additionally, it can be seen that increasing the Z of the detector material significantly increases the likelihood of absorption.

2.2.2 Compton Scattering

Compton scattering is the process through which an incident γ-ray scatters off of an electron in the detector material. The photon interacts with a loosely bound electron, scattering through an angle θ and depositing some portion of its energy to the now recoiling electron. Due to the wide range of angles possible for scattering, the energy lost to the recoil electron can vary drastically.

From conservation of energy and momentum, it is possible to calculate the relationship between the incoming photon energy, E_γ, and the scattering angle, θ. The energy of the scattered photon, E', is given by

$$E' = \frac{E_\gamma}{1 + \frac{E_\gamma}{m_0 c^2}(1 - \cos\theta)} \tag{3}$$

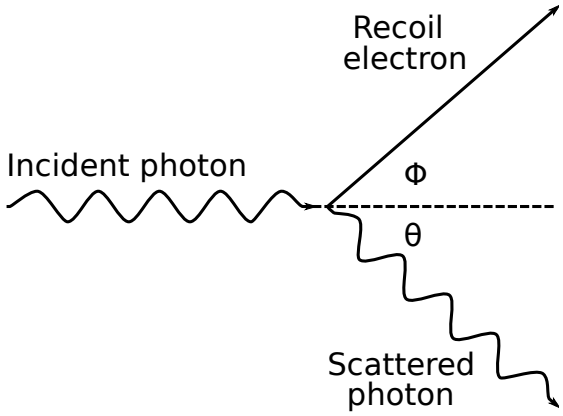

Figure 2.4: Schematic illustration of the Compton scattering interaction, illustrating the paths of both the scattered photon and ejected electrons

where m_0c^2 is the rest mass energy of the electron (511 keV). The ejected electron will have a corresponding energy

$$E_e = E_\gamma - E' = E_\gamma \left[1 - \frac{1}{1 + \frac{E_\gamma}{m_0 c^2}(1 - cos\theta)} \right] \tag{4}$$

It is worth noting that although it is possible for zero energy to be transferred to the electron, when $\theta = 0°$, it is not possible for all of the incoming energy to be passed to the recoil. Even for a scattering angle of $\theta = 180°$, the scattered photon will still have energy, $E' = \hbar\nu/(1 + 2\hbar\nu/m_0c^2)$.

It should be evident that due to the vast range of energies possible, it becomes very difficult to distinguish Compton events from background radiation. Methods have been developed to reduce these events such as Compton suppression systems which will be discussed later in Section **??**.

Compton scattering is the dominant interaction for photons in the intermediate energy range $\sim$ 200 keV - 8 MeV. The probability of a Compton event occurring increases with the number of electrons present, i.e. increasing Z, however it generally decreases as the incoming γ-ray energy increases. One interesting point to note is that the angular distribution of scattering angles changes significantly with initial photon energy. The differential scattering cross section is given by the Klein-Nishina formula

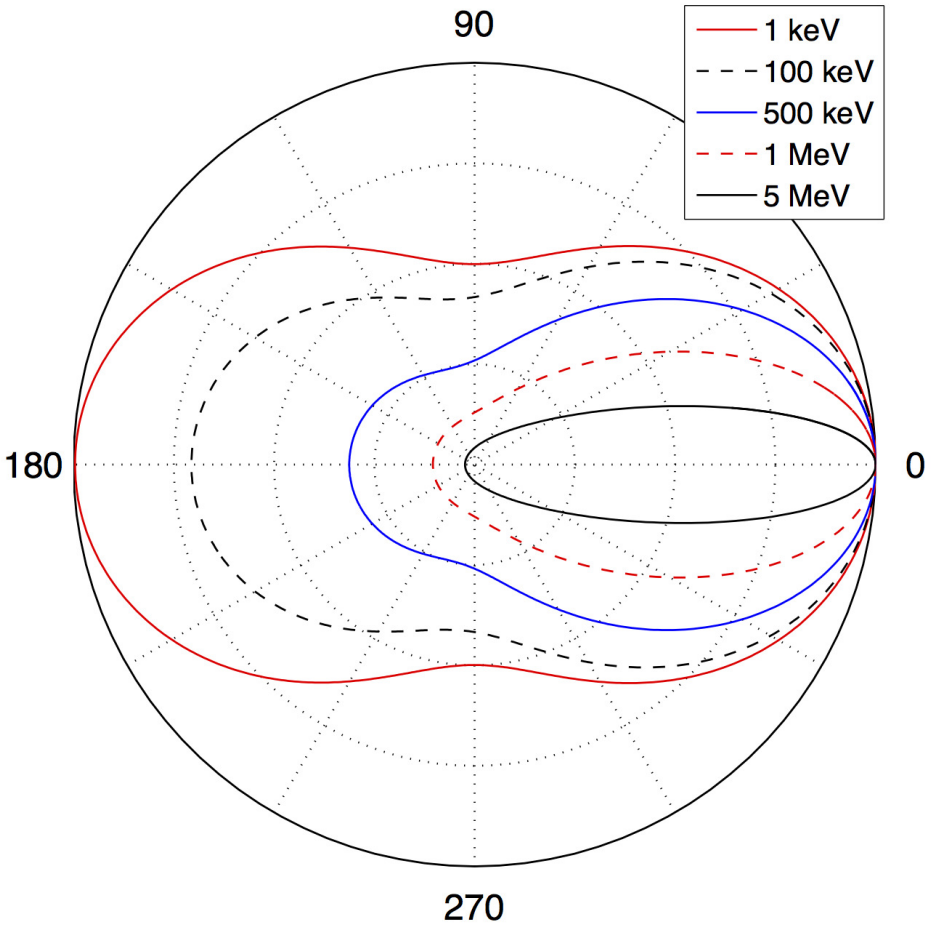

Figure 2.5: Polar plot showing the scattering distribution for varying initial photon energies. This clearly illustrates the forwards focussing which occurs at higher energies

$$\frac{d\sigma}{d\Omega} = Zr_0^2 \left(\frac{1}{1+\alpha(1-\cos\theta)}\right)^2 \left(\frac{1+\cos^2\theta}{2}\right) \left(1 + \frac{\alpha^2(1-\cos\theta)^2}{(1+\cos^2\theta)[1+\alpha(1-\cos\theta)]}\right) \tag{5}$$

where $\alpha = h\nu/m_0c^2$ and r_0 is the classical electron radius. Figure 2.5 demonstrates the effects of this formula for various energies, clearly illustrating the forward focussing that occurs at higher energies.

2.2.3 Pair Production

Pair production is a process only possible above 1022 keV, twice the rest mass energy of the electron. During this interaction, which must take place in the

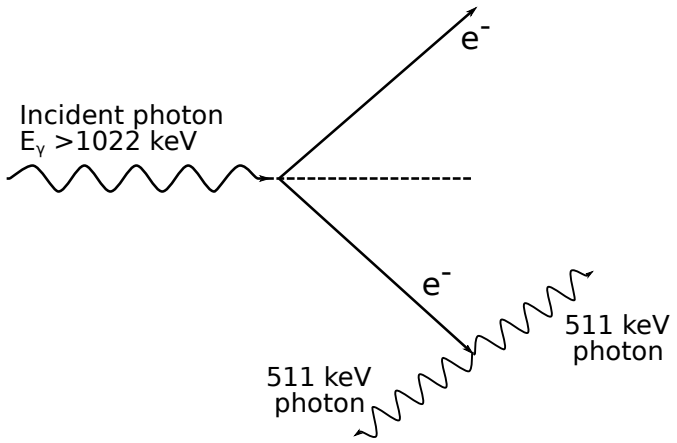

Figure 2.6: Schematic illustration of pair production, demonstrating the two back-to-back 511 keV photons produced

Coulomb field of the nucleus, the incoming photon is converted into an electron-positron pair with the excess energy given to the pair in the form of kinetic energy. The secondary stage of this interaction occurs when the positron meets an electron and annihilates, creating two back-to-back 511 keV γ-rays. This occurs due to it being more energetically favourable to exist as two γ-rays than an e^{-}e+ pair. If both of the photons are detected, then the full energy of the initial γ-ray will be detected. However it is possible for one or both of these photons to escape the detector, thus carrying information regarding the original γ-ray away with them. This results in two distinct peaks on the resulting spectrum, a single escape peak ($E_\gamma - 511$ keV) and a double escape peak ($E_\gamma - 1022$ keV).

For γ-ray energies just above 1022 keV, the probability of pair production is very small, however for initial photon energies much greater than the production threshold (≥ 10 MeV), pair production becomes the dominant interaction mode. This is demonstrated by Figure 2.2, which displays the relative importance of each of the three major interactions as a function of initial energy and atomic mass. No definitive expression exists for the relationship between pair production probability and Z, however the likelihood increases as approximately the square of Z [14].

2.2.4 Gamma Ray Attenuation

All of the interactions above have a distinct probability of occurring for a given γ-ray, however for a specific interaction only one can occur [14]. This means that the probability for an interaction of any kind is simply the sum of the individual contributions

$$\mu_l = \mu_{photoelectric} + \mu_{compton} + \mu_{pairproduction} \tag{6}$$

where μ_l is known as the linear attenuation coefficient. Since this value is linked to the likelihood an interaction will occur in a given distance, the reciprocal of this gives the average distance travelled by a photon before an interaction. This is known as the mean free path, λ, of the photon and is defined as

$$\lambda = \frac{\int_0^\infty x e^{-\mu x} dx}{\int_0^\infty e^{-\mu x} dx} = \frac{1}{\mu} \tag{7}$$

with typical values of λ for germanium varying from mm to cm. For a γ-ray energy of 1000 keV, the mean free path will be approximately 2 cm.

In most instances, the linear attenuation coefficient is combined with density of the material to give the mass attenuation coefficient, which more accurately describes the material, where

$$\mu_m = \mu_l / \rho \tag{8}$$

where ρ is the density of the material. A plot of the mass attenuation coefficients as a function of energy is given in Figure 2.7.

2.3 Detectors

The requirements for detectors are as varied as the physics they are used for, with a different set of parameters necessary to optimise each area of study. These key parameters include material properties such as energy and timing resolution, efficiency, temperature response as well as manufacturing issues such as the ability to construct large crystals of varying shapes in addition to the cost of the process.

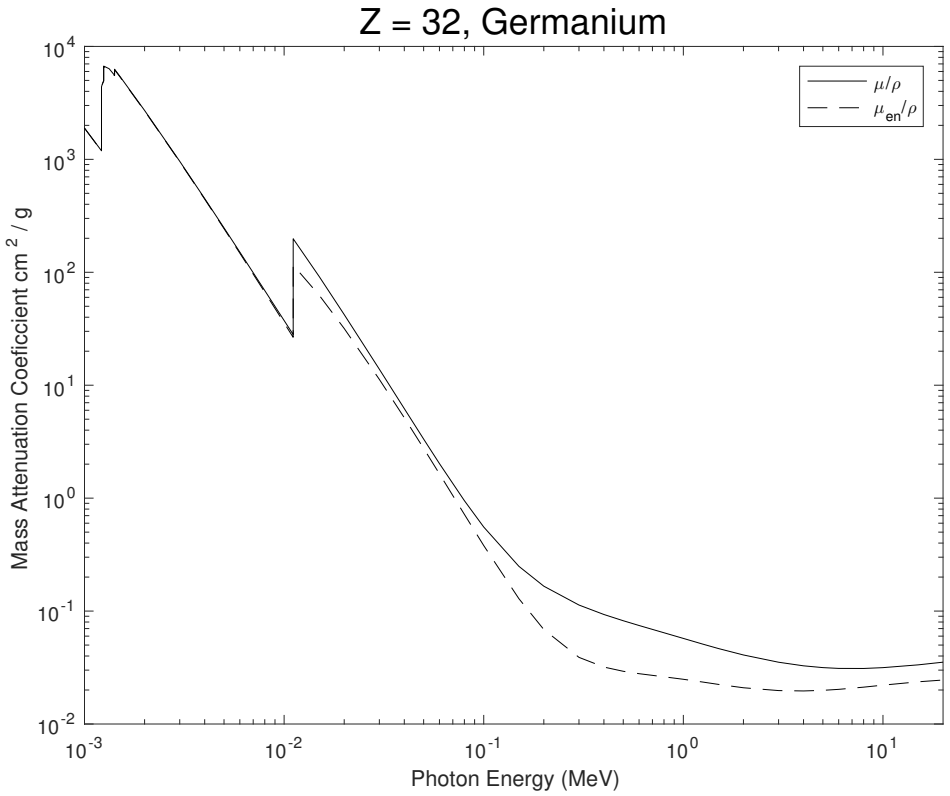

Figure 2.7: Plot of mass attenuation coefficient, μ/ρ, as a function of energy for Z = 32 germanium. Also shown is the mass energy absorption coefficient, μ_{en}/ρ

No material has been discovered which excels in all of these categories, thus forcing experimental physicists to choose the parameters that are key to their particular goal.

Like many experiments, energy resolution and efficiency are very important for the work described in this thesis. Accurate energies are required for calculating the reconstruction angle for Compton cones, with more statistics improving the resulting image. However, unlike most, the ability to accurately determine the position of an interaction within the detector is also crucial. This can be achieved through segmentation of the detector, or the use of materials with position sensitive charge pulses.

The material that has risen to become the gold standard for γ-ray spectroscopy is High Purity Germanium (HPGe). The unrivalled energy resolving capabilities in addition to the ability to manufacture a wide variety of crystal shapes has enabled detectors to be built for almost all purposes. HPGe is not as efficient as materials such as Sodium Iodide (NaI), however this can be improved drastically by crating multi crystal arrays which cover larger solid angles, as used in many experimental nuclear physics experiments. For experiments requiring position resolution, HPGe is able to be electronically segmented, creating 3-dimensional pixels known as voxels. The major drawback for HPGe lies in the small bandgap, $\sim$ 0.7 eV, which allows electrons to be thermally excited by the ambient temperature of the room. This requires each HPGe crystal to be cooled using liquid nitrogen (LN_2) to 77 K. Although HPGe is most commonly used for detector arrays, many ancillary detectors such as those used for Compton suppression systems still utilise scintillator technologies.

2.3.1 Semiconductors

The use of semiconductors in nuclear instrumentation has revolutionised the field of nuclear spectroscopy. The increased density of solid material when compared to that used in a gas detector, has resulted in a dramatic decrease in the physical size of two equivalent detectors. This has enabled compact 4π detector arrays to

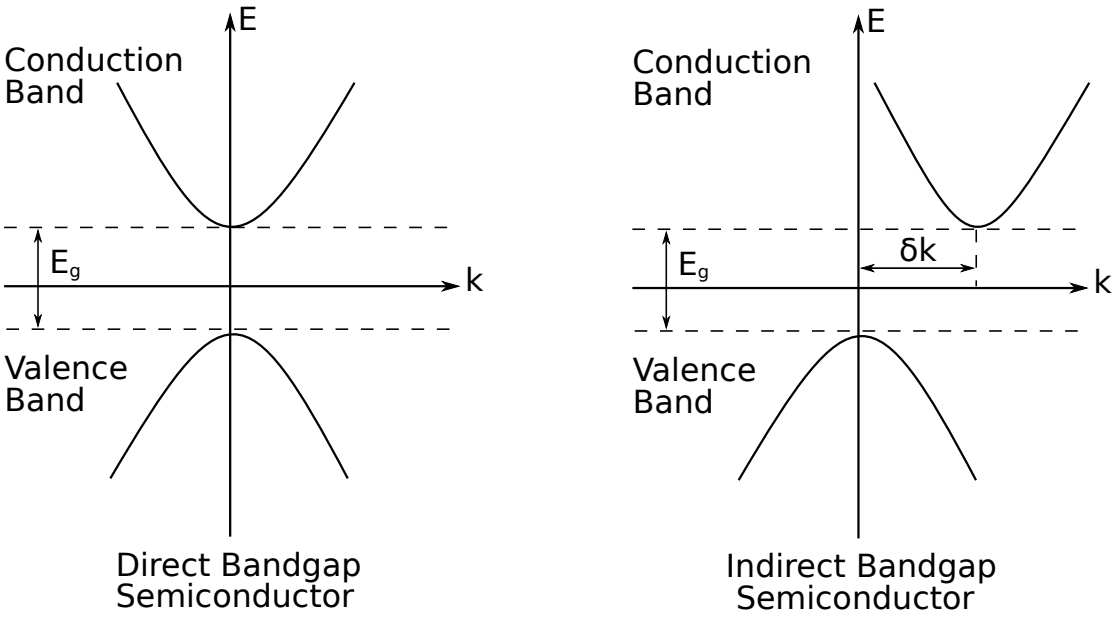

Figure 2.8: Two e-k diagrams representing the range of energy and momentum states possible for an electron in the crystal lattice. Electron energies increase in the positive vertical direction, with hole energy increasing in the negative vertical direction

become a possibility. In addition to the flexibility of semiconductors, they also present a major improvement in terms of energy resolution, a characteristic that has propelled them to the forefront of modern detector systems.

2.3.2 Band Structure

The performance of a semiconductor can be related strongly to the band structure of the material used. Electrons in crystalline solids are confined to discrete quantised energy bands. The energy difference between the valence and conduction band governs the conductivity of the material, with insulators having a large energy gap (≥ 5 eV) and conductors having no gap at all. The nature of the word semiconductor implies that these materials possess a small, non zero energy gap which prevents complete free flow of electrons, but allows for electrons to move into the conduction band given enough energy.

The band structure of germanium can be explained best using an energy-momentum (e-k) curve. This shows the relationship between the energy and mo-

mentum of the conduction and valance bands in the material. There are two types of bandgap semiconductor, direct and indirect. Figure 2.8 demonstrates this, with electron energy increasing in the positive direction, and hole energy increasing in the negative direction. The energy bandgap can be seen as the point of closest contact between the two bands, physically representing the point at which the electrons require the least amount of energy to move from one band to another. A direct bandgap semiconductor only requires a change in energy to excite an electron across the bandgap, however an indirect bandgap requires a change in momentum in addition to a change in energy. For an indirect bandgap semiconductor, the excited electron must first pass through an intermediate state, transferring momentum to the crystal lattice. This is illustrated in Figure 2.8 by the maximum and minimum of the respective bands not aligning on the momentum axis. It should be noted that germanium is an indirect semiconductor, with the bandgap for HPGe cooled to 77K being ~ 0.7eV.

For materials not at absolute zero, there exists the possibility that electrons in the valence band could be thermally excited across the bandgap. These electrons are excited up the conduction band leaving a hole in the valence band, creating an electron-hole pair. It is these electron-hole pairs that move through the material when exposed to an applied electric field, thus contributing to the conductivity of the material. The probability of an electron-hole pair being thermally generated is given by

$$p(T) = CT^{3/2} exp\left(-\frac{E_g}{2kT}\right) \tag{9}$$

where C is a material dependant constant, T is the absolute temperature, E_g is the energy gap and k is the Boltzmann constant. It can be seen that for semiconductors with small bandgaps, the probability of thermal excitations depends greatly on the temperature of the detector. It is for this reason that germanium detectors will always be cooled before use, either with liquid nitrogen or using a mechanical cooling system.

2.3.3 pn Junction

Semiconductor electronic properties can be altered by introducing impurities into the material, a process known as doping. Germanium atoms contain four electrons in their valence band, which bind directly to four additional germanium atoms. However by introducing impurities which contain either three or five valence electrons, the lattice will now have an excess of holes or electrons. These new materials are known as p-type (trivalent doped) and n-type (pentavalent doped) semiconductors.

When n-type and p-type materials are placed in contact with one another, a depletion region is created at the junction. This serves as the active volume of the detector, where the excess of electrons and holes in the respective materials cancel out. By applying a reverse bias to the detector, where the n-type receives a positive voltage and the p-type receives a negative bias, the depletion region can be increased. The bias causes the remaining electrons and holes to migrate towards their respective contacts, thus increasing the active volume of the detector.

2.3.4 High Purity Germanium

One issue present in germanium semiconductors is the small bandgap, ~ 0.7 eV. At room temperature, the thermally induced leakage current is extremely large resulting in a significant degradation of the energy resolution. Due to this, HPGe crystals must be cooled using liquid nitrogen to temperatures of 77 K so as to reduce this leakage current.

Detector efficiency is directly related to the size of the active area within the detector, i.e. the depletion region. The thickness of the depletion region, d, squared is inversely proportional to the net impurity concentration, N, within the detector material,

$$d^2 \propto \frac{1}{N} \tag{10}$$

Germanium of normal semiconductor purity is only capable of producing a depletion depth of 2-3 mm, which is insufficient for γ-ray spectroscopy. This lead

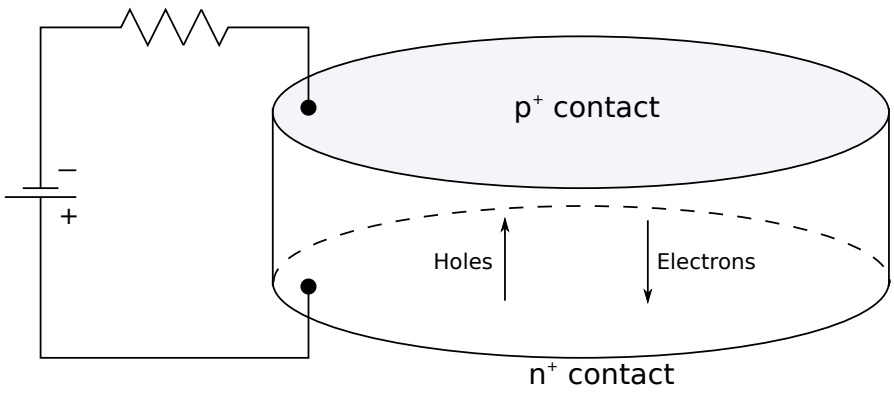

Figure 2.9: Configuration of a basic planar HPGe detector [14]

to the development of High Purity Germanium (HPGe), with impurity concentrations of approximately 1 part in 10^{12}, capable of reaching a depletion depth of several centimetres.

The work in this thesis utilises a segmented planar geometry. A basic planar geometry is illustrated in Figure 2.9, and is essentially a block of HPGe with contacts on the top and bottom [14]. The detector is then reverse biased, with the n-type contact receiving a positive bias voltage and the p-type contact set to zero volts. The ability to electrically segment the contacts on both sides allows for a grid system to be created, providing information regarding the location of interactions within the detector.

The major advantage of semiconductors is the small ionisation energy, ~ 3 eV for HPGe. This allows for a larger number of charge carriers to be generated for a given initial γ-ray energy when compared to scintillator or gas detectors. Since the energy resolution for a detector is determined by statistical fluctuations, this dramatic increase in charge carriers reduces the influence of large fluctuations thus improving the overall resolving power (ΔE). Table 2.1 list the relevant physical and electrical properties of germanium.

2.3.5 Lattice Structure

Figure 2.10 demonstrates the crystal lattice structure of germanium, with its face centred cubic structure. The orientation of the lattice with respect to the electric

Table 2.1: Properties of intrinsic germanium [14]

Atomic number	32
Atomic weight	72.60
Density (300K); g/cm^3	5.32
Atoms/cm^3	4.41×10^{22}
Dielectric constant (relative to vacuum)	16
Intrinsic carrier density (300K); cm^{-3}	2.4×10^{13}
Intrinsic resistivity (300K); $\Omega\cdot$ cm	47
Electron mobility (300K); cm$^2/V\cdot$ s	3900
Hole mobility (300K); cm$^2/V\cdot$ s	1900
Electron mobility (77K); cm$^2/V\cdot$ s	3.6×10^4
Hole mobility (77K); cm$^2/V\cdot$ s	4.2×10^4
Energy per electron-hole pair (77K); eV	2.96

field can cause significant changes in the drift properties of electrons inside of the detector, due to the differing number of atoms in the direction of the electric field lines. When performing simulations of HPGe detectors it is vital that the lattice structure is accounted for.

For charge collection simulations, the velocity with which both electrons and holes traverse the medium must be understood to a high degree. This velocity is known as the drift velocity, and is dependent on factors such as the electric field strength, temperature and lattice orientation. Due to the differences in transportation methods, electrons intrinsically travel faster than holes. Electrons travel as free particles along the electric field lines, whereas holes travel by constantly displacing electrons from bound shells, hence the slower intrinsic drift velocity.

The electric field provides the potential with which the carriers gain energy, meaning that as the field strength increase, so does the drift velocity. For low to intermediate field strengths, this is a fairly linear process, with the drift velocities for electrons and holes, ν_e and ν_h, defined by the mobility constants, μ_e and μ_h respectively

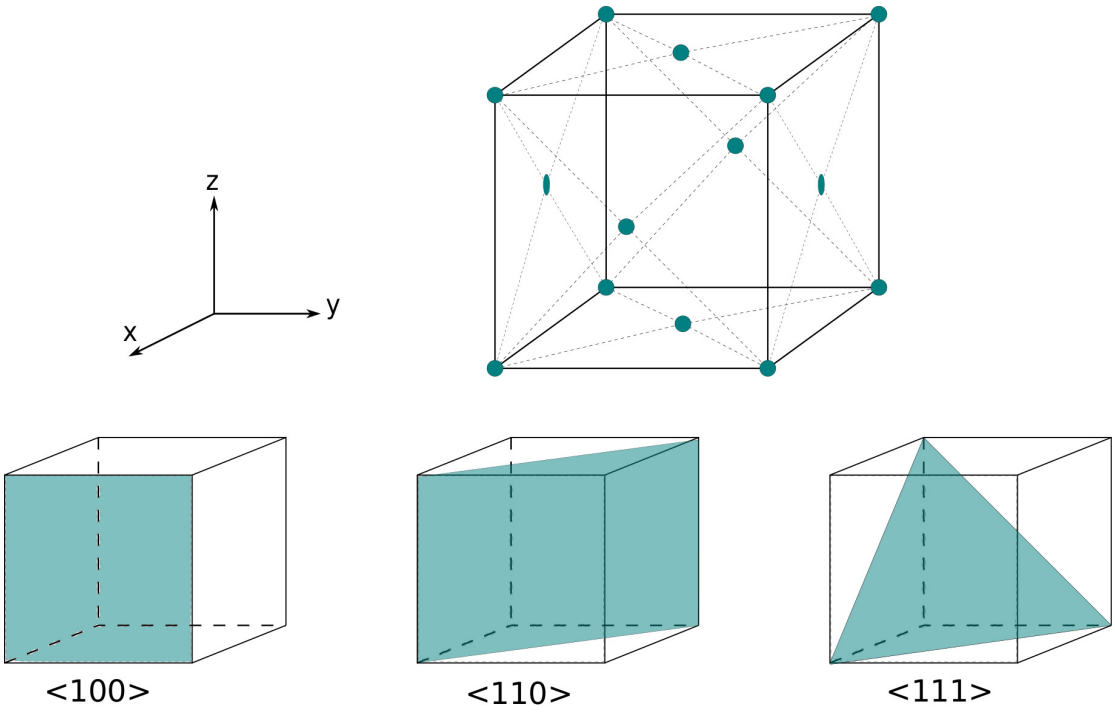

Figure 2.10: Face centred lattice structure of germanium, with the various different lattice planes represented by Miller indices

$$\nu_e = \mu_e E \tag{11}$$

$$\nu_h = \mu_h E \tag{12}$$

where E is the electric field strength. However for high values of electric field strength ($\sim 10^4$ V/cm), the drift velocity saturates ($\sim 10^7$ cm/s) [14]. The temperature of the crystal has effects on the energy of individual atoms within the crystal lattice. For temperatures above absolute zero, the lattice will vibrate, resulting in an increased probability of electrons being scattered by the lattice. This in turn reduces the mobility of charge carriers.

The final component affecting the drift velocity is the orientation of the crystal lattice with respect to the electric field. Figure 2.11 demonstrates the effects of this, with the drift velocity being significantly faster for the <100> than both the <110> and <111> orientations. The explanation for this effect is purely geometric, with the distance between atoms along the electric field lines changing

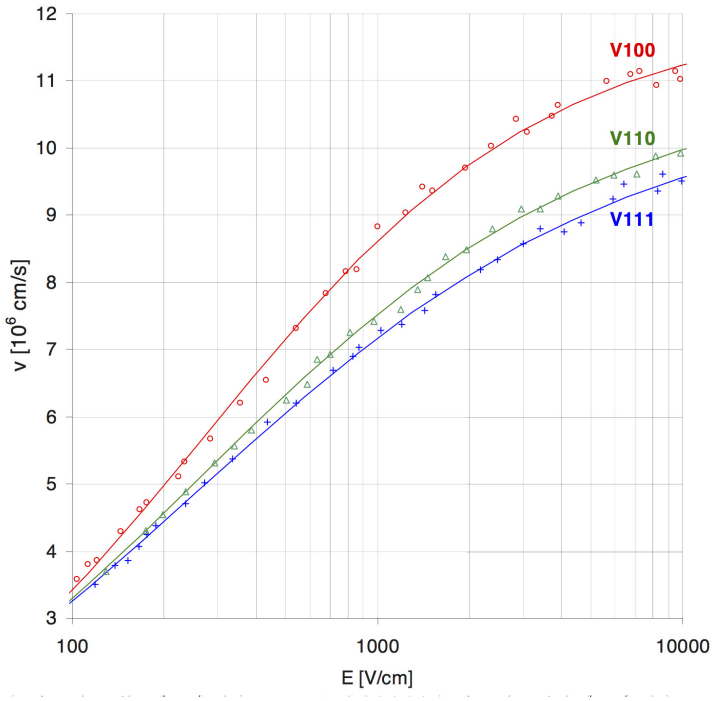

Figure 2.11: Drift velocities of electrons through germanium as a function of electric field strength and crystal lattice orientation [15]

for each orientation. Shorter distances result in more interactions for a given distance travelled, causing the drift velocity to be reduced.

2.4 Signal Generation

As discussed in an earlier section, it is crucial that a detector provides an output that is proportional to the energy of the incoming radiation. For HPGe detectors, incoming radiation interacts with the detection medium, resulting in the production of e-h pairs. The number of e-h pairs produced is directly related to the γ-ray energy deposited, and by extension, the charge is also related to the energy. The charge generated as the result of an interaction, Q_s is given by

$$Q_s = \frac{E}{E_i} e \tag{13}$$

where E is the energy absorbed from the interaction, E_i is the energy required to produce and e-h pair an e is the charge of the electron. The electric field in

the detector will govern the motion of these charge carriers, with each charge carrier drifting towards the opposite polarity electrode. The motion of these charge carriers through the detector is what generates the signal, with different signals produced depending upon the distance travelled by each carrier. This is the foundations of Pulse Shape Analysis, with the shape of the generated signal, or pulse, providing positional information.

2.4.1 Electric Field

The general starting point in calculating the electric field inside of a detector is to solve the Poisson equation

$$\nabla^2\varphi = \rho/\epsilon \tag{14}$$

where φ is the electric potential, ρ is the charge density and ϵ is the dielectric constant of the detecting material. For detectors where there are no trapped charges, $\rho = 0$ and Eqn 14 reduces to the Laplace equation

$$\nabla^2\varphi = 0 \tag{15}$$

For detectors described using a Cartesian coordinate system, such as the one used in this work, the Laplacian operator ∇^2 is given by

$$\nabla^2 = \frac{\delta^2}{\delta x^2} + \frac{\delta^2}{\delta y^2} + \frac{\delta^2}{\delta z^2} \tag{16}$$

Based upon the operating conditions of the detector, different boundary conditions are applied to solve the equations. For planar detectors, one example condition is that the voltage must be equal to the applied bias voltage at one electrode and equal to zero at the opposite electrode. For simple geometries, analytic solutions can be calculated, however for more complicated geometries such as the one in this work, computer simulations are required to solve these equations.

The electric potential can be used to calculate the electric field at any position within the detector by taking the gradient of the potential

$$E = -grad\,\varphi \tag{17}$$

2.4.2 Weighting Field

Charge carriers generated in the detector volume will follow the direction of the electric fields lines discussed in Section 2.4.1, however to calculate the actual induced charge on an individual electrode, we must use the Shockley-Ramo theorem [16, 17]. This also introduces the concept of a weighting field, $\overrightarrow{E}_0$, and weighting potential, φ_0. According to the theorem, the instantaneous current, i, induced on an electrode is given by

$$i = q\overrightarrow{v} \cdot \overrightarrow{E}_0 \tag{18}$$

where q is the charge of the carrier and $\overrightarrow{v}$ is the velocity of that carrier. This can be restated in terms of the weighting potential, with the induced charge being given by the product of the charge multiplied by the difference in the weighting potential from the start to the end of the carriers path

$$Q = q\Delta\varphi_0 \tag{19}$$

The weighting potential varies only as a function of detector geometry and to calculate the potential as a function of position, three boundary conditions must be set:

- The voltage on the electrode of interest is set to unity
- The voltage on all other electrodes is set to zero
- All trapped charges (if any) in the detector are ignored

From these conditions, a charge near the collecting electrode will induce a charge on the electrode, with the charge on all neighbouring electrodes being zero. Although the final charge on the non-collecting electrodes is zero, transient charges are induced during the collection period. The maximum transient charge is related to the proximity of the charge to the electrodes.

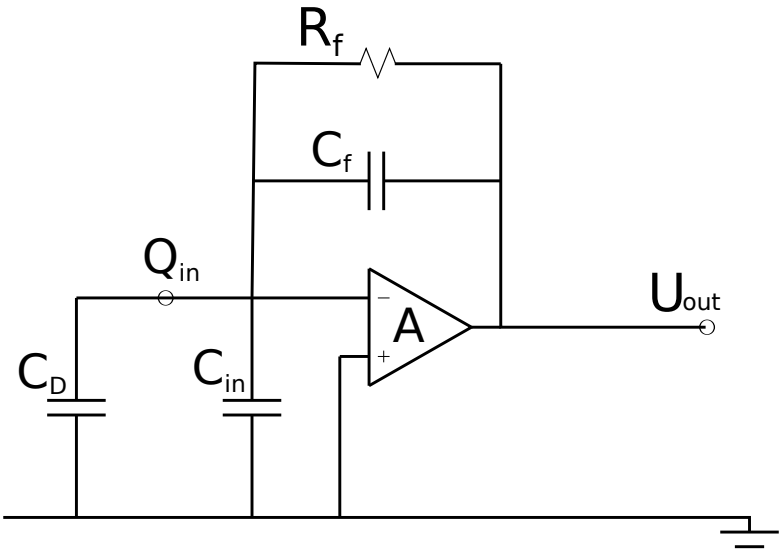

Figure 2.12: Schematic of a charge sensitive preamplifier

2.4.3 The Preamplifier

The charge induced by an interaction between a γ-ray and the detection medium is very weak, making the task of analysing it very difficult. To rectify this, the charge is amplified almost instantaneously using a preamplifier. The preamplifier increases the amplitude of the incoming signal and converts it to a voltage.

Most preamplifiers fall into one of three categories, current sensitive, voltage sensitive and charge sensitive. Both current and voltage sensitive preamplifiers are not suitable for this type of work for varying reasons. Current sensitive preamplifiers require a constant rise time, which is problematic since charges from a semiconductor vary significantly with interaction position. Voltage sensitive preamplifiers utilise the intrinsic capacitance of the detector to convert the charge collected into a voltage signal which is then amplified. The issue with this approach is the fact that the intrinsic capacitance of the detector varies with external factors such as temperature and bias voltage, causing the voltage signal generated to vary too. The solution to these problems is to use a charge sensitive preamplifier, which only relies on the actual charge generated from an interaction. A circuit diagram for a basic charge sensitive preamplifier is shown in Figure 2.12.

The input charge, Q_{in} charges the feedback capacitor, C_f, giving rise to the

fast leading edge, which then slowly discharges through the feedback resistor with a decay constant $\tau_f = R_f C_f$. The output voltage provided by the preamplifier is given by

$$U_{out} = \frac{Q_{in}}{C_f} \tag{20}$$

The value of R_f governs the time taken to discharge the capacitor, which in turn governs the amount of time required between two measurements. Large values of R_f increase the fall time of the charge pulse, thus reducing count rate, however this also has the effect of reducing the electrical noise in the pulses. For a typical preamplifier, $R_f \sim 1G\Omega$

2.5 Compton Imaging Methodology

2.5.1 Compton Imaging

The idea of a multi-element Compton camera was first proposed in nuclear physics in 1974 [18]. Utilising two HPGe detectors, one scatterer and one absorber, the principles of Compton scattering can be used to reconstruct the location of a source from the energy deposits and location of two interactions. The work in this thesis aims to apply this concept to a single HPGe detector, using fold 2-2 interactions to imitate the scatterer and absorber detectors traditionally used. For this work, fold refers to the number of individual channels within the detector firing, with the two numbers referring to the AC and DC coupled faces of the detector respectively.

In a traditional Compton camera setup, two detectors will be positioned in line, with the first used to scatter the incoming radiation into the second. The second detector is used to absorb the remaining energy of the radiation. The detectors used for this are usually double sided strip detectors, allowing for the lateral position of the interaction (x & y) to be determined by the hit strips. The depth of the interaction, z, is given by the separation between the two detectors. These coordinates, in combination with the energy deposited in each interaction, enable the angle of scatter, θ, to be calculated as shown in Eqn 21. This θ value is then projected into a 3-dimensional cone revealing the possible locations of the

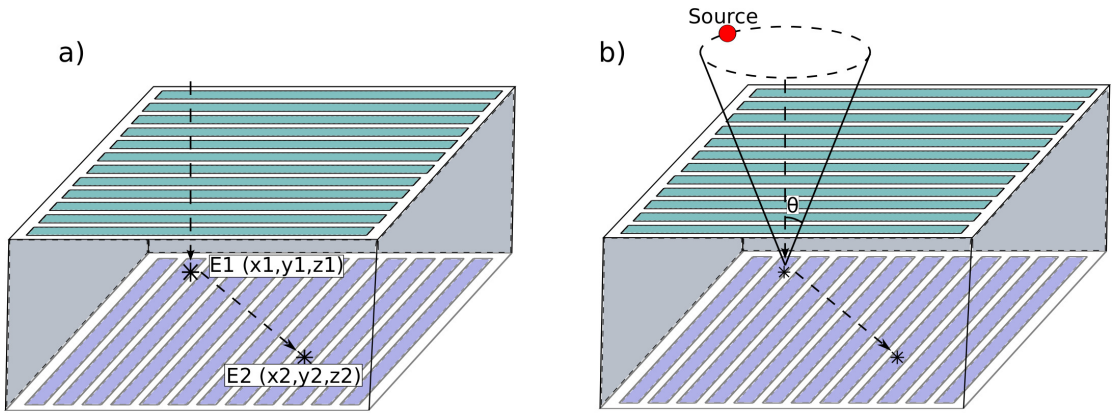

Figure 2.13: The processes involved in a Compton camera, (a) two interactions occur in the detector, E1 is a scatter which deposits some energy in the crystal and scatters, E2 is a full absorption where the remaining energy is absorbed (b) From the two interaction locations and energy deposits a scatter angle can be determined which enables the location of the source to be isolated to the circumference of a cone whose angle is θ. Increasing the number of events allows for more cones to be constructed and the source location is revealed by the intersection of the cones

source. Additional events are used to create more cones, with the overlap of all cones revealing the source location. The more events that are reconstructed, the clearer the emission point becomes.

$$\cos\theta = 1 - m_e c^2 \left(\frac{1}{E_2} - \frac{1}{E_1 + E_2} \right) \tag{21}$$

The work presented in the following chapters aims to recreate this process using a single detector. This concept has been investigated for a highly segmented coaxial HPGe detector [19, 20], with proposals for a planar strip detector also made [21]. For this method to be viable, the radiation must scatter via a large angle and remain within the volume of the detector. The scattered photon must then be fully absorbed by the next interaction. As before, the xy position of the 2 interactions will be given by the hits on each strip. However in this instance the energy deposited in each interaction must be assigned to the correct strips. The major challenge in this approach comes in determining the depth of the interaction. Since the two events occur in the same detector, the distance between the two is

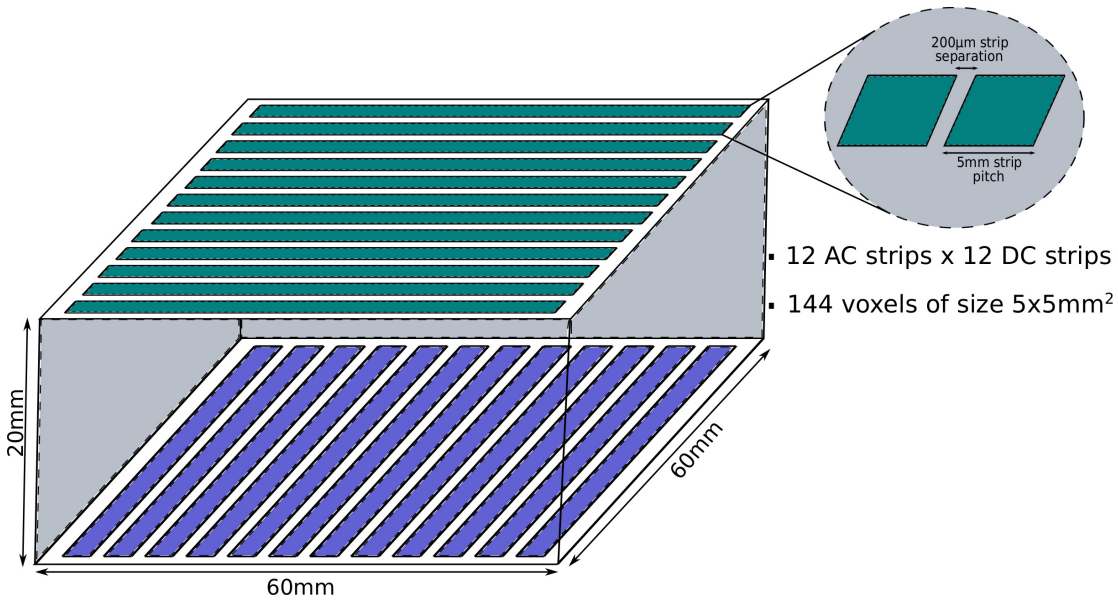

Figure 2.14: Schematic of the Double Sided Germanium Strip Detector used in this work

very small, meaning any errors in the depth will be exaggerated when constructing the cones later on. In order to determine the interaction depths, Pulse Shape Analysis (PSA) techniques were used, which will be discussed in more detail in Section 3.1. The ideas discussed in this section are illustrated in Figure 2.13.

2.5.2 Double Sided Germanium Strip Detector

The detector used in this project was a Double Sided Germanium Strip Detector (DSGSD), manufactured by Canberra. A schematic illustrating the dimensions of the detector is provided in Figure 2.14, with a photograph of the detector shown in Figure 2.15. The detector consists of a High Purity Germanium crystal measuring $60 \times 60 \times 20$ mm^3. Each face is electronically segmented into 12 strip contacts with a strip pitch of 5 mm, creating a 12×12 orthogonal matrix. The n+ DC coupled contacts are ~ 0.3 μm thick, with the p+ AC coupled contacts being ~ 0.5 μm thick, with an interstrip gap of ~ 200 μm. A 7 mm wide guard ring (not shown in Figure 2.14) surrounds the crystal, ensuring uniform electric fields near the edge of the detector, bringing the total dimensions to $74 \times 74 \times 20$ mm^3.

The impurity concentration on the n+ DC face was 0.70×10^{10} cm^{-3}, with the

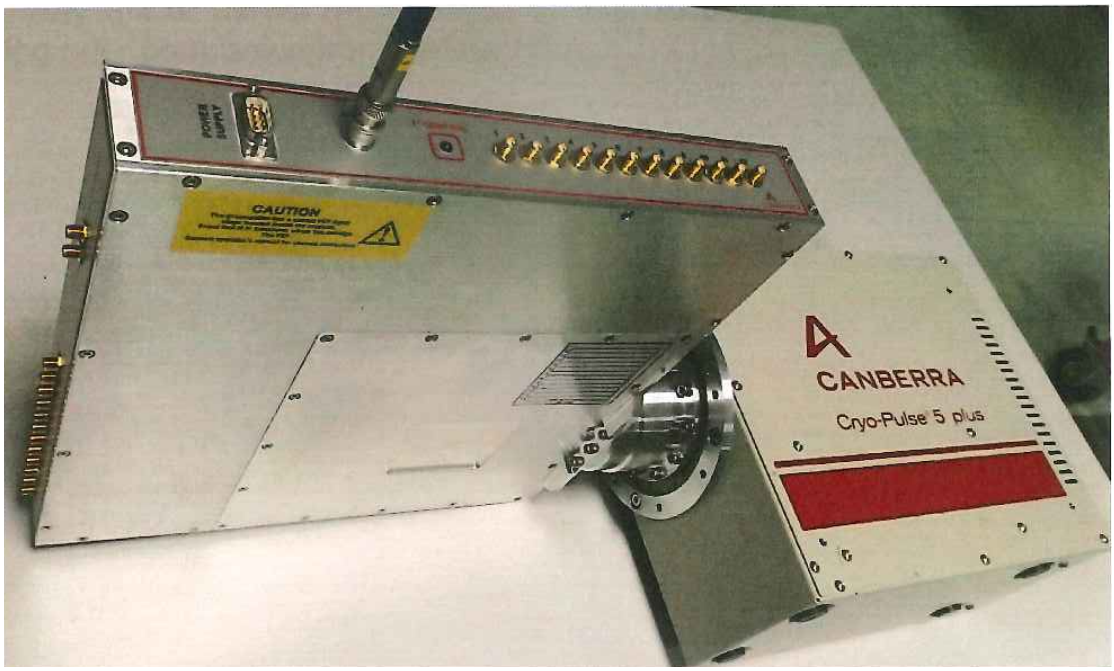

Figure 2.15: Photograph of the Double Sided Germanium Strip Detector used in this work

concentration being 0.85×10^{10} cm^{-3} on the p+ AC face. Although these values were specified by the manufacturer, the measured depletion voltage of the crystal was between 1250 V and 1500 V, indicating that the impurity concentrations should be slightly lower than those quoted, by $\sim 0.1 \times 10^{10}$ cm^{-3}. The energy resolution of each strip in the DSGSD is typically around FWHM = 2 keV at 121 keV and FWHM = 3.5 keV at 1332 keV. From here on, the AC strips will be labelled as strips 1-12, with the DC strips being labelled as strips 13-24.

2.5.3 Digital Electronics

For the experimental Compton imaging measurements, a digital electronics system was used. The switch from analogue to digital electronics enables the full potential of detector systems to be reached. There are many advantages for digital electronics, however three stand above the rest; increased data rates, reduced physical size and digitised storage of all pulse information. Increased data rates provide much greater statistics for weaker transitions, enabling more exotic features of nuclear structure to be observed. With hundreds of data channels necessary for modern

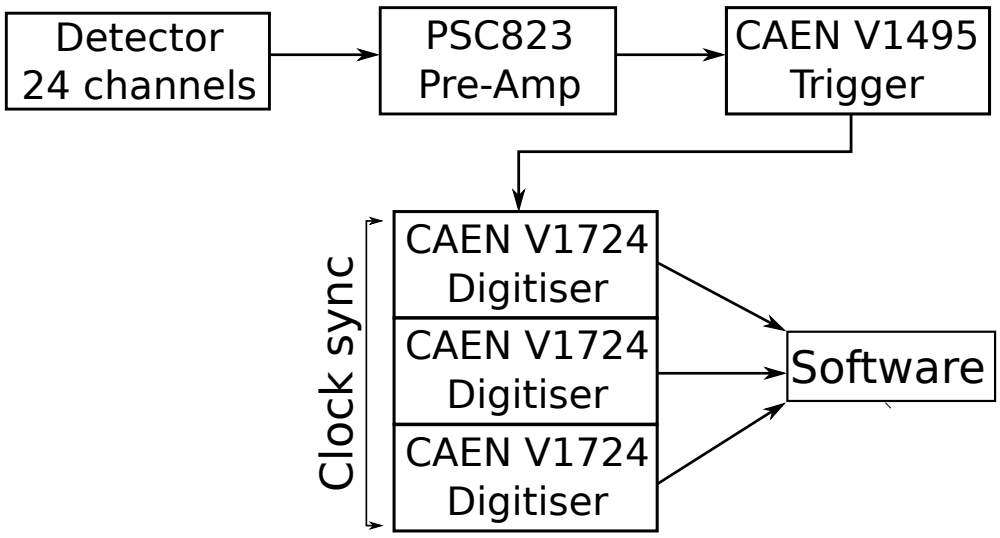

Figure 2.16: Schematic of the digital electronics system used to process pulse information for the Compton imaging work presented in this thesis

detector arrays, the physical space required for analogue electronics is enormous, with the equivalent digital system capable of fitting all of the electronics into a few crates. Possibly the largest difference with digital electronics is the ability to keep all of the information present in each pulse. By digitising the waveform, it can be stored and analysed at any point in the future. This is crucial for PSA, with the pulse shapes of each interaction required for later analysis.

As with the analogue equivalent, pulses are first amplified by a preamplifier, before being transferred to the digitiser card. The fundamental operation of a digitiser is to sample an analogue pulse and transform it into a digital pulse. Once a digital pulse has been created, the true flexibility of digital electronics is displayed. Each digitiser can be programmed with software specific to the users end goal.

The electronics used for the Compton imaging work consisted of a CAEN V1495 card [22] connected to three CAEN V1724 digitiser cards [23]. The V1495 card was used to apply a hardware trigger on the data, set at 40 keV, with the V1724 cards used to digitise all information contained in the charge pulses. All data was taken in singles mode, with a single channel firing above the trigger resulting in all channels being written. Additionally, a pre-trigger was set at 650

ns, which accounts for the lag caused by the triggering process. Each V1724 digitiser consists of a 14 bit flash ADC which samples with a frequency of 100 MHz, with each card containing 8 channels, hence three cards required for the 24 channels from the DSGSD. All three of the V1724 cards were synced to match the clock of the first card. Pulse information is temporarily stored on a buffer, where it can be written to disk should it meet the trigger criteria set on the V1495 card. When a pulse triggers, the buffer is frozen while the datum is exported. To reduce the amount of dead time, each channel contains multiple buffers enabling a constant flow of data, this essentially reduces the dead time to zero. Once the information is written to the V1724 cards, a pre-sort can be applied which performs basic analysis on the events, calculating the essentials parameters in addition to passing the digitised waveform to the storage array. The most important of these parameters include the energy, timestamp and channel number. Prior to the experimental measurements, each channel is gain matched and calibrated using a ^{152}Eu source. The values obtained from the gain match and calibration are input into the pre-sort to correct each channel before any further analysis takes place. A schematic of the digital electronics used in this work is presented in Figure 2.16.

3 Pulse Shape Simulations

3.1 Simulated Detector Response

Compton imaging requires a precise knowledge of the interaction positions for both the scattered and absorbed photons. For detectors such as the Double Sided Germanium Strips Detector (DSGSD) used in this work, this position resolution is provided by the orthogonally placed strips which can be used to create voxels. The detector contains twelve strips on the AC side and twelve perpendicular strips on the DC side, with a strip pitch of 5 mm. This creates 144 voxels each measuring $5 \times 5 \times 20$ mm^3, allowing the interaction position to be determined in the xy plane of the detector face to within 2.5 mm. One problem with this is the lack of information regarding the depth of the interaction, a problem that can be solved through the use of Pulse Shape Analysis (PSA) [24]. The application of PSA can also be used to improve the position resolution in the x and y dimensions.

PSA relies on the fact that interactions occurring at different locations in a semiconductor detector, will produce a slightly different output signal. Due to the nature of charge collection inside a semiconductor, electrons and holes will travel towards opposite electrodes after an interaction. The time taken for each charge carrier to reach the specific electrode will govern the overall shape of the pulse generated. Using this principle, a database can be created containing pulse shapes for all possible interaction positions within the detector. The easiest way to create such a database experimentally is through a coincidence scan. Using a collimated source, specific interaction positions can be selected and the detector response can be measured. This process is then repeated for all possible locations in the detector volume. Although effective, this process can take many months to complete and only creates a partial database. An alternative method is to use a computer simulation to generate the pulse shape database (such as the Agata Detector Library [25, 26]).

3.2 AGATA Detector Library

The Agata Detector Library (ADL) [25, 26] is a simulation package developed by Bart Bruyneel and Benedikt Birkenbach at the Institut für Kernphysik der Universität, Cologne, Germany. The package is written in standard C, with the equations required to simulate charge transport inbuilt. There are currently two versions of ADL in circulation, ADL version 3.0 and the GERDA distribution of ADL. The latest versions come with three inbuilt detector geometries, planar, coaxial and Broad Energy Germanium (BEGe), however the capability exists for building any detector geometry you require, as will be discussed later on in Section 3.2.1.

ADL also contains an electric field solver, allowing for electric potentials and weighting potentials to be generated within the software. These are calculated by solving the Poisson equations as discussed earlier in Sections 2.4.1 and 2.4.2. Once the fields have been set up, an interaction is simulated within the detector volume and the resulting charge carriers are tracked until they terminate at an electrode.

The structure and flow of ADL is illustrated in Figure 3.1, with the light grey boxes representing inputs defined by the user, the white boxes being the subroutines programmed into ADL and the dark grey box showing the output of the program. Inputs such as the impurity concentration and detector geometry are crucial for correctly calculating the charge transport properties of the detector. If these are not defined correctly, the electric potential will be incorrectly calculated resulting in charge carriers taking unrealistic paths as they drift through the detector. Other inputs such as the charge carrier mobility are taken directly from the literature and are assumed to be the same for all detectors, with the orientation of the crystal axis determined by the method used to grow the crystal. The effects of different crystal axis orientation are discussed in Section 2.3.5, with Figure 2.11 showing the effects of axis orientation on drift velocity for varying electric field strengths.

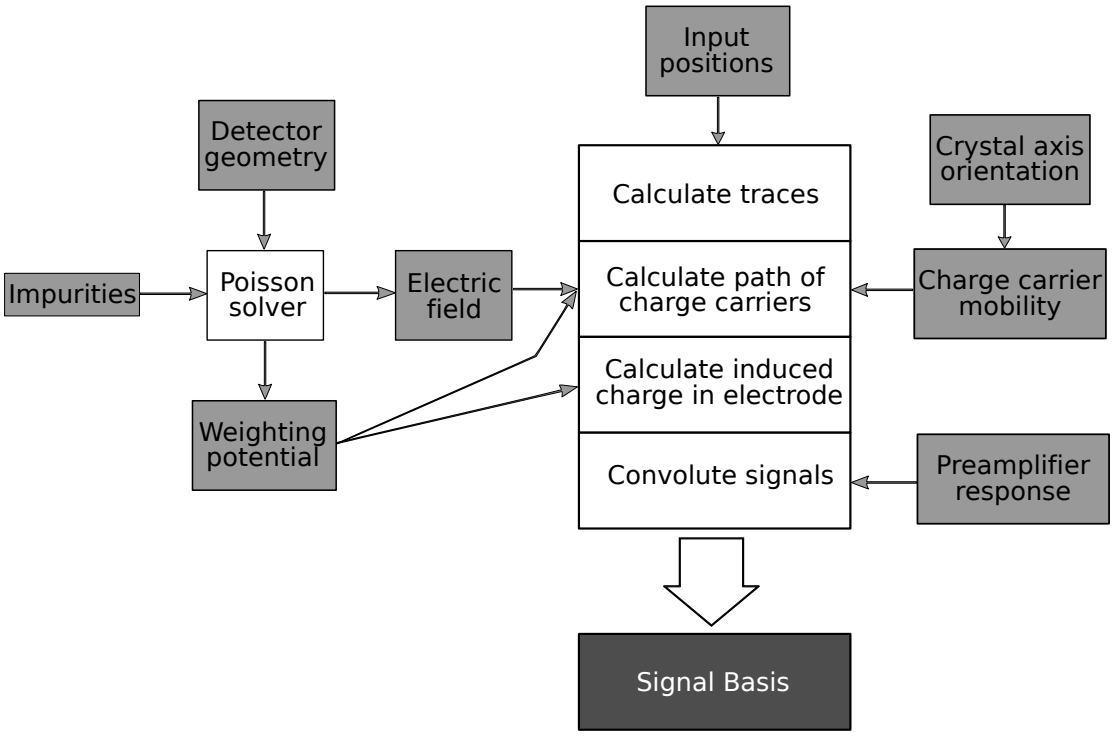

Figure 3.1: Illustration of the work flow within the ADL package. Light grey boxes are user inputs, with white representing the predefined subroutines and dark grey being the final output

Table 3.1: High level structure of ADL, adapted from [27]

.txt files	Description
ADL	Main file used to setup the program and navigate to all other template files
CONVL	Controls how to convolute the signals with a transfer function
DRIFT	Controls the drift parameters for the charge carriers
EVENT	Defines the event information
FIELDS	Controls the electric and weighting fields, also points to location of necessary files
GEOMETRY	Defines the value of geometric variables used to create the geometry within the confines of the source files
READWRITE	Sets the read and write options
TIME	Controls timing aspects of the simulation
TRACES	Sets up parameters used in calculating the traces
TRAPPING	Correction parameters for trapping

3.2.1 ADL Geometry

As mentioned earlier, the current versions of ADL, version 3.0 and the GERDA distribution, come with three pre-defined geometries; planar, coaxial and BEGe. The package is written in such a way that users wishing to run simulations for any of the predefined geometries never need to delve into the source files. All variables used in the program are read in from a series of `.txt` files, described in Table 3.1.

The `GEOMETRY.txt` file contains all the variables necessary to define the detector geometry, such as detector height, radius, contact thickness, etc. This is all performed on a grid system, with the smallest definable object equal to one grid unit. For geometries that contain a symmetry, such as a basic planar detec-

Table 3.2: Variables used to define the geometry of the DSGSD

Variable	Description	Value
ExtGroundWidth	Defines the external ground surrounding the detector	7mm
Spacing	Defines the spacing between the detector bulk and the external ground	1mm
BotContactDepth	Defines the thickness of the bottom contact layer	1μm
Height	Defines the height of the detector in the the z-direction	20mm
TopContactDepth	Defines the thickness of the top contact layer	1μm
NumOfStrips	Defines the number of contact strips per side	12
StripWidth	Defines the width of each strip	4.8mm
StripGap	Defines the interstrip gap	200μm

tor, the detector can be described as a 2-dimensional plane and extrapolated to a 3-dimensional object through the symmetry axis. However for objects with no symmetries, such as the DSGSD used in this work, the detector must be defined in three dimensions.

For geometries that differ from the predefined examples, the user must use the `SIMION_Geometry_*` files available in the `/src` directory. The `SIMION_Geometry.c` file is used to read in the geometry file and set up the field calculations. From here a `SIMION_Geometry_xxx` can be created to describe the geometry of the detector you wish to simulate. The user must first create the grid on which the detector will be defined. This is done by creating a three-dimensional array of size nx $\times$ ny $\times$ nz where the variables nx, ny, nz are defined in terms of the individual detector components that comprise that dimension, for example

nz = BotContactDepth + Height + TopContactDepth

where the variables used describe the dimensions of their respective components, as explained in Table 3.2. From here, boundaries are created in x, y, z and then set to the corresponding material, e.g.

if{ $x_i < nx < x_f$ &&
$y_i < ny < y_f$ &&
$z_i < nz < z_f$
}
return type

where `type` is a predefined component whose electrical properties are described in the `SIMION_Geometry` files. Each component of the detector geometry can be defined in such a way until the entire volume has been filled. Table 3.2 describes the variables used to define the geometry of the DSGSD, with the full `SIMION_Geometry_PLANAR.c` file attached in Appendix A.

In addition to the physical dimensions of the detector, the `GEOMETRY.txt` file also contains the properties of the crystal material necessary to fully describe the detector. These include parameters such as the applied bias voltage, space charge density, dielectric constant and impurity concentration at both ends of the crystal. These properties are necessary when calculating the electric potentials and weighting potentials for the detector.

3.2.2 ADL Fields

Using the geometry defined above in addition to the crystal properties, the electric potential can be calculated using the Poisson equation

$$\frac{d^2\Phi}{dx^2} + \frac{d^2\Phi}{dy^2} + \frac{d^2\Phi}{dz^2} = \frac{-\rho(x,y,z)}{\epsilon_0} \tag{22}$$

where Φ is the electric potential, $\rho(x,y,z)$ is the space charge density and ϵ_0 is the relative dielectric constant. All of these values bar Φ must be provided by the user.

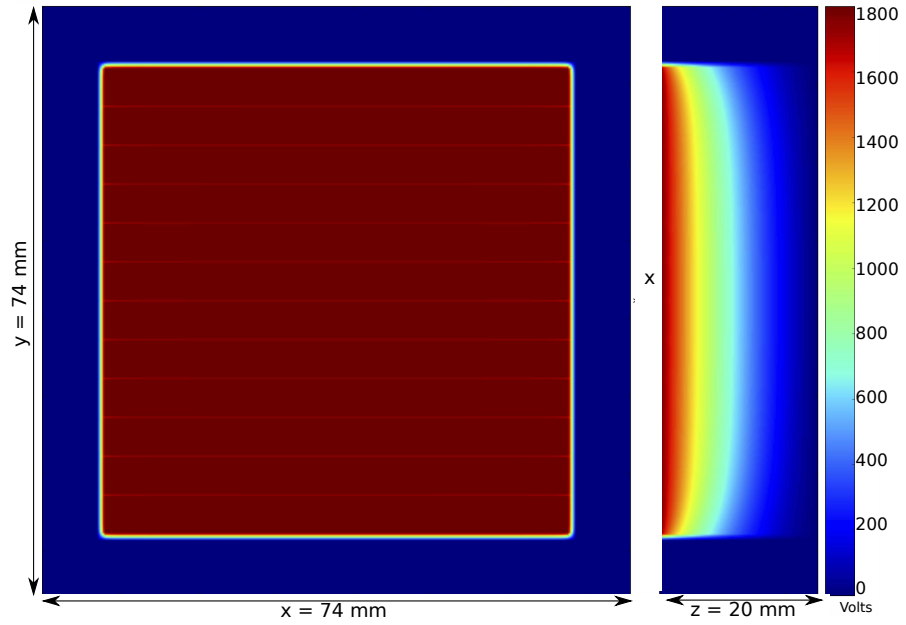

Figure 3.2: Electric potential simulation results for the DSGSD with units in Volts (left) an xy slice through the detector at the biased electrodes and (right) an xz slice through the detector along one of the biased electrodes

The detector was simulated with a bias voltage of +1800 V applied to one set of electrodes, whilst the opposite face was set to 0 V. The electric potential is illustrated in Figure 3.2, which shows an xy slice through the detector at the biased electrode in the left hand image, with the right most image displaying an xz slice through the detector along one of the biased electrodes. These images illustrate the structure present within the detector, with the external guard ring and twelve strips visible.

As we would expect, the simulations demonstrate a decreasing potential as the distance from the biased electrode increases. In addition, the xy cross section shows a uniform potential for a specific depth, with the only exception being the potentials at the top and bottom of the detector, where the potential in the interstrip gap is slightly less than the potential of the electrodes. Although the detector is electronically segmented, the electric potential still mirrors that of a basic planar detector quite closely.

The electric field, E, can be calculated as the gradient at any point in this plot

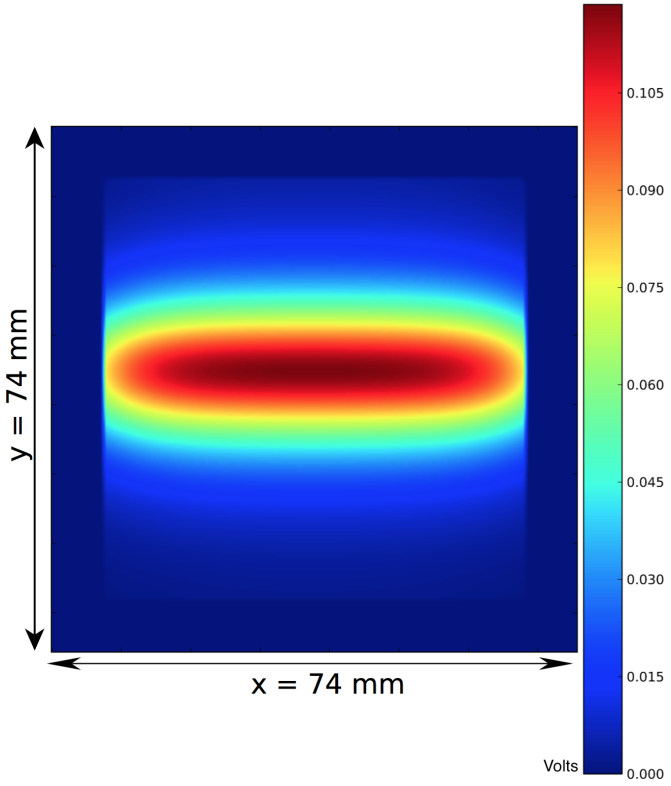

Figure 3.3: Weighting potential simulation results for strip 6 of the DSGSD showing a xy slice through the middle of the detector, with the outline of the strip is clearly visible. Since this slice is taken in the middle of the detector, the weighting field is small and much more diffuse, hence the larger size of the strip and the blurred edges

$$E(x, y, z) = -\nabla\Phi(x, y, z) \tag{23}$$

In addition to the electric potential, the weighting potential and field must also be calculated for each electrode. Where the electric potential can be calculated for the detector as a whole, the weighting field is different for each electrode, therefore 24 weighting fields are required for the simulation. As discussed in Section 2.4.2, the boundary conditions for the calculation are that the electrode of interest is set equal to 1 V with all other electrodes set to 0 V.

The weighting potential for strip 6 of the DSGSD is given in Figures 3.3 and 3.4 with Figure 3.3 showing an xy slice through the centre of the detector, and

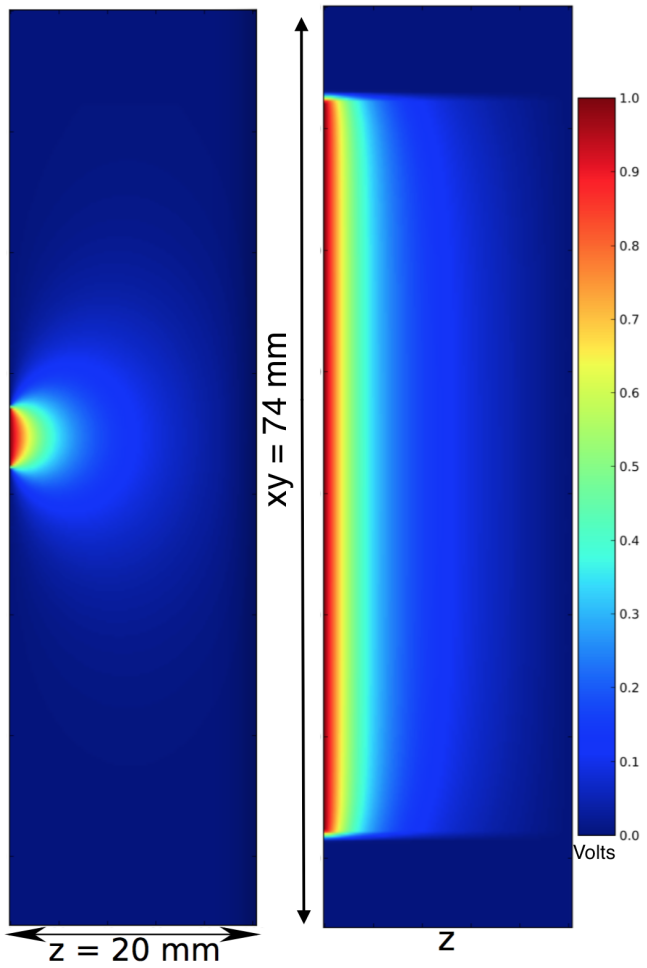

Figure 3.4: Weighting potential simulation results for strip 6 of the DSGSD showing xz and yz slices through the detector. The xz image (left) is cut through the electrode, wiht the yz (right) image cut along the electrode. The xz slice shows a clear radial decrease in potential, with the yz slice acting more like a standard planar potential

Figure 3.4 showing both xz and yz slices through the detector. The outline of the biased electrode can clearly be seen in the xy slice, with the blur and small potential due to the slice being taken in the middle of the detector and not at the electrode. The xz slice in Figure 3.3 shows a radial decrease in the potential as the distance from the electrode increases, with the yz slice almost mirroring the electric field, displaying the behaviour expected from a simple planar detector.

ADL uses these potentials to track charges as they move towards the electrodes. This is done using an iterative process, where the position of the interaction is set as pos(x_0,y_0,z_0). From here the simulation calculates the field strength and direction and moves the charge carriers accordingly for a predefined time step. This gives a new position, pos(x_1,y_1,z_1), which can then be used to recalculate the field strength and move the charges to the next position. Both the time step and the number of steps are user defined and should be long enough to ensure both charge carriers have drifted to their respective electrodes.

The charge induced on each electrode is given as a function of the time step used in the calculations. The results are output in an ASCII format text file, with the real charges on each electrode as well as any transient charges on electrodes adjacent to the real charge provided. A full pulse shape database can be created by simulating interactions for each position within the crystal volume using a 1 mm grid. Due to the size of the charge cloud generated in germanium, a 1 mm grid is the smallest grid size that is necessary for PSA [28]. This was performed for the detector used in this work resulting in 62658 (59×59×18) unique positions. Pulses were generated for all positions, however those at the boundaries displayed strange behaviour with incomplete charge collection. This issue was not fully investigated due to time constraints, however for future work this should be studied further to gain a deeper understanding of the charge transport at these extremes.

3.3 ADL Pulses

The charge pulses calculated in ADL require a few steps of post processing before they are comparable to real pulses acquired in the lab. Firstly, the preamplifier re-

sponse function must be simulated and applied to all pulses in the database. From here, the pulses must be normalised to enable a grid search to be performed. Since the simulated pulses contain no noise, the traces can be normalised to the maximum single channel amplitude. This is not the case for experimental pulses, with a 5-bin average required to estimate the amplitude of the pulse, thus explaining the fact that the experimental traces can be larger than one.

3.3.1 Pre Amplifier Correction

The easiest way to measure the response of a preamplifier is to inject a test pulse and measure the output. Unfortunately, for the detector used, this was not an option due to there being no pulser input on the cryostat. The developers of the detector, CANBERRA, performed tests using a PSC823 preamplifier, identical to the one used in the strip detector. From their tests [29], the typical risetimes with the test pulser were $\sim$ 50 ns with a decay time of $\sim$ 50 μs.

The output from ADL provides the rate of charge collection from the electrodes, however the effects of the preamplifier are not included. The output of the preamplifier is given by Eqn 24, where V(t) is the output voltage, I(t) represents the input current and R(t) is the preamplifier response function

$$V(t) = \int_0^t I(t - t') \cdot R(t')dt' \tag{24}$$

The preamplifier response function is derived from a Sigmoid fit to the pulser output

$$R(t) = g \cdot \frac{1}{1-c} \left(\frac{1}{1 + \frac{(1-c)}{c} \cdot \exp(-b \cdot t)} - c \right)^{\frac{-t}{t_d}} \tag{25}$$

where g is the gain, b represents the rise of the pulse and c determines the point at which the curvature changes in the shape of the signal. The effects of this correction are illustrated in Figure 3.5 for the hit segments as well as the transient charges in the neighbouring electrodes.

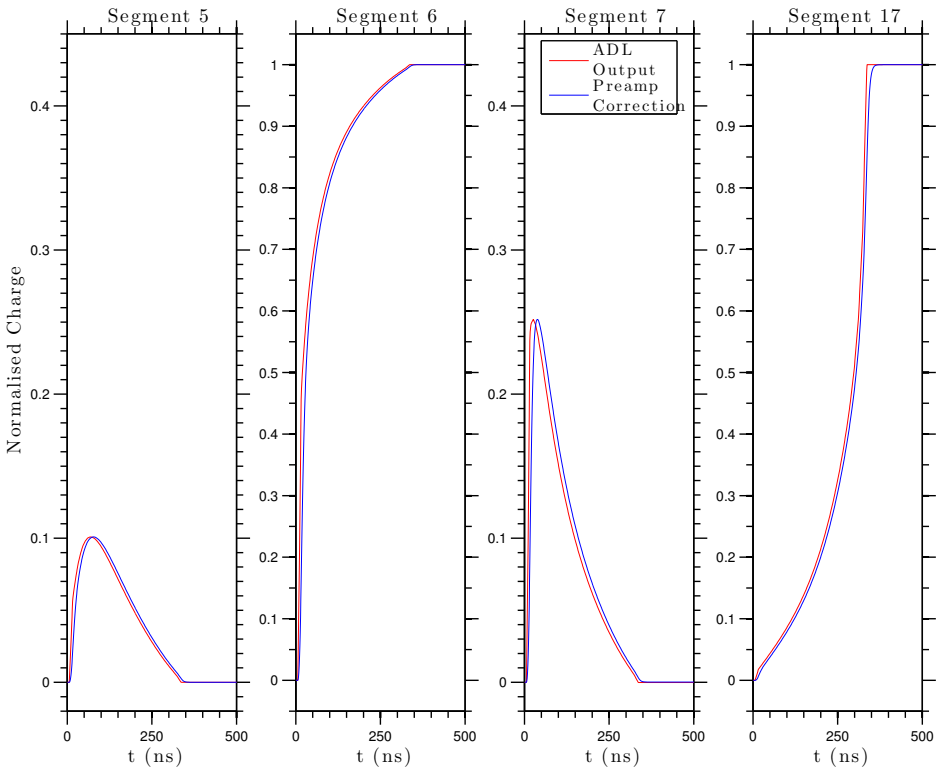

Figure 3.5: Preamplifier corrections to the normalised output from ADL for electrodes detecting a charge in addition to the neighbouring electrodes showing transient charges. The correction acts to smooth the curves in addition to elongating the decay of the charge pulses

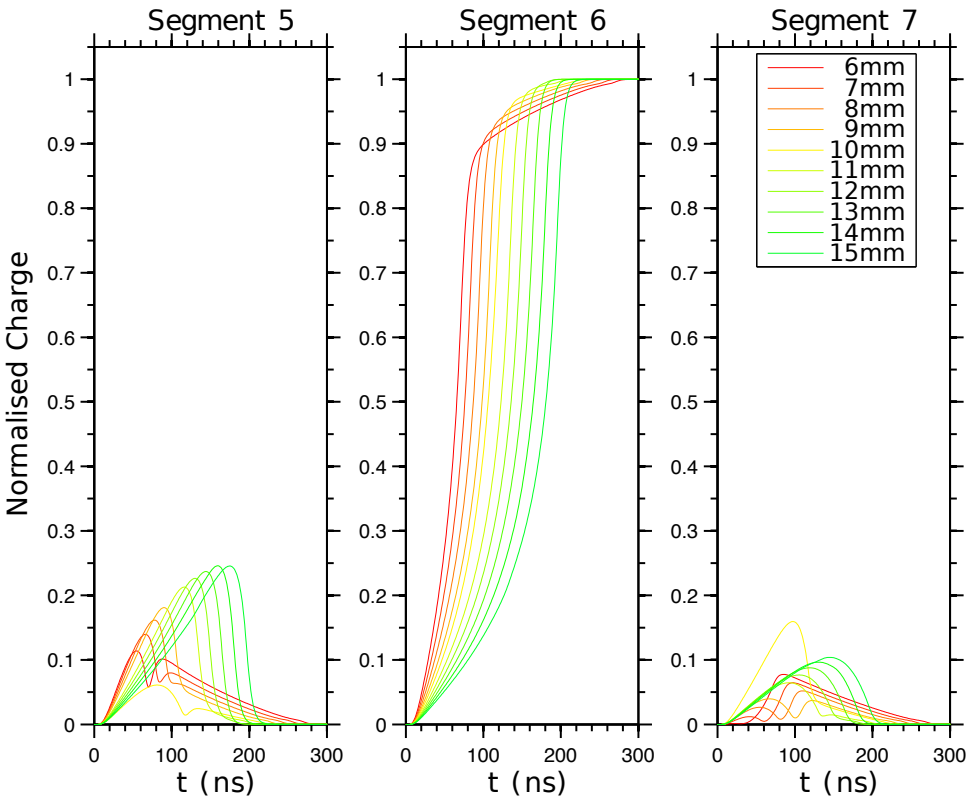

Figure 3.6: Evolution of pulse shapes with varying depth of interaction for the charge collecting electrode and each direct neighbouring electrode

3.3.2 Pulse Shape Evolution

As mentioned earlier, the purpose of this simulation is to observe changes in the charge pulse shapes when varying the position of the interaction. Figure 3.6 shows the effects of depth on the pulse shapes produced for ten positions in the detector. The lateral positions (x & y) were kept constant with the depth (z) varying as indicated in the legend.

The kink in the pulse represents the two different charge carriers being collected at the corresponding electrodes, with the difference in drift velocities evident by the position of the kink. Figure 3.6 clearly shows the change in charge collection time for the individual carriers as the distance from the collecting electrode alters, physically representing the change in distance with which each carrier must travel.

3.3.3 Grid Search Algorithm

Pulse Shape Analysis (PSA) can be categorised into one of two techniques; Parametric PSA and Basis PSA. Parametric PSA utilises the variation in charge pulse risetime characteristics associated with differing positions, in addition to the changing magnitudes of image charges. For Basis PSA, a pulse shape database is generated, either experimentally or via simulation, with each experimental pulse then compared to traces from the database. A Figure of Merit (FoM) minimisation technique is then applied to find the best match, this will be discussed in more detail below.

For the event selection utilised in this work, the ability to study multiple interactions within the same segment is important for improving the efficiency of the measurements. This requires the deconvolution of pulses, something that can only be achieved through the use of Basis PSA. For the Basis PSA to work, experimental pulses are compared to theoretical pulses and a figure of merit is calculated as

$$\text{Figure of Merit} = \sum_{i,j} |A^m_{i,j} - A^s_{i,j}|^2 \tag{26}$$

where A^m and A^s are the measured and simulated signal amplitudes respectively. The i component accounts for the sum over the relevant timescale, with j acting to sum over the number of segments. In essence, this is a minimisation technique, with the lowest value for the FoM representing the pulse most similar to that measured and hence the most likely interaction position. For each interaction, real charges are generated in two strips, with image charges generated in the neighbours. Since the image charges change depending upon the interaction position, the FoM is calculated using six traces, two real traces plus the four nearest neighbour image charges. For interactions occurring in edge strips, only one image charge was compared; this resulted in a five or four trace comparison for interactions occurring at edge strips on one or both faces respectively.

For large pulse shape databases, this process can be very time consuming. To reduce the computational time required, the search can be performed on two

separate grids. The first search is performed on a broad grid in order to locate the rough position. Following this, a fine search is performed on the region of interest to locate the interaction position more precisely. Due to the construction of the detector used in this work, the rough grid search is unnecessary due to the segmentation of the detector. Since the position is already known to be within a $5 \times 5 \times 20$ mm^3 volume, the pulse shape comparison needs only be performed in this region. This drastically reduces the computational time required to perform a search, with the database being reduced from 62658 pulses to just 500 pulses.

In order to compare experimental pulses with simulated pulses, a few considerations must be made. Firstly, each channel from the ADC is sampled at 10 ns intervals, however the simulated pulse shape database was constructed using 1 ns intervals. In order to compare the two, both must be on the same scale, with an equal number of bins. To correct for this, the experimental pulses were put through an interpolation code. This expanded each channel into 10 and then performs a 3-bin moving average to smooth the shape and allow intermediate values instead of a 10 bin step. For future work, the time scale used would mirror that of the experimental work and not the simulated data. This prevents the "creation" of data and maintains the integrity of the real data set, thus preventing inaccuracies from being introduced through interpolation.

One other consideration when comparing pulses, is the fact that experimental results will not necessarily be time aligned. This will result in meaningless comparisons, since the comparison is done on a time basis. To fix this, a 5-bin moving window average was calculated from the start of the trace to the calculated t_{10}, where t_{10} is defined as the time taken to reach 10% of the maximum charge amplitude. Once this average passed a threshold value, larger than the average noise, the starting bin was taken as t_0. All pulses were then aligned at $t_0 = 6$ ns to coincide with the alignment of the simulated database.

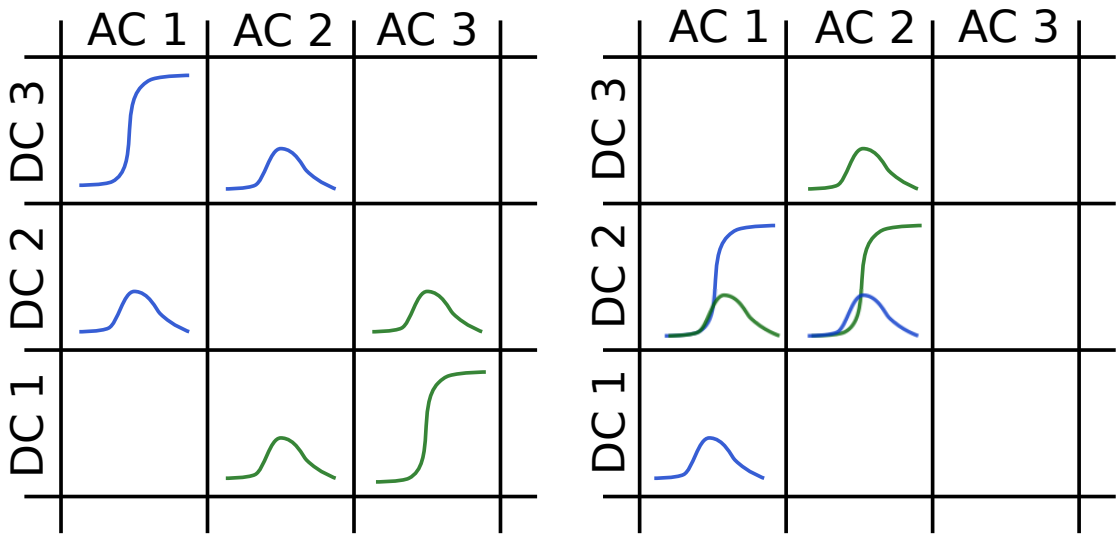

Figure 3.7: Schematic showing the effects of interactions occuring in neighouring strips, with (left) the pulses clearly distinguishable from one another and (right) the convolution of image charges and real charges

3.3.4 Multiple Interactions

The above methodology describes the process of searching for single interactions, however for the work in this thesis, we are only interested in multiple interactions. In order to recreate a Compton event, two interactions are required (as explained in Section 2.5), thus making the task of comparing experimental and simulated pulses more difficult. The major source of complication lies in the image charges generated on neighbouring strips when an interaction occurs. These image charges are useful for improving the precision of the grid search algorithm. However when multiple interactions occur in nearby strips, signals from separate interactions can convolve with one another, reducing the clarity of the pulse. This is shown in Figure 3.7, with the convolution of image charges and real charges clearly visible for interactions in neighbouring strips.

Image charges are generated when a charged particle moves through the weighting potential of any electrode. As the charge moves towards increasing potential, the charge generated increases relative to the gradient of the potential. Following this, the opposite effect is observed as the charge moves towards a smaller

potential, with the cumulative image charge on the electrode reducing back to zero. In practice, image charges are only observed on the strips closest to the charge collecting electrode, with the intensity decreasing rapidly with increasing distance from the hit strip. The closest electrodes will show significant image charges, whose intensity is $\sim 10 - 20\%$ that of the charge collected, depending upon their proximity to the interaction position. This is reduced greatly for the next strip, with the intensity peaking at a few %. This rapid decline in intensity means that only interactions closer than three strips apart will significantly affect one another. One consideration to be made is in the case where the two interactions are substantially different in energy. In this scenario, the image charges from the higher energy interaction may be larger than the real charge from the lower energy interaction, thus increasing the chances of signal convolution. To account for this, the data were sorted to only output interactions whereby the first and second interactions were greater than two strips apart on both the AC and DC faces. This enabled each pulse to be compared directly to the database, however the side effect was a drop in efficiency (from $7.2\% \rightarrow 0.5\%$ of total events detected).

Methods exist to deconvolve the individual components from summed pulses, thus enabling interactions on neighbouring strips to be analysed. Future work on this project would look into developing new algorithms capable of utilising these techniques, thus improving the efficiency of the process. In addition, simulations are presented in Chapter 5.1 which present the potential performance of the system with position information of varying levels and perfect pulse deconvolution.

3.3.5 Experimental Pulses

As mentioned earlier, noise is a concern when analysing experimental pulses, with the baseline RMS noise levels for this work being approximately $\pm$ 2mV. The Canberra PSC823 preamplifier has a gain of 200 mV/MeV, giving a noise level in keV of $\pm$ 10 keV. The noise level in the pulses is of larger concern for lower energy signals than higher energy signal, due to the relative contribution in the

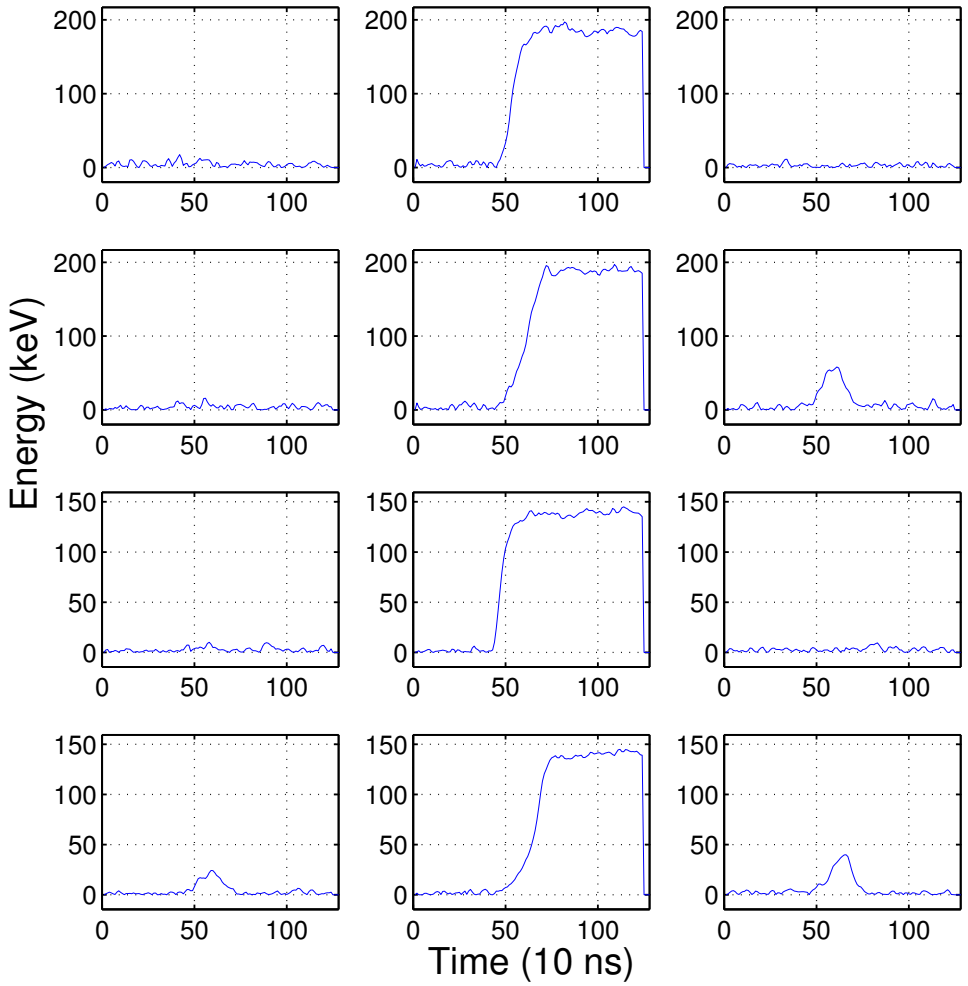

Figure 3.8: Raw experimental pulses for the 344 keV decay from ^{152}Eu showing the four hit strips resulting from a fold 2-2 interaction in addition to the image charges generated either side of the hit strip

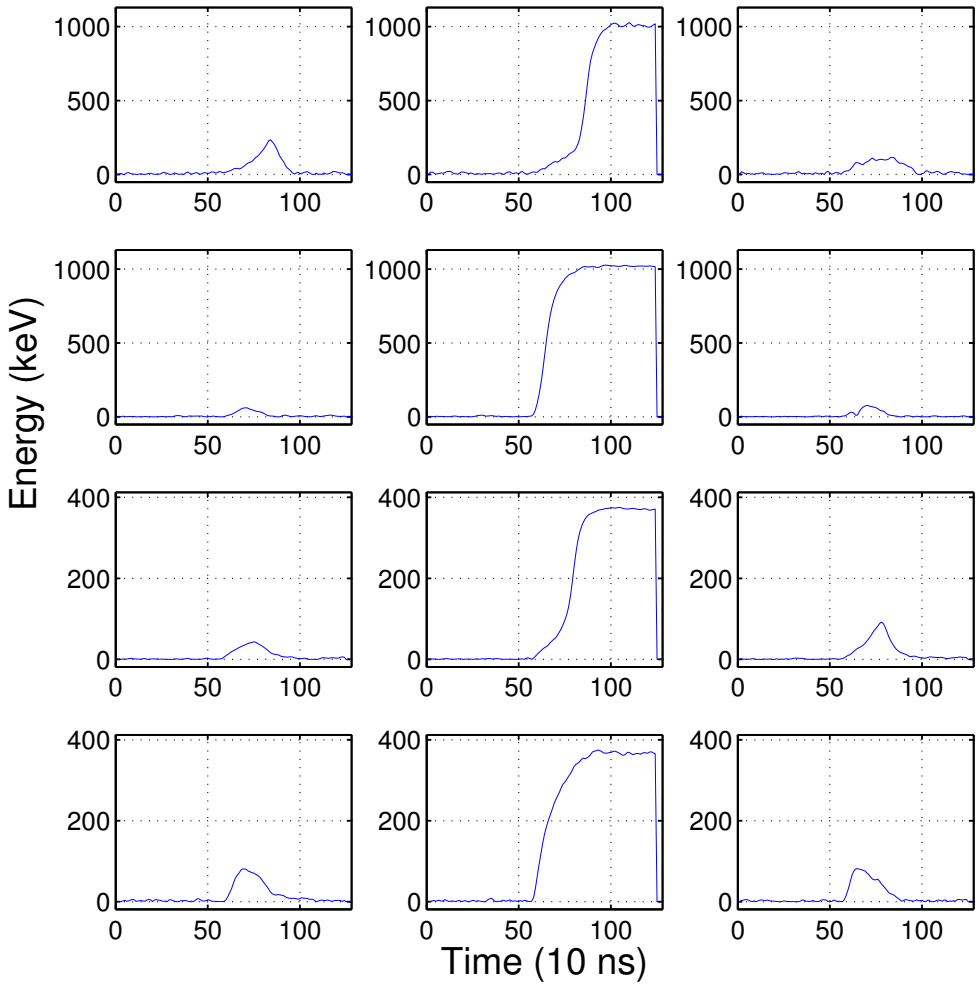

Figure 3.9: Raw experimental pulses for the 1408 keV decay from ^{152}Eu showing the four hit strips resulting from a fold 2-2 interaction in addition to the image charges generated either side of the hit strip

signal-to-noise ratio.. The effects of this can be seen when comparing signals from the 344 keV ^{152}Eu decay shown in Figure 3.8, to those from the 1408 keV decay of the same nuclide shown in Figure 3.9. Shown in these figures are the four pulses from the hit segments, 2 AC + 2 DC, along with the respective image charges generated on the nearest neighbour strips. All image charges have been displayed on the same scale as their corresponding pulse.

These figures clearly show that for the higher energy signals, the noise level is completely drowned out by the amplitude of the pulse, however for the low intensity signals generated from the 344 keV γ-ray interactions, the noise significantly reduces the quality of the signal. This reduction in signal-to-noise ratio has a knock on effect on pulse processing, making it much more difficult to quantify the signal properties and thus more challenging to align the pulses correctly. This in turn affects the grid search algorithm, with poorly aligned, noisy pulses resulting in larger FoM fits for matching traces. This leads to the conclusion that the grid search algorithm will perform better for larger signals, however the efficiency of the detector will also be reduced for these high energy signals.

Figure 3.10 shows the results of a grid search performed on pulses generated by a 778 keV γ-ray from ^{152}Eu. Displayed in blue are the experimental pulses from the hit AC and DC strips, in addition to the neighbouring image charges generated. The red lines represent the simulated ADL pulses which were found to be the closest match when using the grid search algorithm, returning a FoM/d.o.f. of 0.48.

The variation in pulses as a function of time can be seen more clearly in Figure 3.11, where the 12 charges generated from a 778 keV Compton event are shown, along with the best matched simulated pulse. In addition to the pulses, a trace for the residual is presented, illustrating the difference between the experimental and simulated pulses as a function of time. This figure shows that the simulations seem to measure the turn over of the real charge pulses incorrectly for most pulses. There appears to be a bipolar effect, where the charge pulse is overestimated from $\sim$80-95% of the pulse height and subsequently underestimated for the remaining

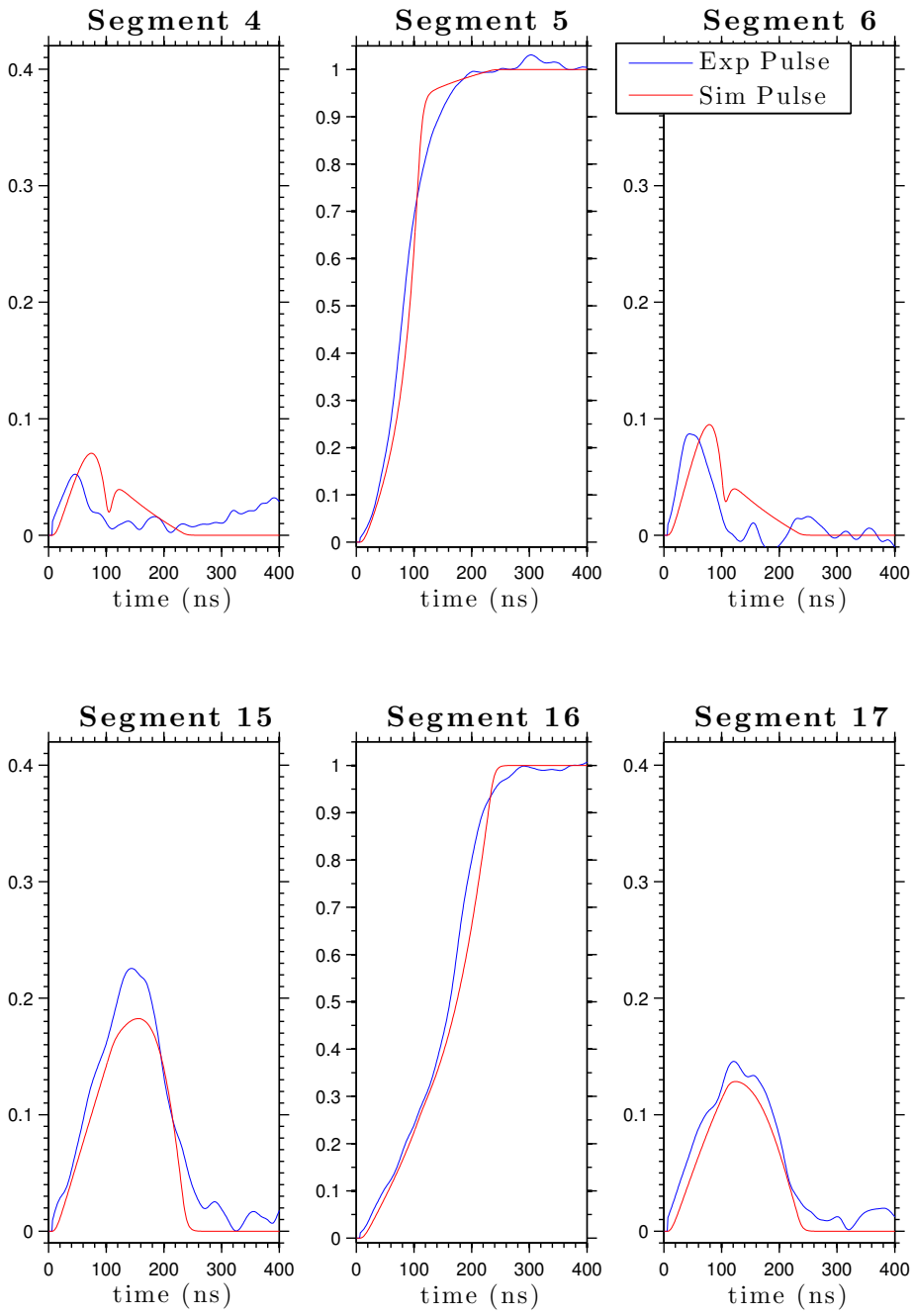

Figure 3.10: Comparison between experimental pulses from hit segments plus neighbouring image charges and the corresponding simulated pulses found through the grid search algorithm. The pulses used were from a 778 keV decay from ^{152}Eu

∼5%. This effect could be the result of electronic effects present in the real data that were not accounted for in the simulations. A better understanding of both the preamplifier and the subsequent electronics chain could help to improve this effect.

For each experimental pulse used in this work, a FoM value was calculated, with a cutoff then applied to remove any pulses with a poor fit to the simulated database. Figure 3.12 displays the distribution of FoM values for all pulses used in the analysis of the 778 keV ^{152}Eu photopeak. As can be seen from Figure 3.12, the majority of events have a low calculated FoM, with nearly 60% having FoM <10. Since the statistics for most of these runs were low, the FoM cutoff was placed at 25 to remove any events drastically different from the simulated pulses, whilst maintaining statistics. This is validated by looking at Figure 3.12 with the slope of the distribution flattening at ∼20-25.

As discussed in Section 3.3.3, a FoM is evaluated for every interaction position within the hit voxel, constrained by the known hit strips. Figure 3.13 shows the variation in FoM as a function of position for x, y and z. For each plot, the two directions not being altered are fixed to be equal to the calculated position, given by the lowest FoM. The lowest value of FoM is highlighted on each plot by a star, with the numerical values for each position given for all values close to the minimum.

For both the x and y directions, the FoM drops drastically as the correct position is approached, however there still exist multiple possible positions with similar values for the FoM. This supports the argument that the position resolution is improved through the use of PSA, however it does not allow the position resolution to be claimed as ∼1 mm. The results for the z variation provide a much stronger case for this, with the FoM at the chosen position drastically different from those around it. From the information present, the x and y position resolution can be assumed to be ∼ 2 mm, with the position resolution in z being ∼1 mm, consistent with the limitations expected from [28].

These results are to be expected, with the electric field variation in z being

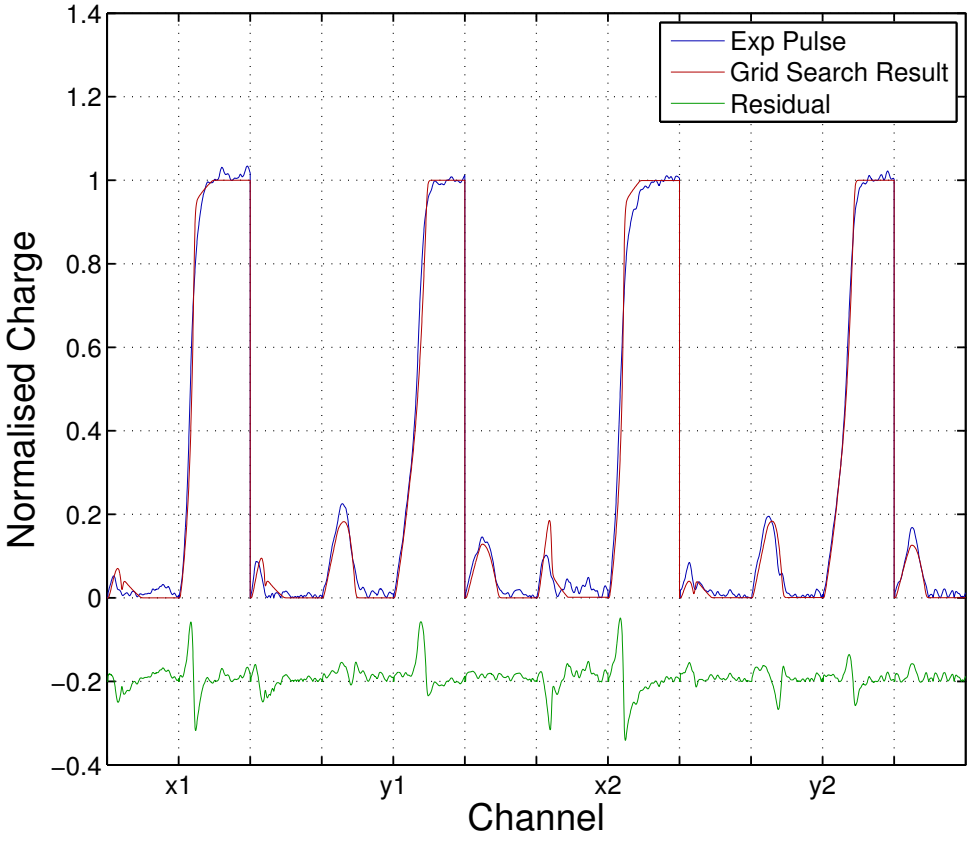

Figure 3.11: Results of the grid search algorithm for a Compton imaged events, showing all 12 charges resulting from a 778 keV γ-ray. Along with the experimental and simulated pulses, is the residual trace, illustrating the variation between the two pulses as a function of time. The residual trace has been offset by -0.2 to improve visibility. The labels, x and y refer to the AC and DC strips respectively, with the numbers describing the order of the two interactions.

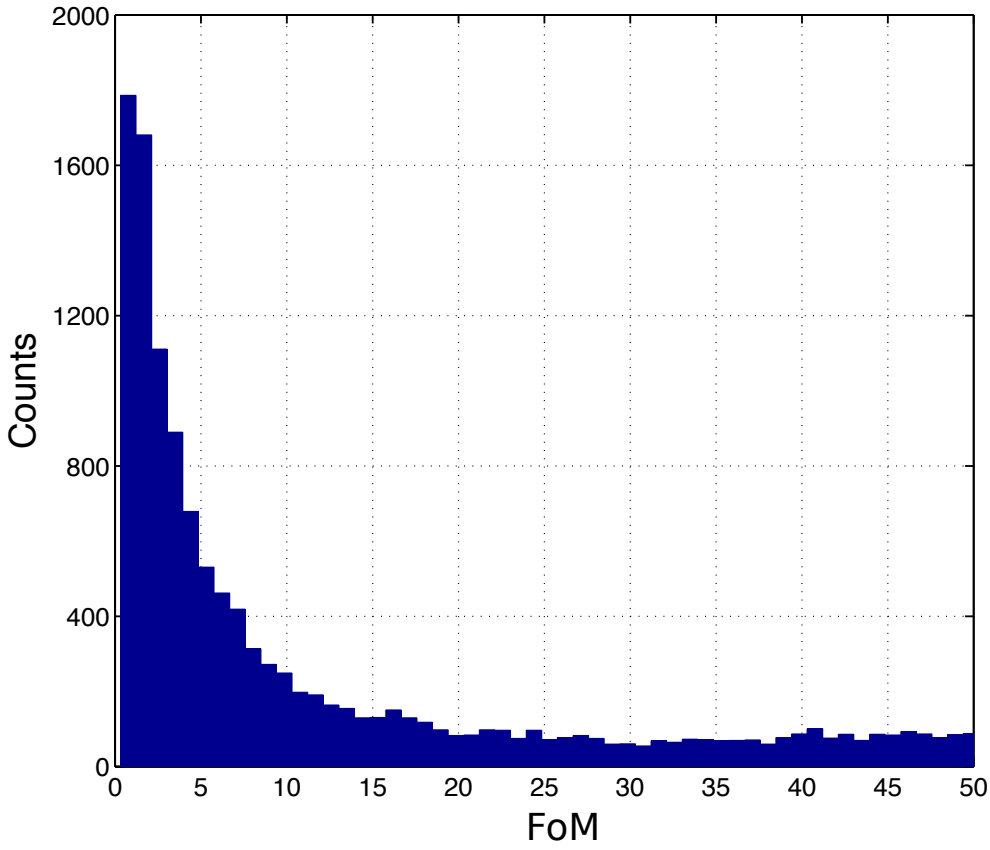

Figure 3.12: Distribution of calculated FoM values for comparison between experimental pulses and the best match from the simulated pulse shape database. Data was generated using the 778 keV ^{152}Eu photopeak

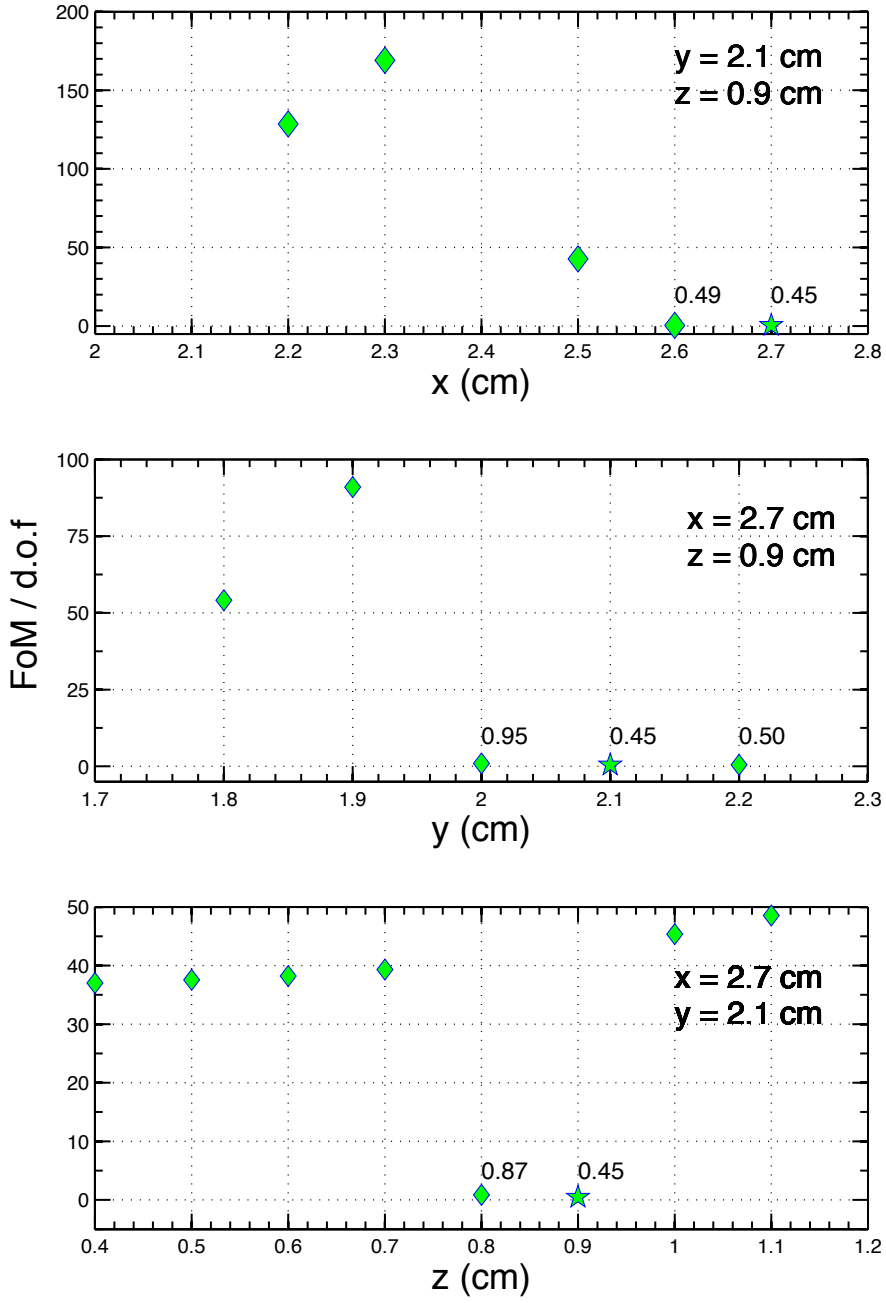

Figure 3.13: Calculated FoM values for the interaction depicted in Figure 3.10, showing the variation in FoM as a function of interaction position. The data point with the lowest FoM is highlighted by a star, with the values for the FoM given for all data point close to the minimum

much greater than that in both x and y. This larger variation results in significant differences between two real charge pulses more than 1 mm apart in z. For both x and y, the real charge pulses are likely very similar for most positions, however the image charges generated will vary significantly. This is where the issues in x and y most likely arise, with Figure 3.10 showing that the image charges for many of the low energy interactions are not significantly above the noise of the detector. Further work to improve the noise and thresholds used could increase the signal-to-noise ratio for the image charges and in turn enable better position sensitivity in x and y.

4 Compton Imaging Results

Results are presented for the capability of single element Compton imaging with a DSGSD. Compton images were generated for seven different γ-ray energies ranging from 121 keV to 1408 keV, using experimental data acquired from ^{152}Eu and ^{60}Co radioactive sources. The effects of PSA on the Compton reconstruction are demonstrated for each γ-ray energy, with further analysis using a Monte Carlo simulation provided in Chapter 5.

The ability to reconstruct a Compton image based upon the position and energy deposition for two interactions from a single γ-ray within a detector system is a well documented process [18]. The position resolution of the final image depends on the accuracy with which the position and energy of interactions within the detector are known. The errors in the energy measurement are consistent throughout the detector volume and described by the energy resolution of the detection medium, with the FWHM increasing with increasing γ-ray energy. Unlike energy, the angular error resulting from the positional resolution for the interaction location is relative to the distance between the two interactions. This is a purely trigonometric problem, whereby increasing the distance between the two interactions results in a smaller angular error carried forward from the positional uncertainty. For the DSGSD used in this work, the necessity for two interactions to occur within the same detector volume, results in a very small distance between interaction positions. This small separation increases the importance of accurately locating the interaction position.

For the results presented without the application of PSA, each interaction was taken to be at the centre of the voxel, giving a positional uncertainty of $\pm\,2.5 \times 2.5 \times 10$ mm in x, y and z respectively, where x and y describe the face of the detector, with z representing the depth of detector/distance to source. Events were reconstructed using an analytical approach [30, 31] whereby cones were back projected using an angle defined by the location and energy deposition of two interactions, as governed by the Compton scattering equation, Eqn 3. The imaging code utilised for the reconstruction was unable to process results with

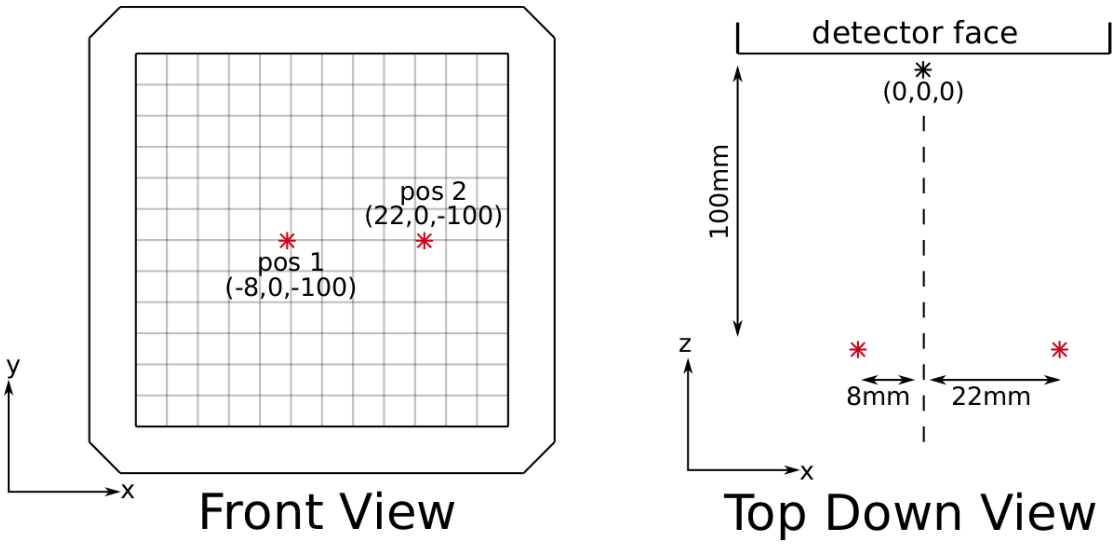

Figure 4.1: Experimental setup indicating the source locations used with the coordinate system setup relative to the centre of the detector face

$z_1 = z_2$ ($\theta = 90°$), due to the axis of reconstruction being perpendicular to the projection axis. This results in the inability to project the reconstructed cones into the z direction. To resolve this, each z was offset by 1 mm either side of centre. The first interaction was taken as the shallower of the two, giving $z_1 = 9$ mm and $z_2 = 11$ mm, this is discussed in more detail in Section 4.1.1.

4.1 Experimental Compton Camera Measurements

Experimental measurements were taken using two different radionuclides, ^{60}Co and ^{152}Eu. The first nuclide, ^{60}Co, contains two discreet γ-decays, one at 1173 keV and the other 1332 keV, both of which were studied in this work. Secondly, ^{152}Eu contains many discreet γ-decays, however only five were used in this thesis, 121 keV, 244 keV, 344 keV, 778 keV and 1408 keV. The data were acquired with each source positioned near the centre of the detector face, at a distance of 100 mm from the detector face cap, pos 1 in Figure 4.1. Additional data were taken at a different position, pos 2, for ^{152}Eu only. The second position was located 30 mm to the side of the first as shown in Figure 4.1. The purpose of the second data set was to test the position response of the reconstruction, testing whether

Table 4.1: Details of the experimental runs used in this work

Run #	Source	Position	Data (Gb)	# of Events
R_{30}	^{152}Eu	Pos 1	230.4	3.58×10^8
R_{32}	^{152}Eu	Pos 2	650.6	8.06×10^8
R_{38}	^{60}Co	Pos 1	1600	2.49×10^9

the source moved correctly in the reconstructed images.

The experimental data were taken over the course of five days at the University of Liverpool, with details of the experimental runs provided in Table 4.1. CAEN 1724 digitiser cards [23] were used to process the preamplifier signals, information on their functionality is provided in Section 2.5.3. Digitised pulse shapes were stored for each interaction, with 128 samples using 10 ns intervals. A hardware trigger of 40 keV was used when taking the experimental data, in addition to a 10 keV software trigger used when sorting the data post experiment.

4.1.1 Data Sorting

In order to analyse the data set, a sort must be applied to select the events of interest. A sort is merely a computer program written to arrange data packets into more accessible formats, in addition to providing a basis for preliminary analysis. Firstly the data were sorted to only include fold 2-2 events, whereby two interactions were detected on both the AC and DC faces of the detector. Secondly, the summed energy for the two interactions were calculated, known as the addback energy. From here, gates were placed on addback energies equal to γ-decays associated with the radionuclides of interest, where a gate is defined as a predefined range of accepted values for a given variable. After all gates have been applied, the energy resolution of the peaks in the addback spectra were reduced to FWHM = 9 keV at 121 keV and FWHM = 10 keV at 1408 keV. With this in mind, gates on the energy were defined to be $E_\gamma \pm 10$ keV. For a Gaussian distribution, the FWHM is equal to 2.35σ, therefore the gates placed represent a 2.61σ and 2.35σ range respectively. This equates to > 98 % of the peak events being measured for

all energies.

A software threshold was placed in the sort program to ensure each event had at least one real charge detected on one of the strips. This threshold acts to prevent random noise from being processed as a real charge signal. In a typical two detector Compton camera system, the majority of events in the scatter detector are low energy deposits due to the small angle of scatter for events of interest. This results in a need to set the software threshold as low as possible to increase efficiency. However for the events of interest in this work, the minimum scattering angle possible is $\sim 35°$, see Figure 4.5. This results in much larger energy deposits in the scatter detector, and it can be shown using the Compton scatter equation that for all initial γ-ray energies above 244 keV, the minimum energy deposit will be greater than the 10 keV threshold. Of the energies studied, only the 121 keV γ-rays will experience a reduction in efficiency due to the software threshold.

Each candidate event results in four real charges being collected and two pairs of distinct energies being measured. The four strips must be correctly paired to create two interaction positions. By comparing the energies, each strip can be matched to its partner, revealing the voxel within which the interaction occurred. As mentioned in Section 3.3.4, only interactions with a distance greater than two strips were accepted to remove the interference caused by neighbouring image charges. Additionally, increasing the distance between interactions results in a smaller error when calculating the scattering angle from poor positional resolution.

Without the application of PSA, there is very little information regarding the depth of each interaction. This causes problems when trying to discover the order of the γ-rays, with two interactions occurring in coincidence within the same detector volume. To resolve this, the Compton scattering equation, Eqn 21 was used to calculate the minimum scattering angle required for the energy of the scatter to be larger than the absorbed energy, E1 > E2. For E1 = E2,

$$\theta = cos^{-1}\left(1 - \frac{m_0 c^2}{E_\gamma}\right) \tag{27}$$

which provides a lower limit on the initial γ-ray energy required of

Table 4.2: Minimum scattering angles required for $E1 \geq E2$ calculated for transtitions in both ^{152}Eu and ^{60}Co

Energy	θ_{min}
121 keV	N/A
244 keV	N/A
344 keV	119.04°
778 keV	69.93°
1408 keV	50.43°
1173 keV	55.64°
1332 keV	51.95°

$$E_\gamma \geq \frac{m_o c^2}{2} \tag{28}$$

showing that for all γ-rays below 255.5 keV, it is impossible for the energy deposited in the scatter to be larger than that in the absorber. This means that for all events resulting from either the 121 keV or the 244 keV decays from ^{152}Eu, the lowest energy measurements are always assigned to the scatter interaction. Results of this calculation are presented in Table 4.2 for all seven ^{152}Eu and ^{60}Co γ-rays studied in this work.

As can be seen from Table 4.2, the minimum scattering angle for E1 $>$E2 is very large for 344 keV and then drops significantly for 778 keV and higher. For this reason, the results for 344 keV were treated the same as the lower energy γ-rays discussed above, with the scattering interaction taken to be the lowest energy deposit of the two. For all energies above 778 keV, the scattering angle was considered sufficiently low that the majority of events would scatter through larger angles and thus the energy deposited in the scatterer would be larger than the energy measured in the absorber. For the results without PSA, this was the assumption used, with the highest energy deposition taken as the scatter.

For the results with the application of PSA, more information was available regarding the depth of each interaction. This information, combined with more

Table 4.3: Calculated efficiencies for Compton imaging selection and reconstruction process for R_{38} ^{60}Co dataset

Gate	# of Counts	Efficiency
Total Events	2.49×10^9	
Fold 2-2	2.23×10^7	0.89 %[1]
Strip Separation $\leq$ 2 Strips	1.67×10^7	75.0 %[2]
Strip Separation $>$ 2 Strips	1.19×10^6	5.3 %[2]
Compton Events - 1173 keV	8.22×10^4	0.0033 %[1]
Compton Events - 1332 keV	6.96×10^4	0.0028 %[1]

[1] Relative to total number of events
[2] Relative to number of Fold 2-2 events

precise lateral position information, enabled a scattering angle, θ, to be calculated for each event using

$$\theta = tan^{-1}\left(\frac{\sqrt{(x_1-x_2)^2+(y_1-y_2)^2}}{|z_1-z_2|}\right) \tag{29}$$

where x, y and z are the coordinates found through use of the grid search algorithm. By comparing this to the minimum scattering angle in Table 4.2 for each specific decay, the interaction order was assigned on an event by event basis, thus improving the quality of the dataset.

4.2 Experimental Efficiency

Gates are applied to the data set to select Compton events of interest, as discussed in Section 4.1.1. These gates significantly reduce the volume of data available, where the efficiency of this selection process can be calculated as

$$\epsilon_{\text{selection}} = \frac{\text{No. of events after gates}}{\text{No. of events before gates}} \times 100 \tag{30}$$

Table 4.3 shows the calculated efficiencies for each step in the selection process relative to the initial number of events detected by the detector. As can be seen, the requirement for AC and DC strip separation to be greater than two strips

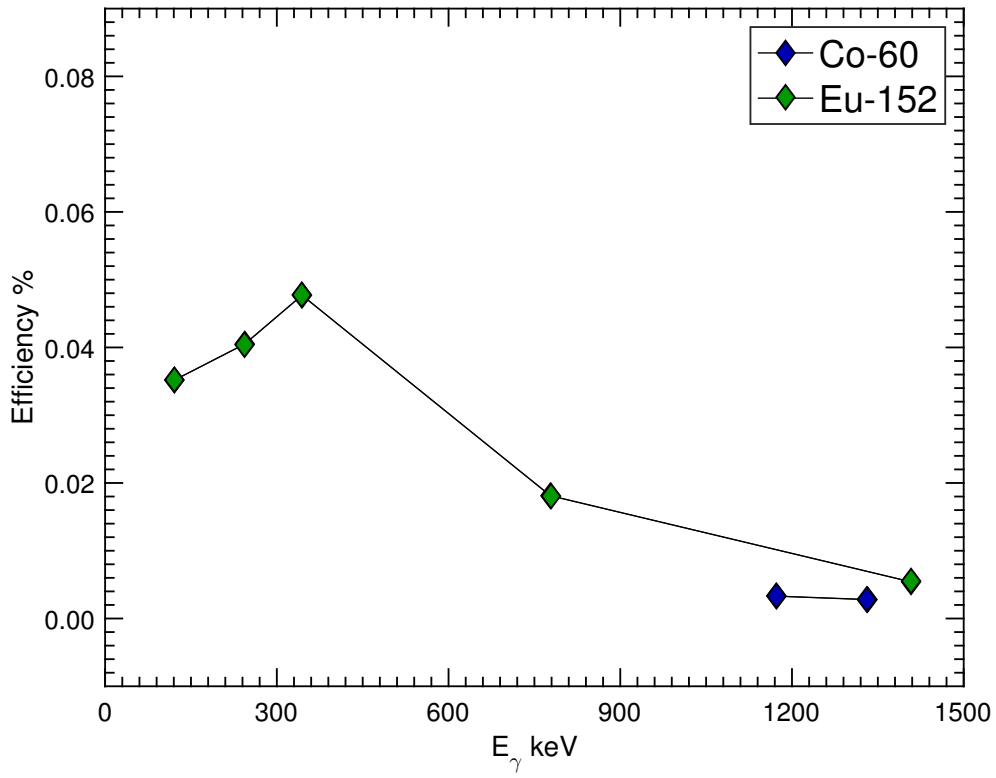

Figure 4.2: Efficiency calculations for fold 2-2 events passing all gates as a function of initial γ energy. Errors are included, however they are too small to see. A list of values is provided in Table 4.4

significantly reduces the efficiency, with only 5 % of fold 2-2 events passing this gate. The remaining 19.7 % of fold 2-2 events are those where $AC_{sep} > 2$ and $DC_{sep} \leq 2$ or vice versa. Multi fold events only count once towards all of the tallies presented in Table 4.3. Similar efficiency calculations were performed using seven different γ-ray energies ranging from 121 keV to 1408 keV. The results presented are for events passing all gates; fold 2-2, xydiff $>$ 10 mm and E = E_γ, with the results presented in Table 4.4 as well as graphically represented in Figure 4.2.

The ^{152}Eu data displays the behaviour that we would expect, with a slight increase from low to intermediate energies followed by a decrease towards high energy. For low energy γ-rays, total photoelectric absorption is the most favoured interaction method, therefore fold 2-2 Compton scattering interactions are less

Table 4.4: Calculated efficiencies for Compton imaging selection for varying γ-ray energies. All data were calculated at position 1 using runs R_{30} (^{152}Eu) and R_{38} (^{60}Co)

E_γ (keV)	$\epsilon_{\text{selection}}$ %	$\Delta\epsilon$ ($\times 10^{-3}$)
121.78	0.0352	0.2089
244.70	0.0405	0.2242
344.28	0.0477	0.2434
778.90	0.0181	0.1499
1173.24	0.0033	0.0115
1332.50	0.0028	0.0105
1408.01	0.0054	0.0819

likely. In addition, events which do scatter in the first instance are likely to interact within 10 mm of the first interaction thus being lost to the xydiff $>$ 10 mm gate. At intermediate energies, the first interaction is most likely a Compton scatter, with the reduced energy second interaction favouring photoelectric absorption, resulting in fold 2-2 events. For high energies, the first interaction is still likely to be a Compton event, however the resulting γ-ray still possesses a large amount of energy, thus decreasing the likelihood of photoelectric absorption within the detector volume with the mean free path for a 500 - 1000 keV scattered photon being greater than 1 cm. The two γ-rays from the ^{60}Co data follow the trend of the ^{152}Eu data, with a decrease in efficiency as the γ-ray energy increases, however they do appear to lie slightly above what would be expected from looking at the 1408 keV data point.

Figure 4.3 shows the efficiencies for different AC/DC fold variations, where fold is defined as the number of unique strips firing as a result of a single initial γ-ray. These results were calculated using the R_{32} ^{152}Eu and R_{38} ^{60}Co datasets, with all values normalised to the total number of events for each run. The results are displayed in a numerical form in Table 4.5. By studying both nuclei, we can get an idea of the effects of γ-ray energy on the likely fold. The γ-rays from ^{60}Co are

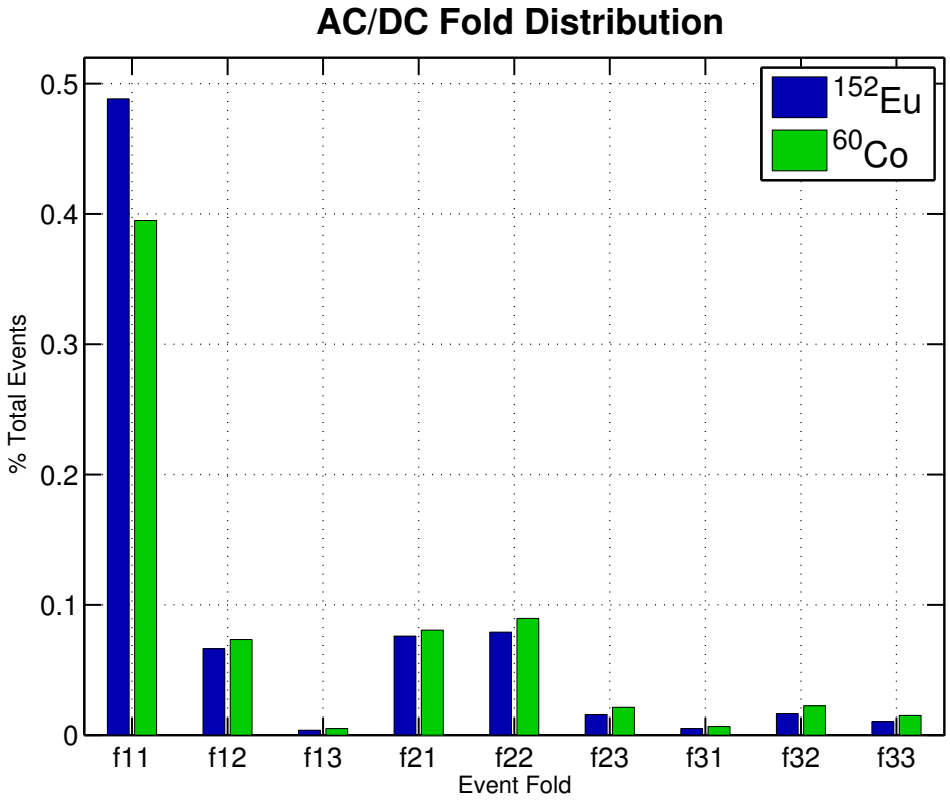

Figure 4.3: Histogram showing efficiencies for different AC/DC fold variations as a fraction of the total number of events. Results are shown for both ^{152}Eu and ^{60}Co, calculated from the R_{32}/R_{38} datasets respectively, with no gates placed on the γ-ray energy

Table 4.5: AC fold vs DC fold for ^{152}Eu/^{60}Co respectively as a percentage of the total events for each dataset. Data calculated using the R_{32}/R_{38} datasets respectively

		AC		
	Fold	1	2	3
	1	48.8/39.5 %	6.6/7.3 %	0.4/0.5 %
DC	2	7.6/8.1 %	7.9/8.9 %	1.6/2.1 %
	3	0.5/0.6 %	1.7/2.3 %	1.0/1.5 %

both high in energy, meaning the likelihood of photoelectric absorption is reduced when compared to the low energy photons present in a ^{152}Eu spectrum. This is reflected in Figure 4.3, with the chance of a fold 1-1 interaction being over 9% higher for ^{152}Eu. This effect is reversed as the γ energy is increased, with higher fold events more likely in ^{60}Co.

4.3 Cobalt 60 Results

Images were generated using the ^{60}Co dataset, R_{38}, located in pos 1 (see Figure 4.1). Using a ^{60}Co source with an activity of 52 kBq, at a distance of 100 mm, gives a count rate of $\sim$ 5,000 cps. Figure 4.4 shows the γ spectrum for varying stages of the sort process, from the raw data from a single strip to the summed gated spectra. One interesting feature in Figure 4.4 is the shift in γ-ray energy from the top and bottom spectra to the middle spectrum. When looking at the 1173 keV peak, the centroid shifts from 1173 keV $\rightarrow$1181 keV $\rightarrow$ 1173 keV, with the same feature seen for the 1332 keV peak (1332 keV $\rightarrow$ 1341 keV $\rightarrow$ 1332 keV). This can be attributed to proportional crosstalk, which is defined as a coupling between electronic channels. This effect causes shifts in the baseline of neighbouring strips, which can have the effect of increasing the measured energy, in addition to increasing the FWHM of the peak. This is confirmed in the bottom spectrum, with the requirement for strip separation to be greater than two strips removing the effects of crosstalk and thus correcting the peak energy. Proportional crosstalk

is a linear process and is a function of the initial γ-ray energy. From the changes in energy for both γ-rays in ^{60}Co, the magnitude of the proportional crosstalk is calculated to be ~ 0.7 %. It is worth noting that this value is consistent with similar geometry detectors such as the SmartPet detectors [32] also studied at the University of Liverpool.

From the experimental run, 2.49×10^9 events were collected, totalling ~ 1.6 Tb of data. Of these, 2.23×10^7 passed the fold 2-2 requirements, with 8.22×10^4 and 6.96×10^4 events passing all gates for 1173 keV and 1332 keV respectively. The significant reduction in efficiency arrises due to the requirement for strip separation to be greater than 10 mm. Due to an error when analysing the data, a small portion of the events were lost, reducing the dataset to 7.00×10^4 and 7.21×10^4 events for 1173 keV and 1332 keV respectively.

Figure 4.6 presents the reconstructed Compton images with and without PSA. All plots have been offset 400 mm in both x and y for display purposes, thus the source is located at $(x_{pos1}, y_{pos1}) = (422, 430)$ mm. One feature present in all images is the cross shape in the intensity profile, with zero intensity around the x = 422, y = 430 mm axis. This is due to a geometric issue with the event selection. With the requirement for greater than 10 mm separation between triggered strips, in addition to the relatively small thickness of the detector, 20 mm, there exists a minimum angle with which an event could be processed. Assuming that each interaction occurred at one of the detector faces with the minimum lateral separation of 10 mm in both x and y, the minimum angle possible is $\sim 35^\circ$, see Figure 4.5. Since the angle of the reconstructed cone is radially symmetric about each axis, the 35° cone angle actually represents a 70° angle when taken as a 2D slice. This feature is also significantly reduced when PSA is applied, as events are focussed into the central hotspot.

Both energies present a strange feature in the original images whereby there exists four hotspots in the reconstruction. The addition of PSA acts to convolve these into one location, significantly improving the resolution of the image. These are once again geometric issues relating to the angular selection imposed by the

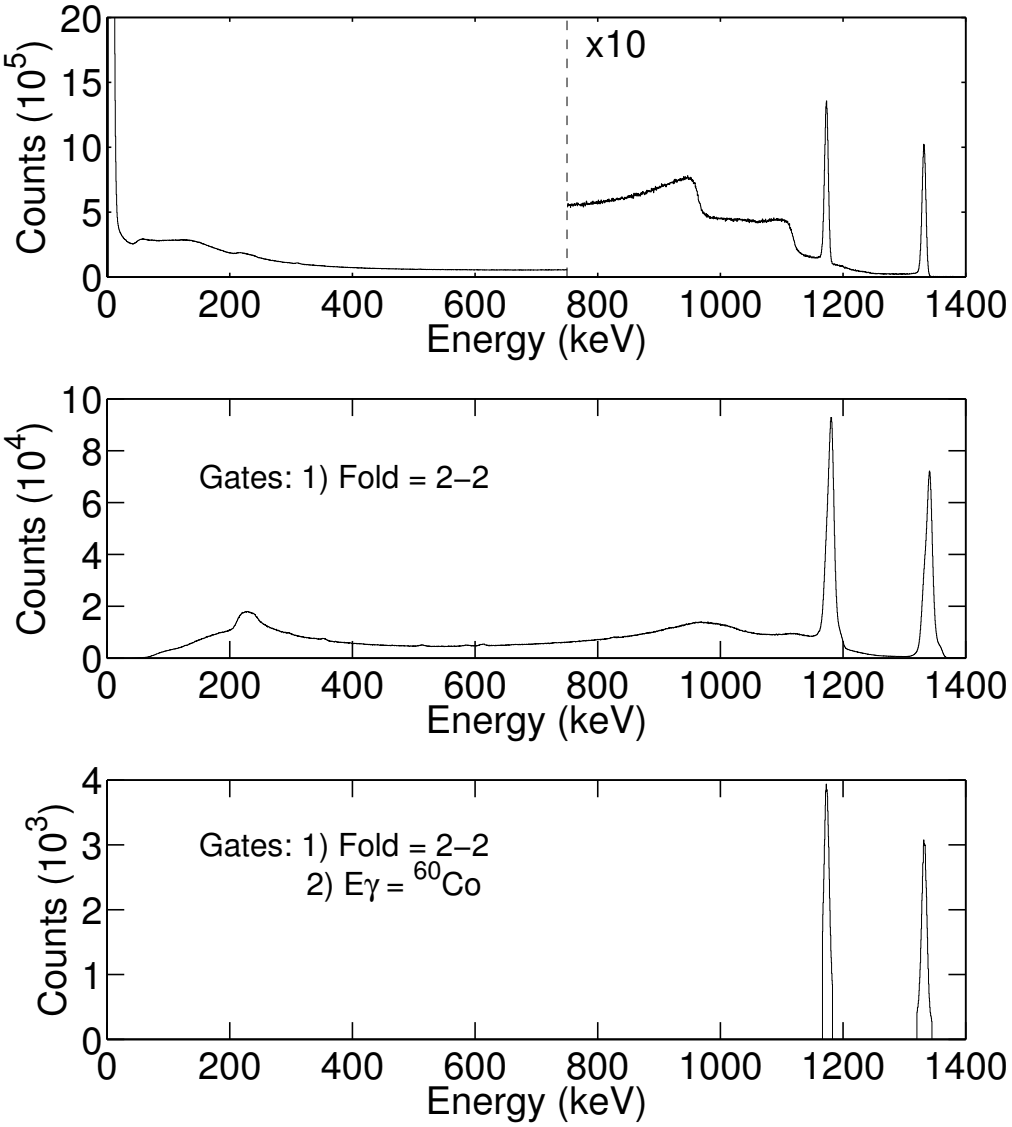

Figure 4.4: Experimental spectra from the R_{38} dataset showing (top) the raw spectra obtained from strip 6 of the DSGSD, displaying the excellent energy resolution of each strip (middle) all fold 2-2 events and (bottom) all fold 2-2 events with strip separation >2 strips whose addback energy is equal to a photopeak energy from ^{60}Co $\pm$ 10 keV

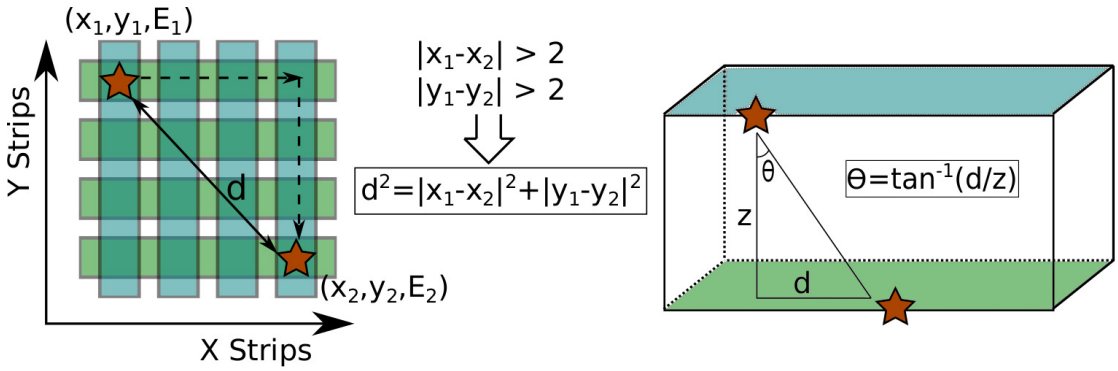

Figure 4.5: Schematic illustrating the minimum possible angle for the event selection utilised in this work

gates and will be explained in more detail with the aid of Monte Carlo simulations in Chapter 5.

For the quantitative analysis, the position resolution was calculated for both x and y along the slice containing the highest intensity pixel for each respective dimension. All reconstructions were projected at a fixed depth, z, of 120 mm, corresponding to the distance from the rear of the detector to the source. An example of the fits used is shown in Figure 4.7, where the reconstructed image is shown in addition to the highest intensity x and y slices. The intensity profile for each slice is fitted using a Lorentzian fit plus a quadratic background fit. From the fitted peak, a Full Width Half Maximum (FWHM) can be calculated, representing the resolution of the reconstructed position. The fit used combines a quadratic background with a Lorentzian peak using,

$$L_x = a + bx + cx^2 + \frac{A}{2\pi}\frac{\Gamma}{(x - x_0)^2 + (\frac{1}{2}\Gamma)^2} \tag{31}$$

where a, b and c represent the constant, linear and quadratic parameters for the background calculation. The peak amplitude is given by A, with x_0 representing the centroid of the distribution x and Γ describing the width of the fit. Each slice is displayed with three different fits; a quadratic background, a purely Lorentzian fit and a combination of the two. In addition, a residual has been calculated for each fit, showing the difference between the Lorentzian fit and the data at each data point. A quadratic fit is used for the background due to the empirical evi-

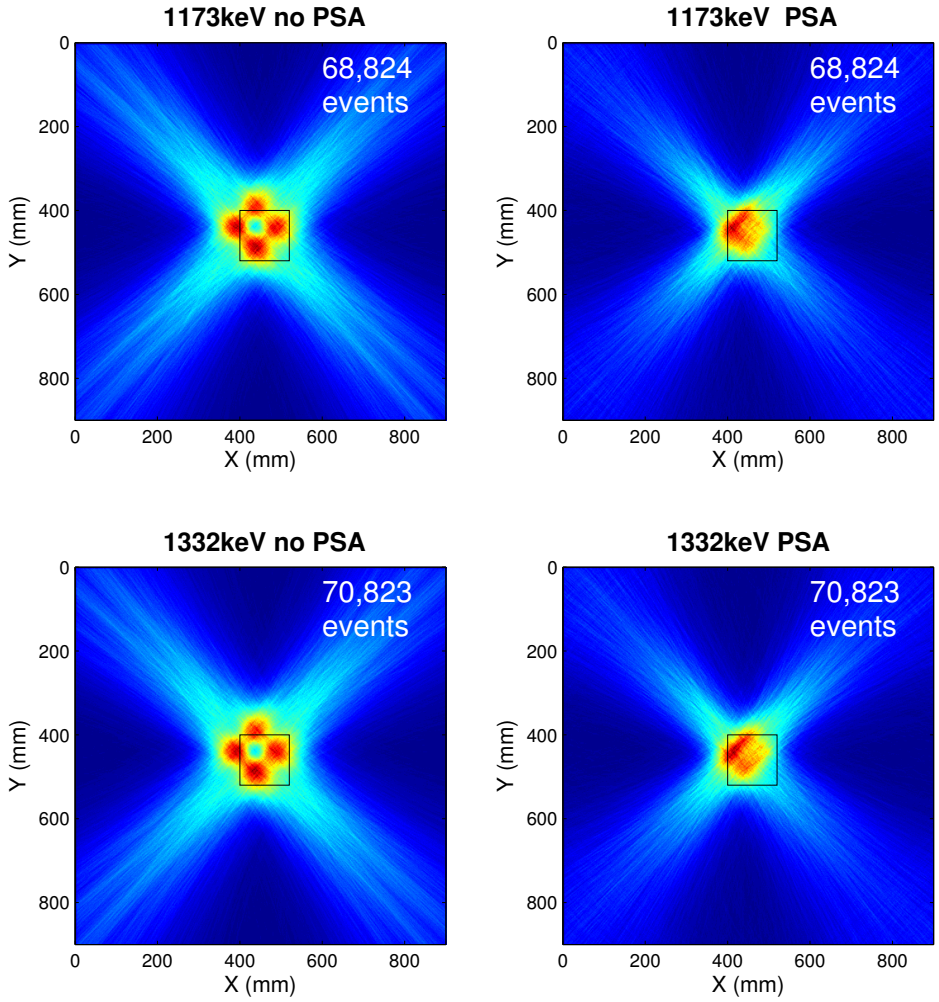

Figure 4.6: Compton image reconstruction for experimental ^{60}Co data showing the effects of PSA on two different energies. The number of events is displayed in the top right of each image, in addition to a box highlighting the position of the detector face

dence supporting this fit. Previous studies involving the use of this reconstruction method have found similar behaviours [7].

Due to the multiple hotspots present in the reconstructions without PSA, fitting a single Lorentzian produced a fit with a large χ^2, the centroid of which was located between the two peaks. For this reason, it is non-physical to apply such a fit to the data and extract any meaningful conclusions. However, the convolution effect observed with the application of PSA drastically improves the χ^2 of the fit, thus improving the reliability of any results extracted. The results for the 1173 and 1332 keV reconstructions are presented in Figures 4.7 and 4.8 respectively.

For both the 1173 and 1332 keV γ-decays, we can conclude that it is not possible to perform Compton imaging in this scenario without the use of PSA due to the multiple hotspots reconstructed from a single source. Through the application of PSA, the position resolution for 1173 keV, Figure 4.7, is calculated to be $FWHM_x = 128$ mm and $FWHM_y = 123$ mm, with the centroid located at $(x, y) = (448, 434)$ mm. In addition, for 1332 keV, Figure 4.8, the position resolution is calculated as $FWHM_x = 125$ mm and $FWHM_y = 128$ mm, with the centroid located at $(x, y) = (447, 437)$ mm. In terms of the position reconstruction, the data provides a good estimation of the source location. The source location is known to be at $(x_{pos1}, y_{pos1}) = (422, 430)$ mm, with the 1173 keV data deviating by 26 mm in x and 4 mm in y, and the 1332 keV data deviating by 25 mm in x and 7 mm in y. These values are well within the confines of the position resolution stated above.

4.4 Europium 152 Results

Images were generated using both the R_{30} and R_{32} ^{152}Eu datasets, located in pos 1 and 2 respectively (see Figure 4.1), with Figure 4.9 showing the γ spectrum for varying stages of the sort process. For both runs, a ^{152}Eu source with an activity of 64 kBq was used, with count rates of $\sim$ 5,500 and 6,800 cps for the R_{30} and R_{32} respectively. The count rate was higher for the run with the source positioned centrally, due to the larger solid angle coverage. After the initial analysis, it was

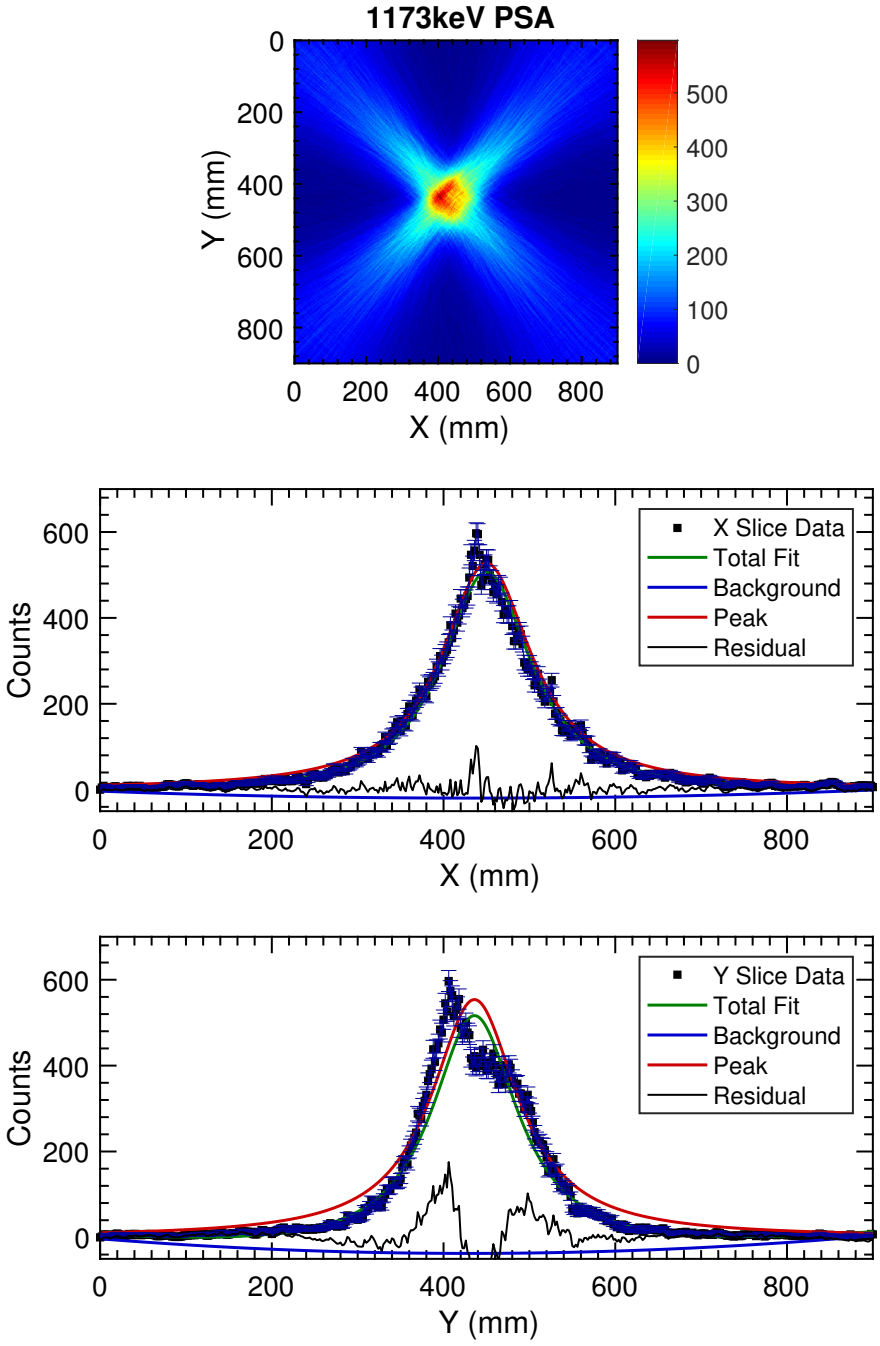

Figure 4.7: Compton image reconstruction using the 1173 keV γ-ray from ^{60}Co, showing reconstructed image in addition to a Gaussian fit applied to the X and Y slice with peak intensity. Results shown with the addition of PSA

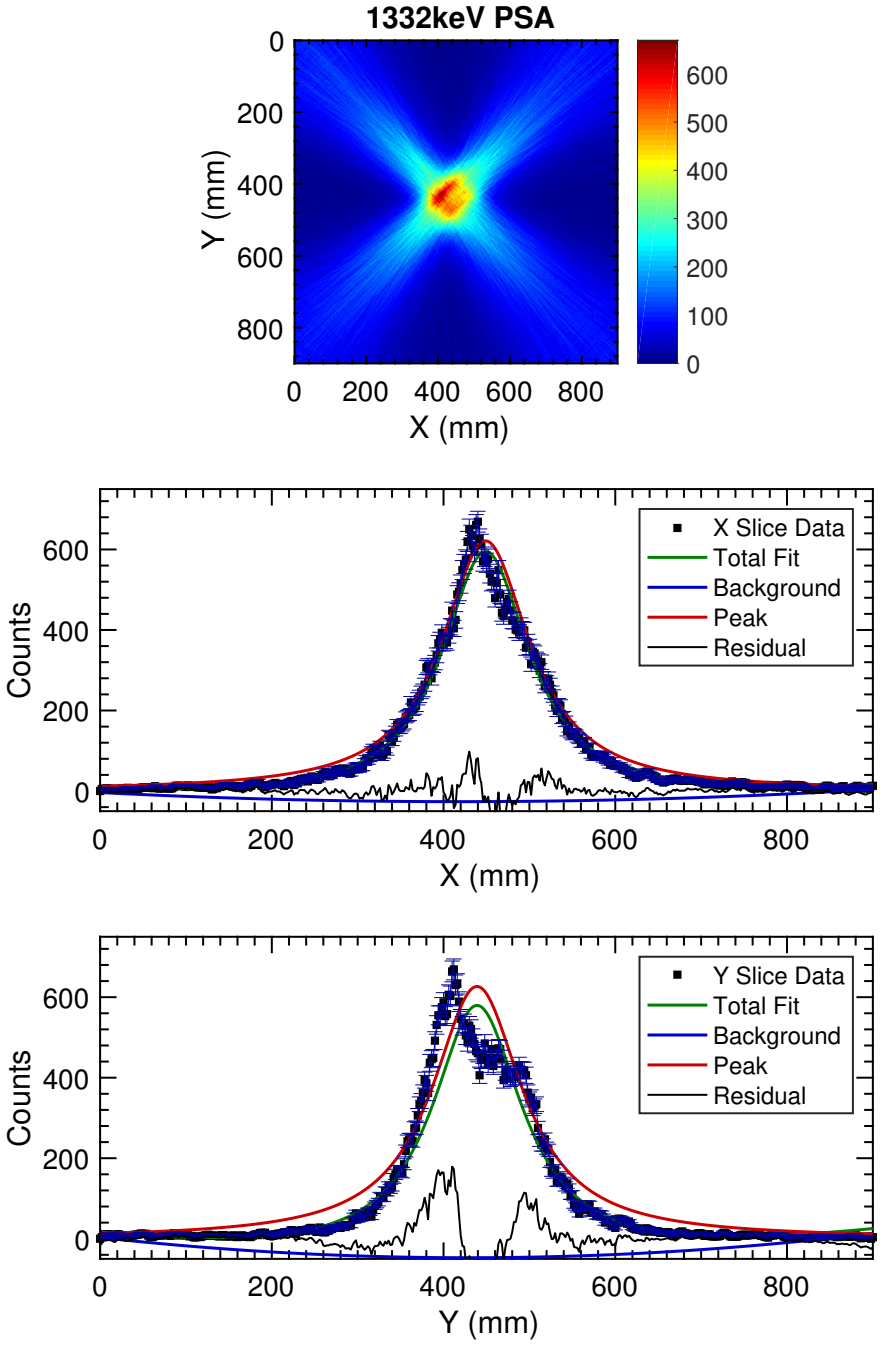

Figure 4.8: Compton image reconstruction using the 1332 keV γ-ray from ^{60}Co, showing reconstructed image in addition to a Gaussian fit applied to the X and Y slice with peak intensity. Results shown with the addition of PSA

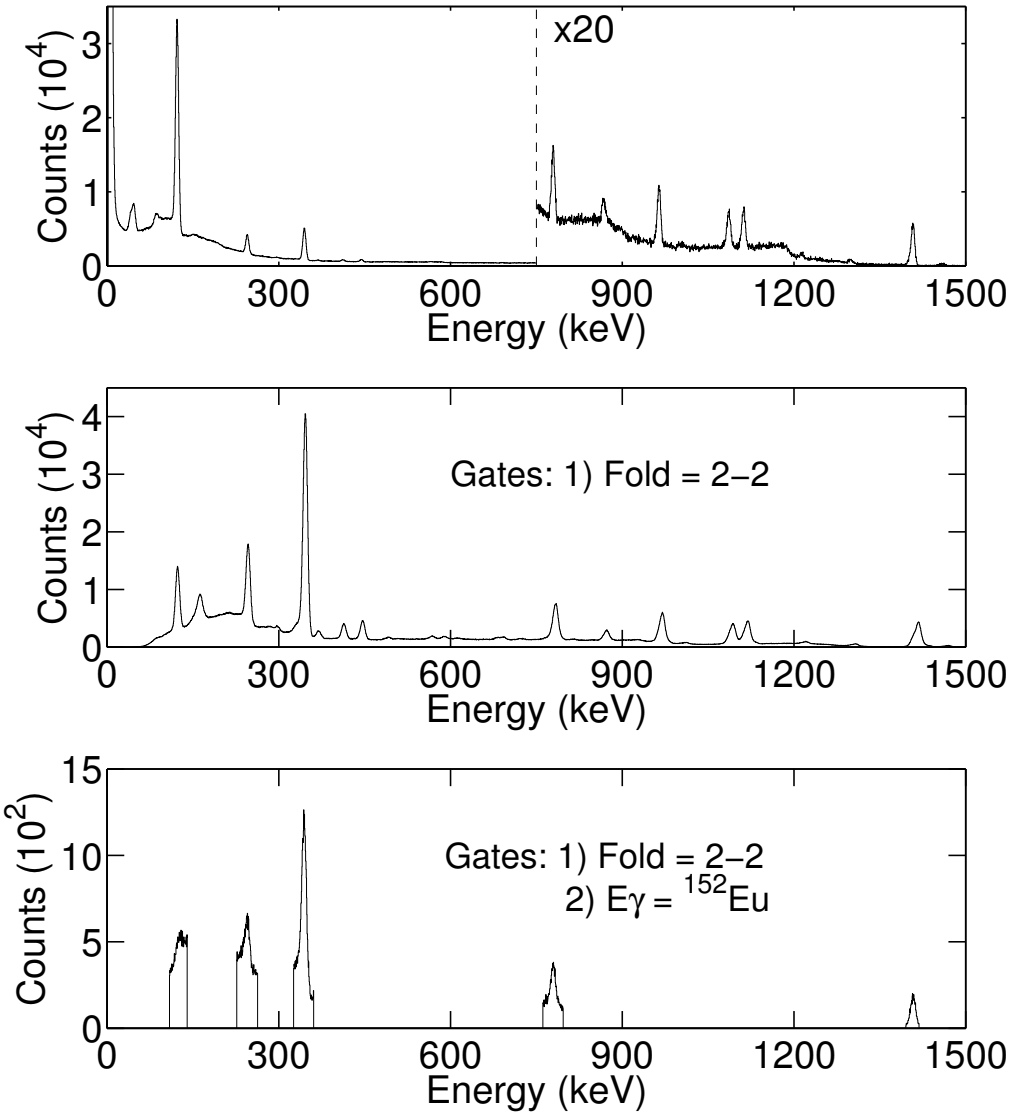

Figure 4.9: Experimental spectra from the R_{30} dataset showing (top) the raw spectra obtained from strip 6 of the DSGSD (middle) all fold 2-2 events and (bottom) all fold 2-2 with strip separation $>$ 2 strips events whose addback energy is equal to a photopeak energy from ^{152}Eu $\pm$ 10 keV

decided that all analysis of ^{152}Eu would only be performed using the larger R_{32} dataset, due to the limited statistics available from the R_{30} dataset. From the R_{32} experimental run 8.06×10^8 events were collected, totalling 650.6 Gb of data. Of these, 6.47×10^6 passed the fold 2-2 requirements with 2.83×10^4, 3.25×10^4, 3.83×10^4, 1.46×10^4 and 4.36×10^3 events passing all gates for 121, 244, 334, 778 and 1408 keV respectively.

Figure 4.10 presents the reconstructed Compton images for the 121, 244 and 344 keV γ-rays with and without PSA. Figure 4.11 presents the reconstructed Compton images for the 778 and 1408 keV γ-rays with and without PSA. As before, all images have been offset 400 mm in x and y with the source located at $(x_{pos2}, y_{pos2}) = (452, 430)$ mm. The images generated without the application of PSA exhibit the same features discussed earlier in Section 4.3, with four central hotspots surrounded by a cross shaped background. These are geometric effects caused by the angular selection placed upon events, a more detailed explanation of which will be provided in Section 5. The results with PSA are similar to the ^{60}Co results, with the four central hotspots convolving into one. With a much larger range of initial γ-ray energies, we can see that the central hotspot is much more compact with increasing γ-ray energy, in addition to moving closer to the known location of the source for higher energy decays.

For the two lowest energy decays, the 121 and 244 keV γ-rays, the effects of PSA are limited. Although the image convolves into a single hotspot, the spread of that hotspot is very broad, resulting in very large position resolutions. For the 121 keV decay, Figure 4.12, the resolutions were calculated to be $FWHM_x = 315$ mm and $FWHM_y = 190$ mm, with the centroid located at $(x, y) = (455, 337)$ mm. For the 244 keV decay, Figure 4.13, the resolutions were calculated to be $FWHM_x = 283$ mm and $FWHM_y = 210$ mm, with the centroid located at $(x, y) = (458, 418)$ mm. This dataset was taken with the source located in pos 2, with $(x, y) = (452, 430)$ mm, the 121 keV dataset differs from this by 3 mm in x and 93 mm in y, with the 244 keV results deviating by 6 mm in x and 12 mm in y. The results for the 121 keV decay are significantly different from

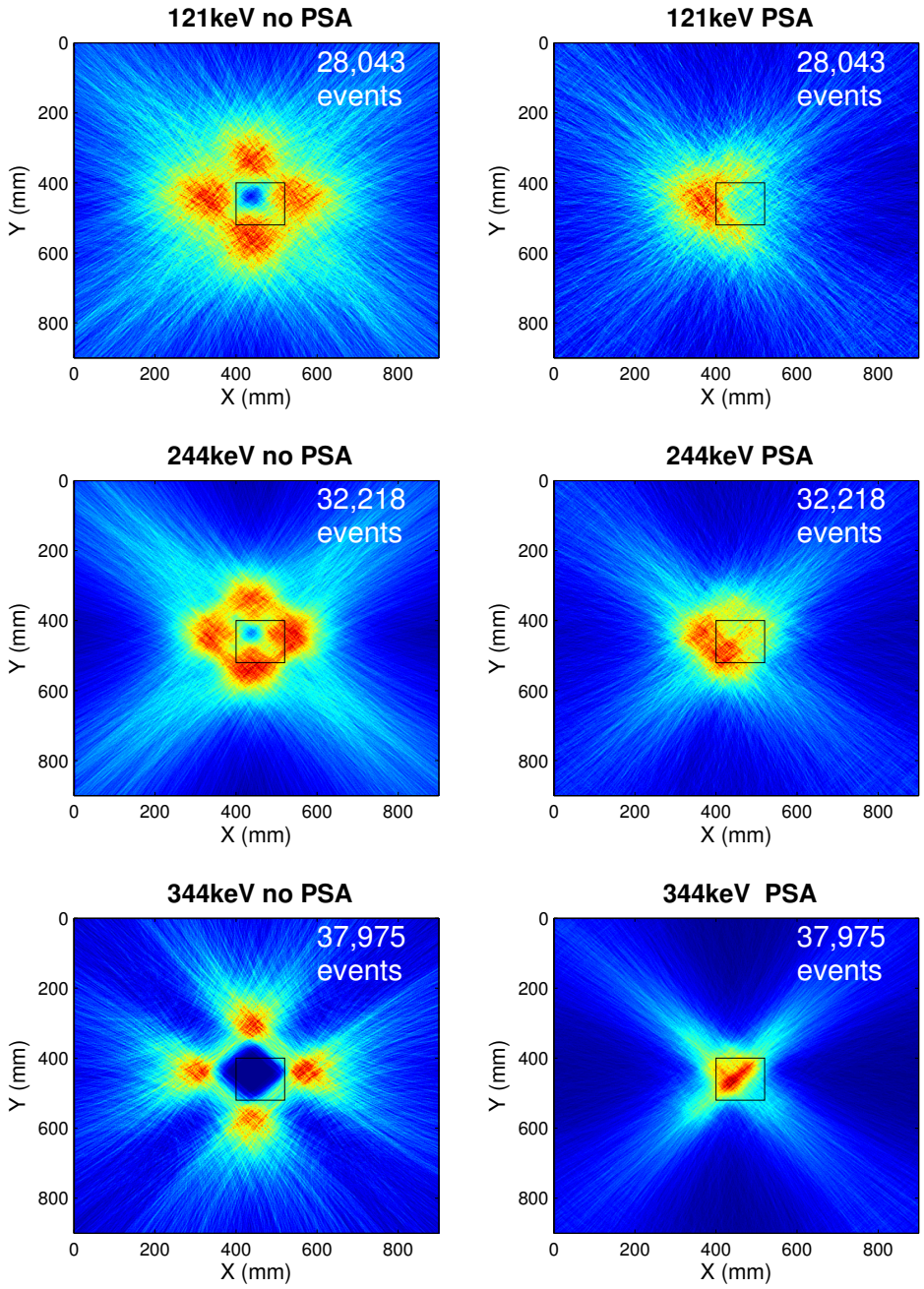

Figure 4.10: Compton image reconstruction for experimental ^{152}Eu data showing the effects of PSA on three different energies. The number of events is displayed in the top right of each image, in addition to a box highlighting the position of the detector face

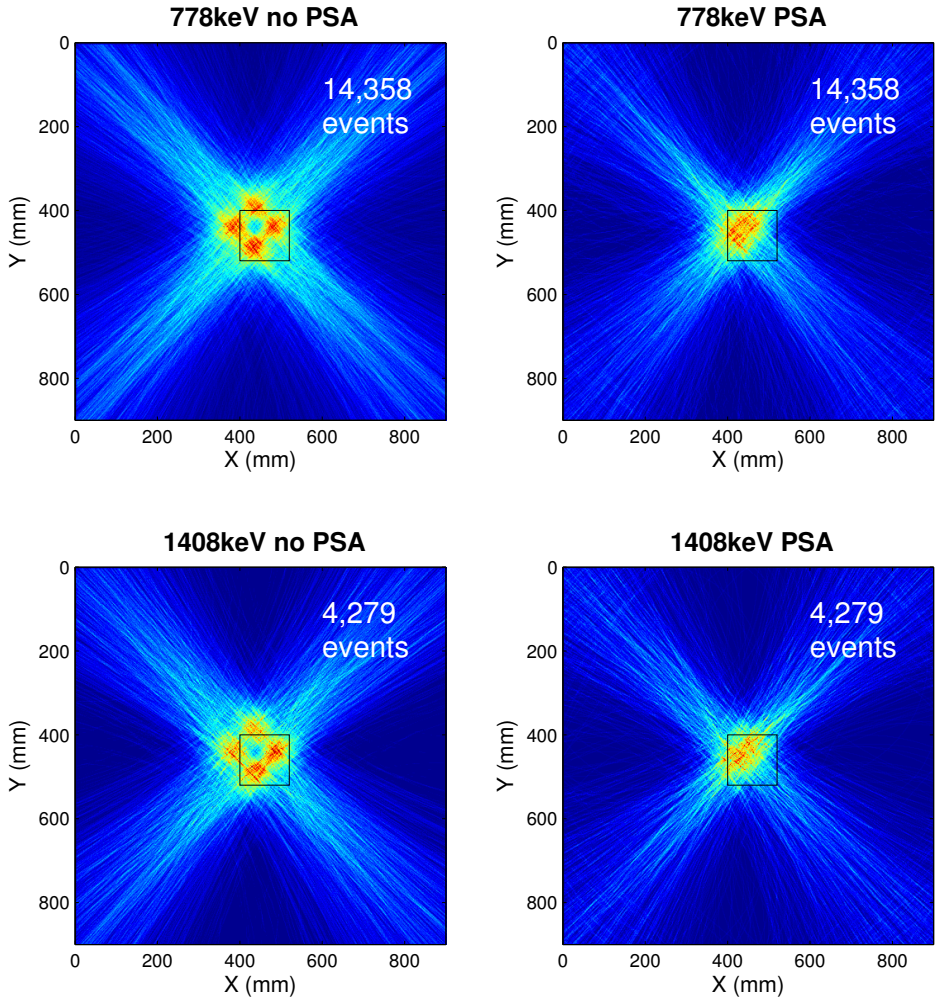

Figure 4.11: Compton image reconstruction for experimental ^{152}Eu data showing the effects of PSA on two different energies. The number of events is displayed in the top right of each image, in addition to a box highlighting the position of the detector face

the expectation, casting doubt on the capability of imaging at this energy within the constraints of the current setup. In contrast, the 244 keV decay provides an excellent reconstruction of the source position, however the position resolution of the reconstruction is much worse than that of the higher energy images. Imaging at these low energies is extremely challenging due to the much reduced signal-to-noise ratio for small energy deposits, especially when looking at image charges. This, combined with the short mean free path for low energy photons means a reduction in both the quality of data and also the volume.

For the 344 keV γ-ray, Figure 4.14, the resolutions with PSA were calculated to be $FWHM_x = 134$ mm and $FWHM_y = 118$ mm, with the centroid located at $(x, y) = (449, 436)$ mm. The position resolution represents a significant improvement from the 244 keV measurements to the 344 keV measurements, with the source location deviating from the known position by 3 mm in x and 6 mm in y. The resolution with PSA for the 778 keV γ-ray, Figure 4.15, were calculated to be $FWHM_x = 126$ mm and $FWHM_y = 125$ mm, with the centroid located at $(x, y) = (444, 428)$ mm. The source location differs from the known position by 8 mm in x and 2 mm in y. For the 1408 keV γ-ray, Figure 4.16, the resolutions with PSA were calculated to be $FWHM_x = 126$ mm and $FWHM_y = 114$ mm, with the centroid located at $(x, y) = (448, 433)$ mm. The source location deviates from the known position by 4 mm in x and 3 mm in y. All three of these energies excellently reproduce the source location, in addition to providing a significantly improved position resolution when compared to the 121 and 244 keV measurements. All results for ^{60}Co and ^{152}Eu are summarised in Table 4.6.

With the energy resolution only varying by a small amount from 121 - 1408 keV, the effects displayed between the 121 keV and the 1408 keV reconstructions can be attributed to the improved position sensitivity at higher energy. With larger signals, the signal-to-noise ratio for both real and transient charges increases, which in turn improves the effectiveness of the PSA grid search algorithm. At 121 keV, most of the image charges are barely above the background noise in the detector, thus removing the ability to distinguish between pulses from positions

Table 4.6: Summary of the Compton imaging results presented for all seven energies studied

E_γ (keV)	Δx (mm)	Δy (mm)	x, y (mm)	$\Delta x, y$ (mm)
121	315	190	$(455, 337)$	$(+3, -93)$
244	283	210	$(458, 418)$	$(+6, -12)$
344	134	118	$(449, 436)$	$(-3, +6)$
778	126	125	$(444, 428)$	$(-8, -2)$
1173	128	123	$(448, 434)$	$(+26, +4)$
1332	125	128	$(447, 437)$	$(+25, +7)$
1408	126	114	$(448, 433)$	$(-4, +3)$

varying in x and y. Additionally, the z PSA information is also reduced for small energy deposits due to the real charge pulses being significantly affected by noise. As the γ-ray energy increases, all of these effects are reduced, thus improving the effectiveness of the PSA algorithms. These effects can be seen in the ^{152}Eu reconstructions, Figures 4.12 - 4.16, in addition to the ^{60}Co images, Figures 4.7 and 4.8

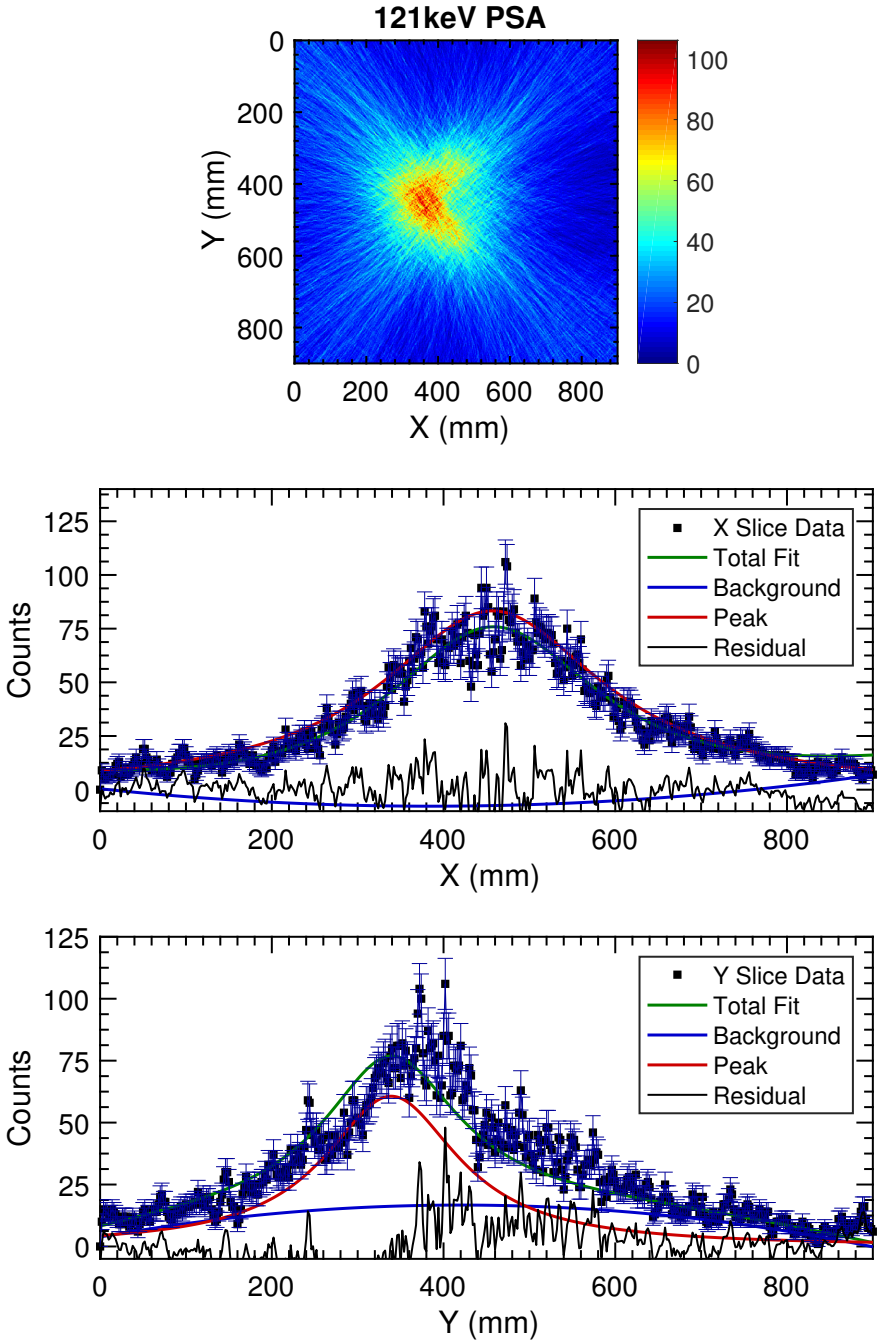

Figure 4.12: Compton image reconstruction using the 121 keV γ-ray from ^{152}Eu, showing reconstructed image in addition to a Gaussian fit applied to the X and Y slice with peak intensity. Results shown with the addition of PSA

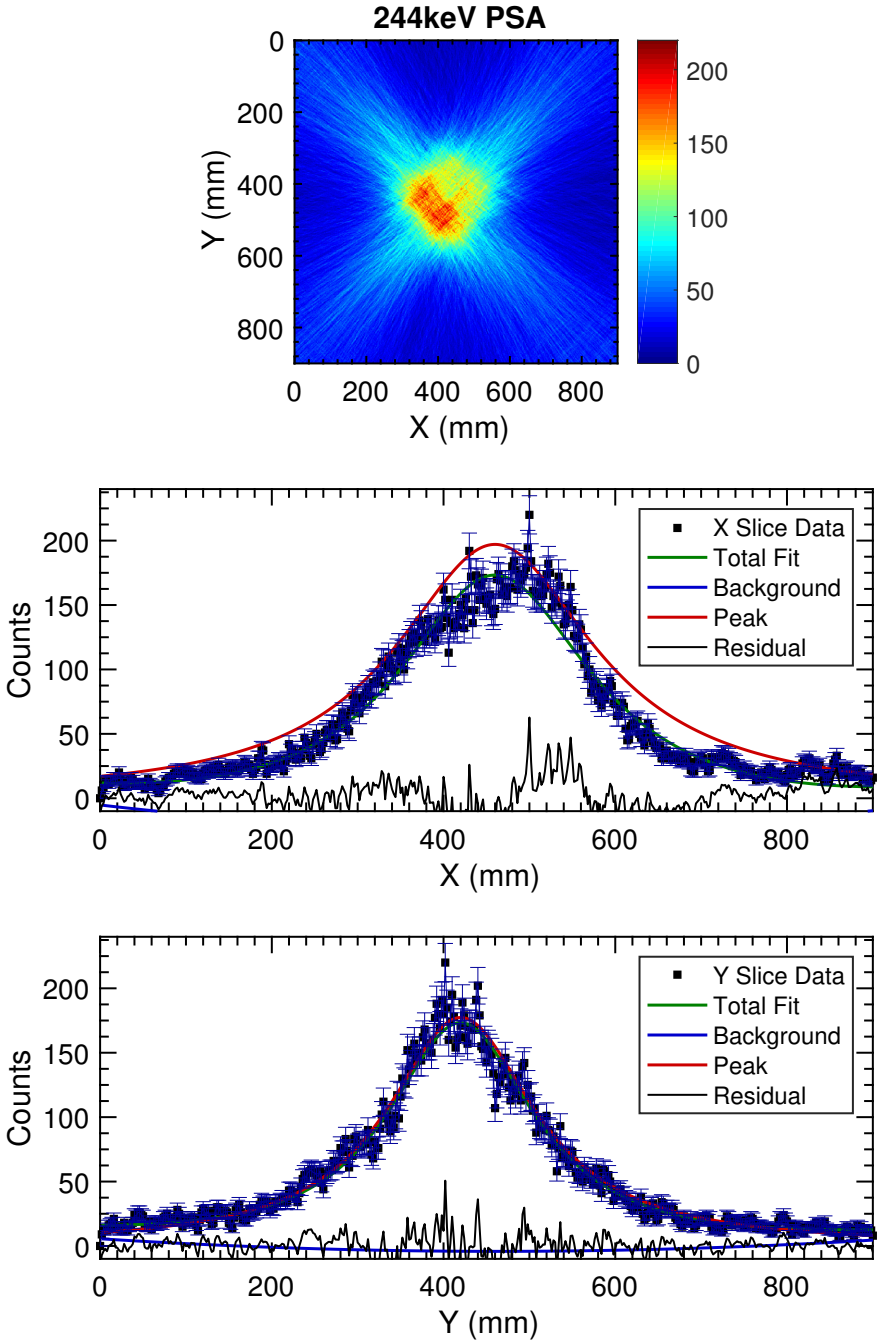

Figure 4.13: Compton image reconstruction using the 244 keV γ-ray from ^{152}Eu, showing reconstructed image in addition to a Gaussian fit applied to the X and Y slice with peak intensity. Results shown with the addition of PSA

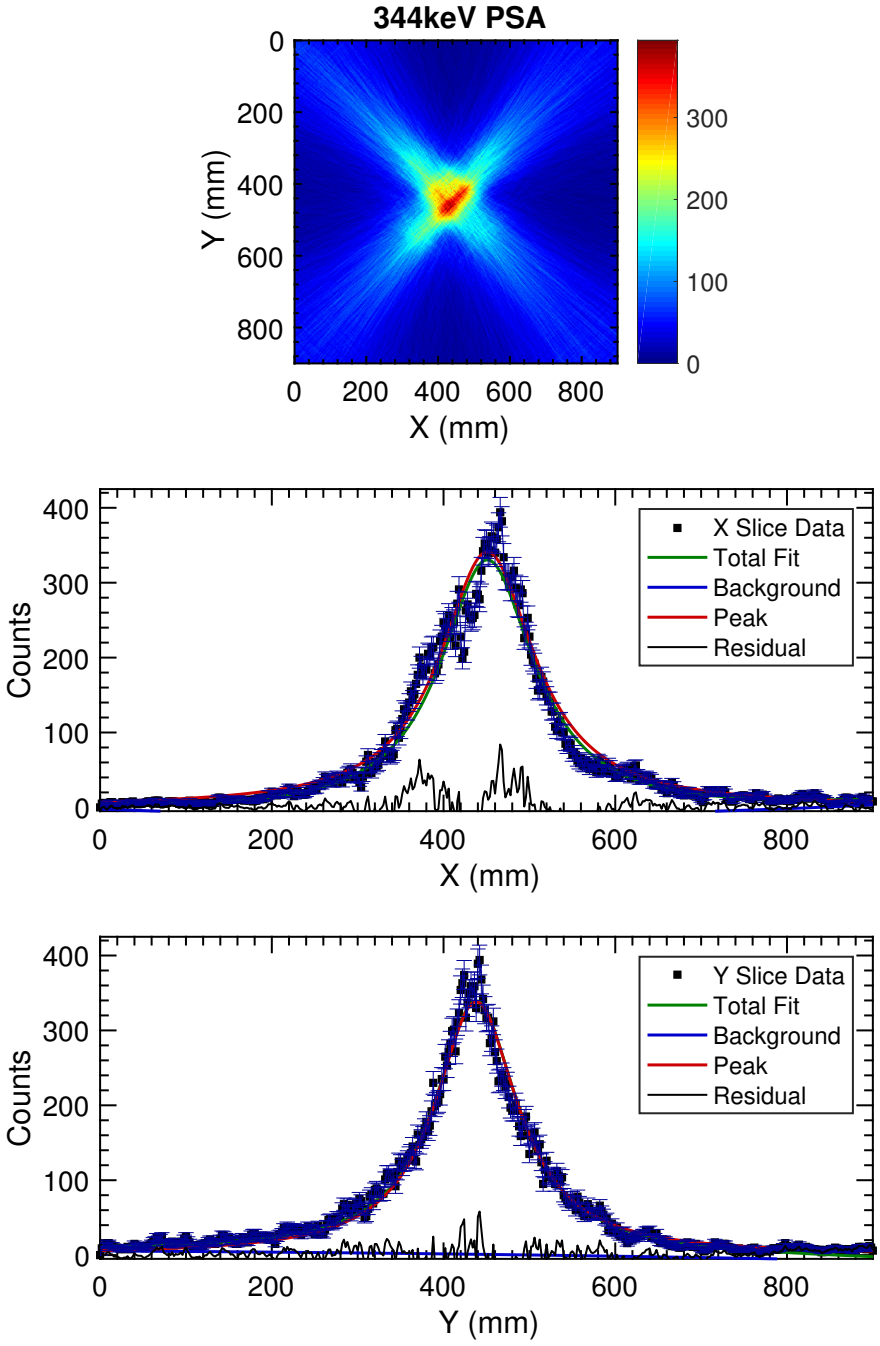

Figure 4.14: Compton image reconstruction using the 344 keV γ-ray from ^{152}Eu, showing reconstructed image in addition to a Gaussian fit applied to the X and Y slice with peak intensity. Results shown with the addition of PSA

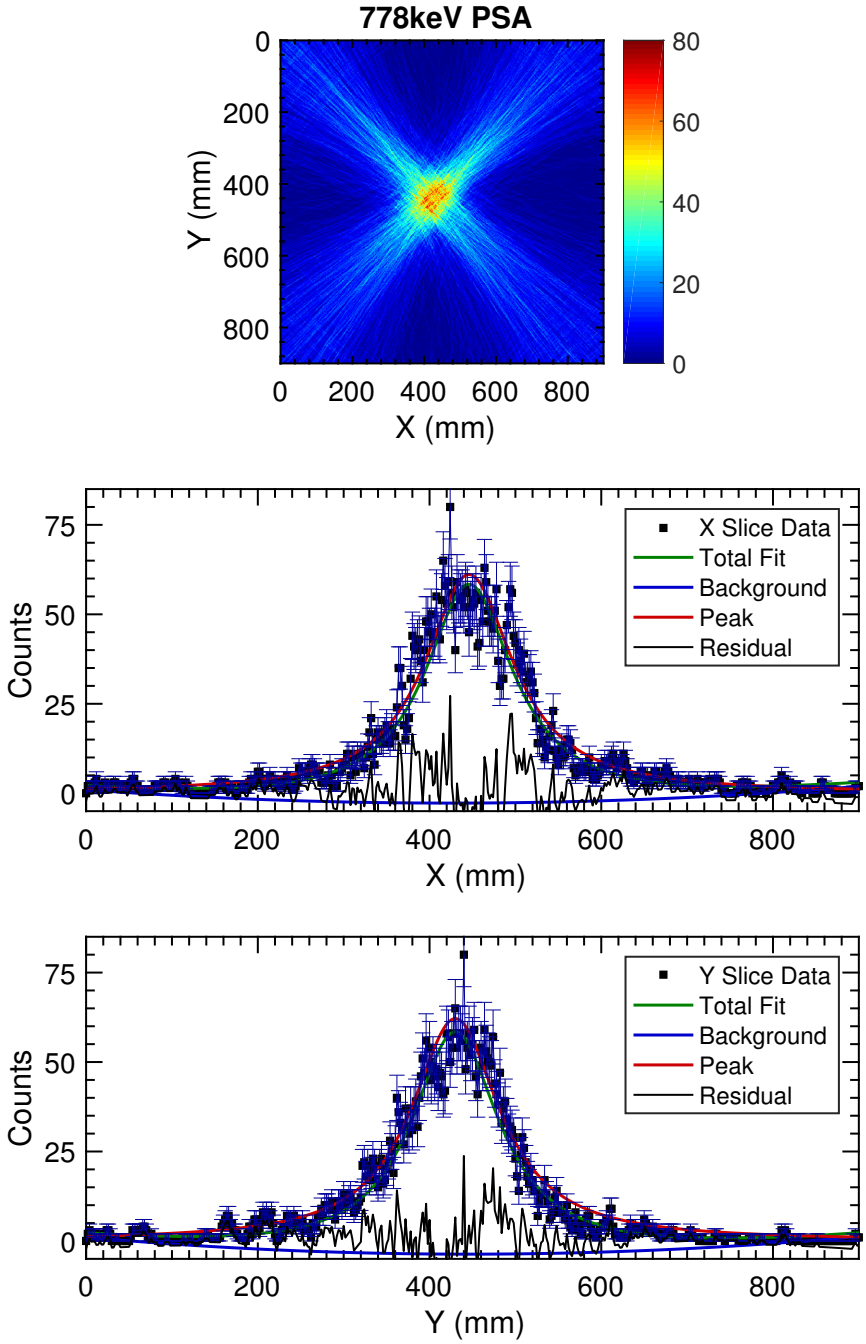

Figure 4.15: Compton image reconstruction using the 778 keV γ-ray from ^{152}Eu, showing reconstructed image in addition to a Gaussian fit applied to the X and Y slice with peak intensity. Results shown with the addition of PSA

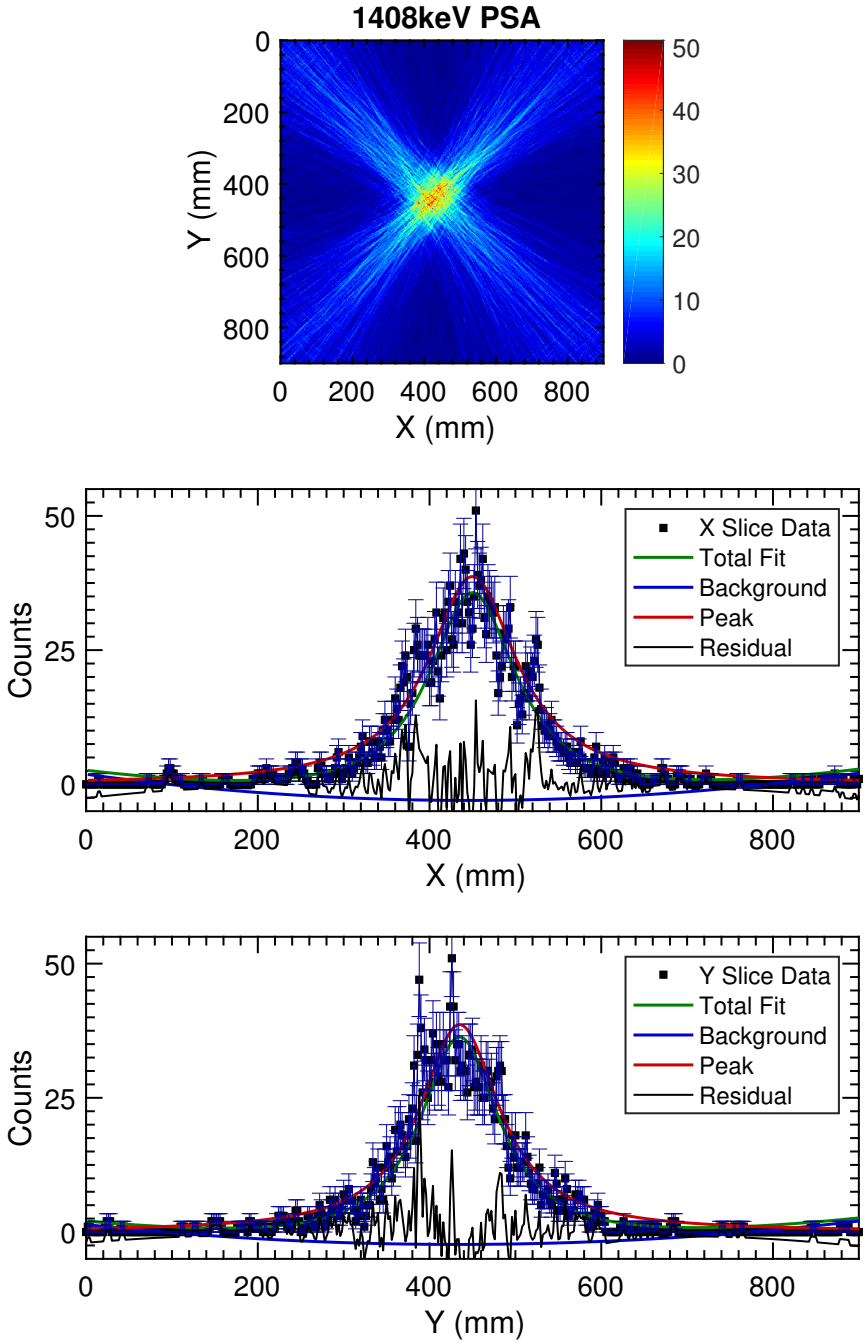

Figure 4.16: Compton image reconstruction using the 1408 keV γ-ray from ^{152}Eu, showing reconstructed image in addition to a Gaussian fit applied to the X and Y slice with peak intensity. Results shown with the addition of PSA

5 Gamos Simulations

5.1 Geometric Effects in Imaging

In addition to the experimental measurements, simulations for the expected performance of the detector were performed using the GAMOS, GEANT4-based Architecture for Medicine-Oriented Simulations [33], simulation package. As the name suggests, GAMOS is a scripting language based upon the Monte Carlo code, GEANT4 [34, 35]. GAMOS enables users to perform complex simulations using a simplified interface, removing the need to programme in C++, as is the case for GEANT4.

To simulate the effects of PSA, detector models were created with different voxel sizes to represent the experimental position resolution of the detector. Hit coordinates were taken to be in the centre of each voxel, much in the same way as the experimental results without PSA. Schematics of each model are displayed in Figure 5.1. The first detector model created for the simulation without PSA consisted of a $60\times60\times10$ mm^3 Ge scatter detector located 100 mm from the source, with a $60 \times 60 \times 10$ mm^3 Ge absorber detector immediately behind. Each detector was segmented into 144 voxels ($12 \times 12 \times 1$) with a voxel size of $5 \times 5 \times 10$ mm^3. The second model created to simulate the effects of PSA was based upon the first model, however the segmentation was much finer. The $12 \times 12 \times 1$ segmentation utilised in the first model was replaced by a $60\times60\times10$ segmentation, representing the 1 mm position resolution with which the pulse shape database was created. The improvement in position resolution should significantly reduce the angular error when calculating the cone axis, resulting in an improved FWHM for the reconstructed image. The main purpose of the simulation was to prove that the features present in the experimental images are physical, in addition to helping explain the origins of these features.

Simulations were performed using a γ-ray energy of 778 keV, which was chosen due to the increased efficiency of germanium at this energy. The results of these are presented in Figure 5.2 for both models, with a more quantitative analysis

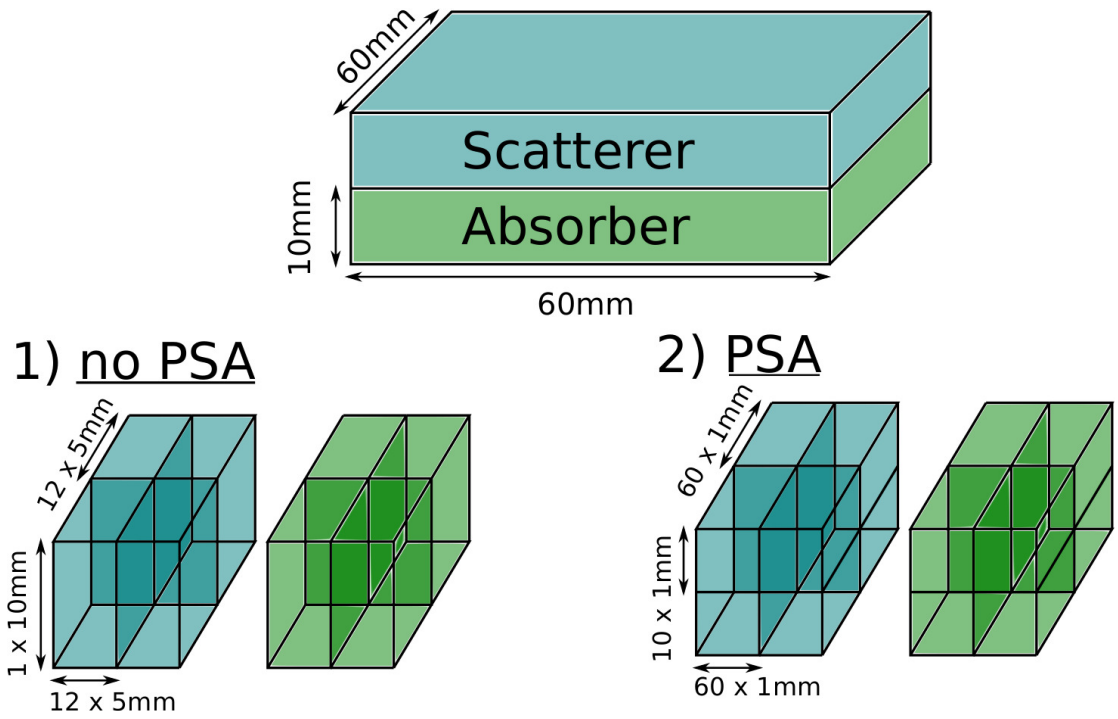

Figure 5.1: Schematics of the two different geometries simulated using Gamos. Both models are based upon the top diagram, with the differentiation coming from the size of each voxel, depicted below. The first model represents raw positional information available from the segmentation of the detector, with the second model simulating the effects of using a 1 mm basis for PSA

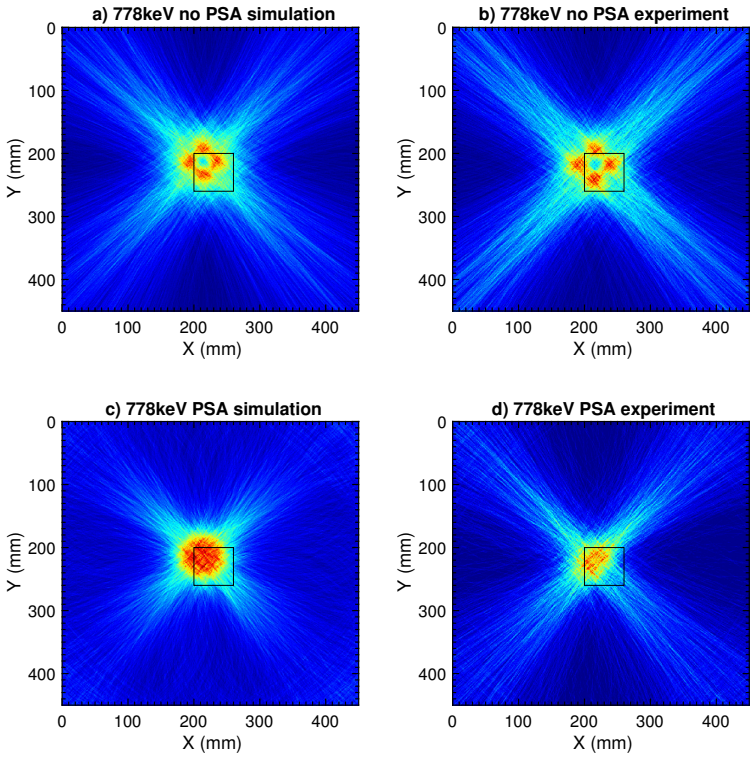

Figure 5.2: Compton image reconstruction for simulated and experimental ^{152}Eu data showing data from a 778 keV γ energy with and without PSA

presented for the PSA model in Figure 5.3. A qualitative comparison between simulated date, Figure 5.2, and experimental data, Figure 4.11, shows the presence of the same four hotspots in addition to the four distinct spikes protruding uniformly outwards from the centre. This suggests that these features are physical and not the effects of an error in the imaging process. The same is true of the PSA results, with Figures 5.3 (simulated) and 4.15 (experimental) also displaying similar features. The four hotspots present in the raw images appear to converge into one central region with the outward projecting spikes still present. From the fits applied to the data, position resolutions were calculated to be $FWHM_x = 134$ mm and $FWHM_y = 125$ mm, with the centroid located at $(x, y) = (439, 425)$ mm, providing excellent agreement with the values obtained experimentally.

In addition to validating the experimental results, the simulations enable predictions to be made and certain features of the process to be explored in more

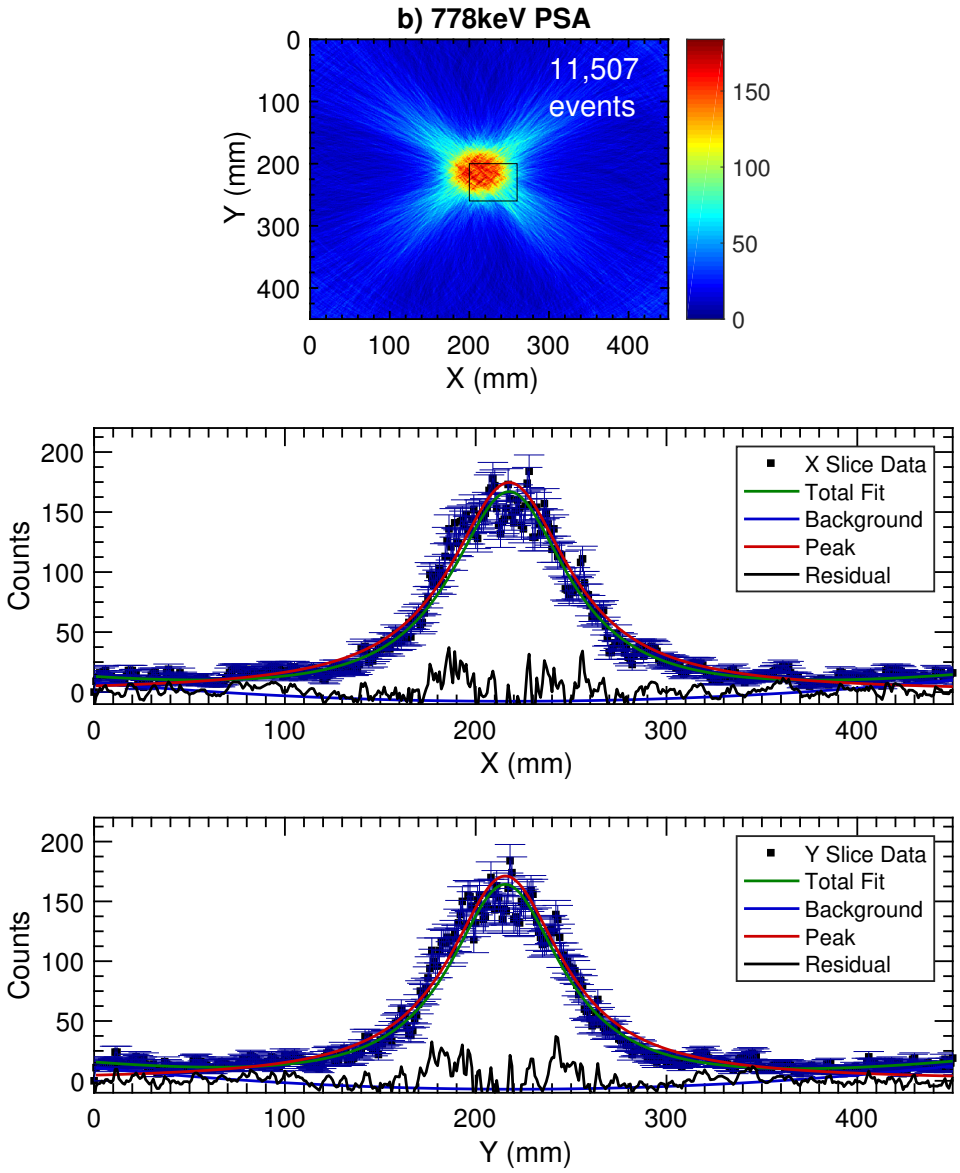

Figure 5.3: Compton image reconstruction for simulated ^{152}Eu data showing the effects of PSA when using a 778 keV γ energy

depth. One example of this is the four hotspots present in the 'noPSA' results. These are attributed to the restrictions imposed upon the cone opening angle by the selection criteria utilised, with the angle between two interactions, independent of energy, provided by Eqn 29. For the initial measurements, the depth of each interaction was taken to be constant, with $z_1 = 9$ mm and $z_2 = 11$ mm. For two interactions within the same detector with $\Delta z = 2$ mm, the angular range is

$$81.95^\circ \leq \theta \leq 88.65^\circ \quad \& \quad 91.35^\circ \leq \theta \leq 98.05^\circ \tag{32}$$

with the second range representing the two depths being switched. Using the same simulation as earlier, gates were applied to only image interactions within a set angular range. The results of this are presented for four ranges in Figure 5.4. From this, it can be seen that for values of θ which fall between the allowed range, the four hotspot convolve into one central spot, with θ values outside of the allowed range maintaining the original shape.

Further to this, the data were imaged with the assumption that each interaction occurred at one of the detector faces, such that $\Delta z = 20$ mm. With this new set of conditions in place, the angular ranges becomes

$$35.26^\circ \leq \theta \leq 76.74^\circ \quad \& \quad 103.26^\circ \leq \theta \leq 144.74^\circ \tag{33}$$

with the resulting images displayed in Figure 5.5. The $35.26^\circ \leq \theta \leq 76.74^\circ$ range was not imaged due to limited statistics. Figure 5.5 shows similar behaviour to Figure 5.4, with a clear improving in the clarity of the image for events within the accepted angular range.

These erroneous events arise due to the reconstruction algorithms used, with the cone angle only being dependent on the energy depositions and not the hit coordinates. The reconstruction code calculates the cone axis from the two sets of hit coordinates and then projects a cone onto that axis with an opening angle calculated using Eqn 21. This leads to issues when the depth of the interaction is so poorly understood, as is the case for the results without PSA. The depth of interaction can be interpreted by the algorithm as either shallower or deeper for

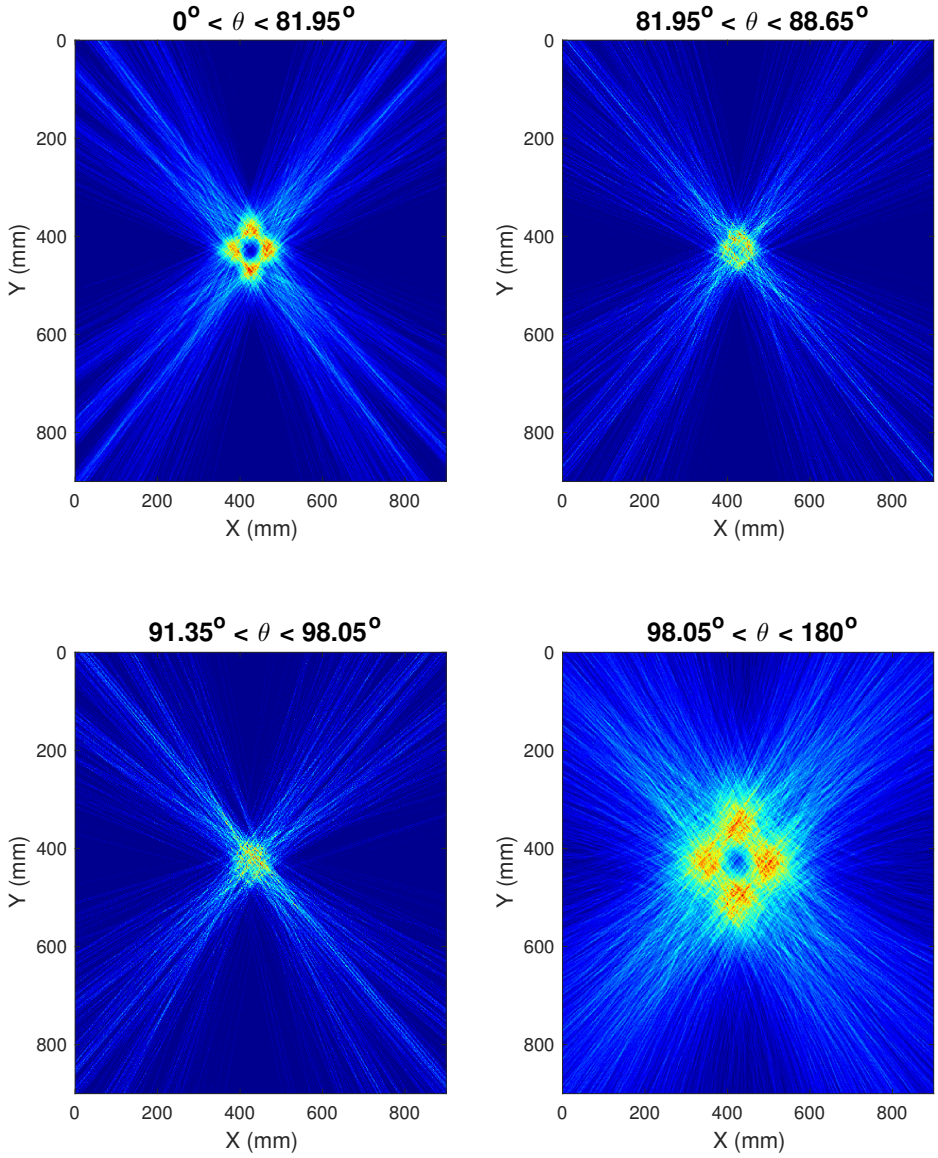

Figure 5.4: Compton image reconstruction for a simulated γ-ray energy of 778 keV, showing the effects of altering the acceptance angle on the resultant image for a depth separation of 2 mm

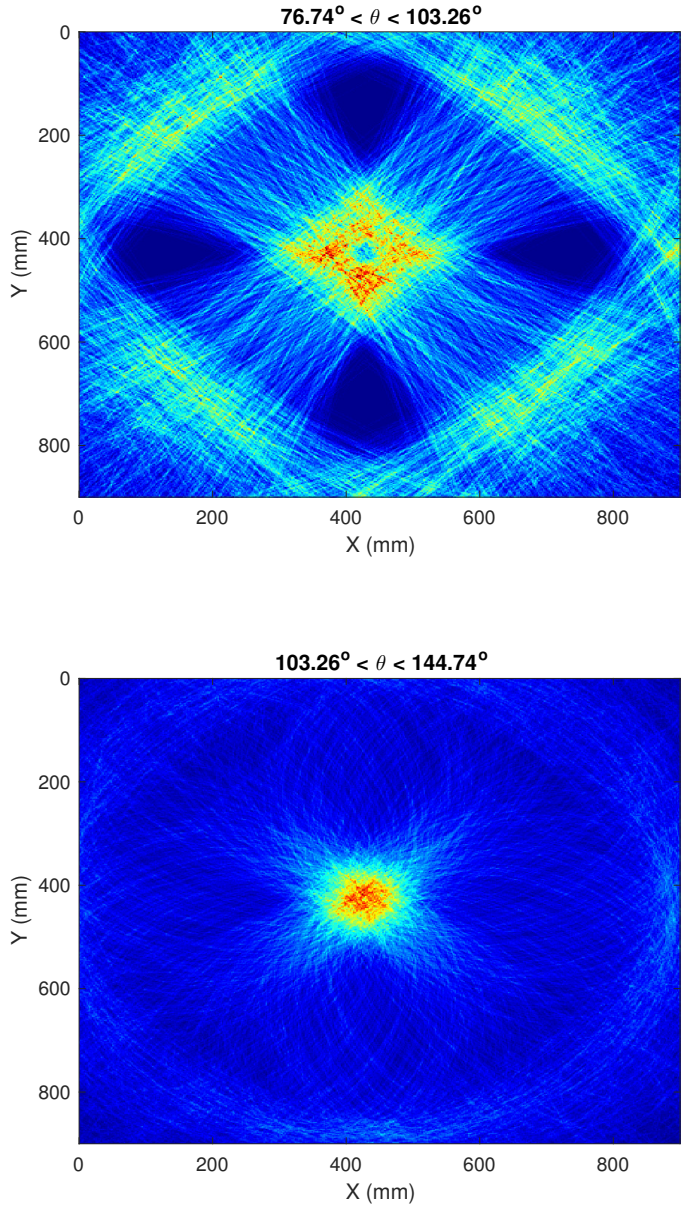

Figure 5.5: Compton image reconstruction for a simulated γ-ray energy of 778 keV, showing the effects of altering the acceptance angle on the resultant image for a depth separation of 20 mm

both the scatterer and the absorber, presenting four distinct combinations. It is these four combinations that lead to the four hotspots in the reconstructed images.

5.2 Efffects of Energy and Postion Resolution on Imaging

Although simulations prove useful in explaining experimentally observed features, they also provide an excellent opportunity to calculate the expected outcome of untested scenarios. This enables us to study the effects of changing one parameter whilst keeping the other the same and gain a deeper understanding of the individual contributions of each detector characteristic. For the results of these simulations to be deemed credible, they must first be validated against a known result. This validation comes from the work discussed earlier in this section.

When reconstructing Compton images, there are two main parameters of interest; energy resolution and position resolution. A detector with better energy resolution will more accurately and more consistently determine the energy of deposits within the crystal, which in turn produces a more accurate cone angle. The second parameter affects the axis of the reconstruction, and is governed by the positions of the interactions within the detector. A detector with better position resolution will be able to locate interactions on a finer grid and thus will be able to make finer adjustments to the reconstruction axis.

To study the contributions of each of these parameters, two sets of simulations were performed; firstly a set of three simulations were ran with a constant position resolution and varying energy resolutions of 0 keV, 3 keV and 50 keV. These values were chosen to represent a perfect detector (0 keV), a realistic semiconductor (3 keV), and finally a typical scintillator (50 keV). The second set of simulations maintained a constant energy resolution whilst altering the position resolution. This was done in the same way as discussed earlier for the PSA comparison, see Figure 5.1, with voxel sizes of 1 mm^3, 2 mm^3 and 5 mm^3 studied. For all simulations, energy resolution refers to the FHWM of the energy peak, where FWHM = 2.35σ, with position resolution referring to the volume of the voxels used.

Table 5.1: Summary of Compton image reconstruction results for energy resolution simulations for an initial γ-ray energy of 778 keV

ΔE (keV)	Δx (mm)	Δy (mm)	x,y (mm)	Δx,y (mm)
0	93	73	(428,431)	(-2, +1)
3	99	65	(429,430)	(-1, 0)
50	93	54	(429, 430)	(-1, 0)

5.2.1 Energy Resolution

Each simulation was ran using a γ-ray energy of 778 keV with a detector geometry similar to that depicted in Figure 5.1. This consisted of two planar detectors stacked one behind the other, each measuring $60 \times 60 \times 10$ mm with a voxel size of $2 \times 2 \times 10$ mm^3. A total of 35,000 events were simulated for each energy resolution, with the number of imaged events being less due to the efficiency of the imaging code.

Due to the significant computational demands of these simulations, the results presented are for zero xy separation to increase the statistics and reduce run times. These results also provide an insight into the potential of this system with the addition of a full deconvolution algorithm. In the same vein as the earlier work, all reconstructions are displayed as an xy slice projected at 120 mm from the rear of the detector, in addition to a fit to the highest intensity slice through both x and y directions. The fit consists of a Lorentzian combined with a quadratic background and is described in more details in Section 4.3. Error bars are displayed for the number of counts in each reconstructed data point.

Figures 5.6 – 5.8 present the results for the Compton reconstruction, with the values extracted from the fits to these reconstructions given in Table 5.1. Figure 5.6 presents the results for a detector with a 'perfect' energy resolution of 0 keV. The source was found to be located at (x,y) = (428,431) mm, with the actual source location set at (x,y) = (430,430) mm. The resolution of the fit in both x and y was calculated to be FWHM$_x$ = 93 mm and FWHM$_y$ = 73 mm. The results for an energy resolution of 3 keV are shown in Figure 5.7, with the centroid of the

reconstruction located at (x,y) = (429,430) mm. The resolution in x was calculated to be FWHM_x = 99 mm, with the resolution in y calculated as FWHM_y = 65 mm. Finally, the results for Δ E = 50 keV are presented in Figure 5.8, with the reconstructed source located at (x,y) = (429,430) mm. The x and y fits returned values of FWHM_x = 93 mm and FWHM_y = 54 mm respectively.

The results of all of these simulations returned very precise source locations, with all three reconstructed source locations deviating from the known location by less than 2 mm in x and 1 mm in y. This shows that the energy resolution of the detecting medium has no noticeable effect on the centroid of the reconstructed image. This is to be expected since the energy only determines the angle of the reconstructed cone and has nothing to do with the axis of the reconstruction.

The resolution of the image also appears to show no real improvement as the energy resolution increases. The numbers presented in Table 5.1 appear to suggest that the position resolution in y improves as the energy resolution degrades. This is clearly non-physical and if we take a closer look at the fit applied to the y slice for both ΔE = 3 keV and δE = 50 keV, we can clearly see that the background component of the fit arcs much more than it should resulting in a much narrower peak when calculating the FWHM. The effects of this can be seen if we observe the residual line near the edges of the fit. The difference between the total fit and the actual data increases drastically as we move away from the source, indicating that the background fit is not as accurately determined as the energy resolution degrades.

5.2.2 Position Resolution

Similarly to those performed for the energy resolution, three simulations were ran for varying position resolution. Each simulation was ran using a γ-ray energy of 778 keV, with a fixed energy resolution of 5 keV. As before, the detector geometry was defined as two planar detectors stacked one behind the other, each measuring $60 \times 60 \times 10$ mm. For these simulations, three voxel sizes were tested; 1 mm^3, 2 mm^3 and 5 mm^3. This simulated the difference between imaging with the natural

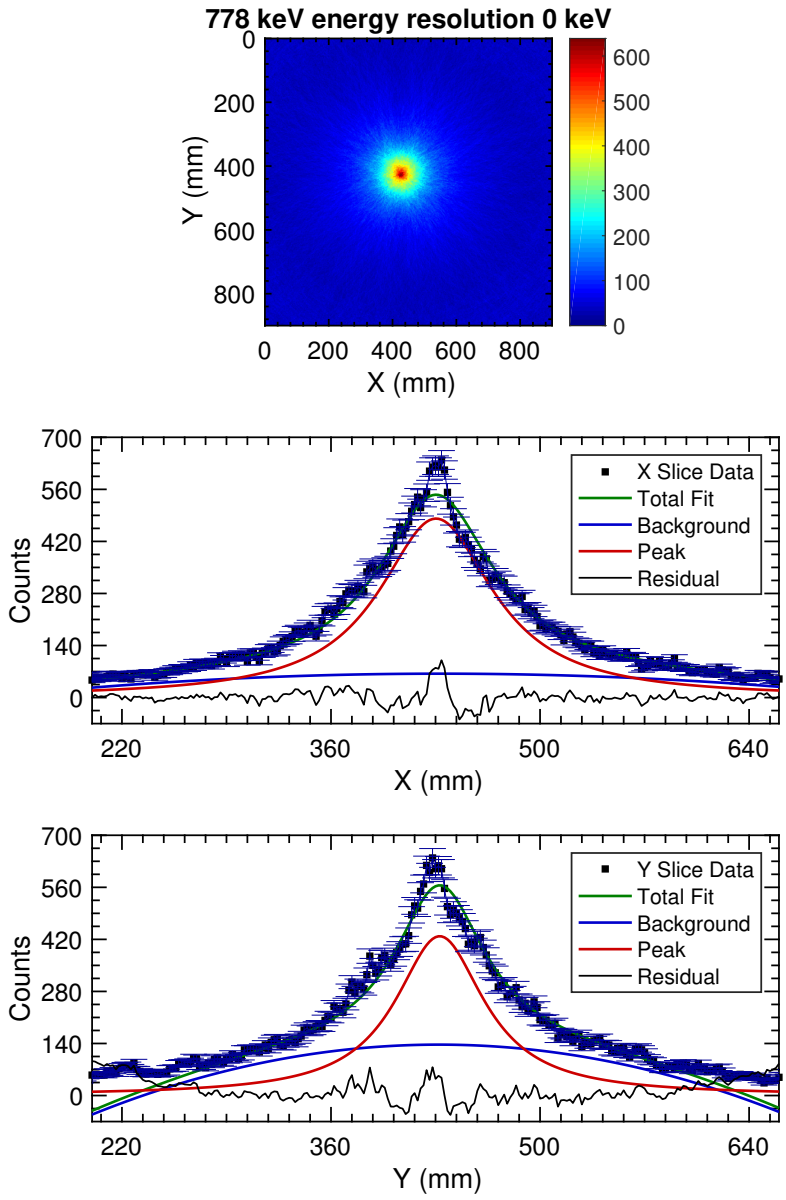

Figure 5.6: Compton image reconstruction for a simulated γ-ray energy of 778 keV, with ΔE = 0 keV and Δpos_{xy} = 2 mm, Δpos_z = 10 mm. A cross section of the reconstruction at z = 120 mm is shown in addition to a slice through the highest intensity region in both X (middle) and Y (bottom). A Lorentzian plus a quadratic background is fitted to the data with a residual calculated for the difference between the data and the fit.

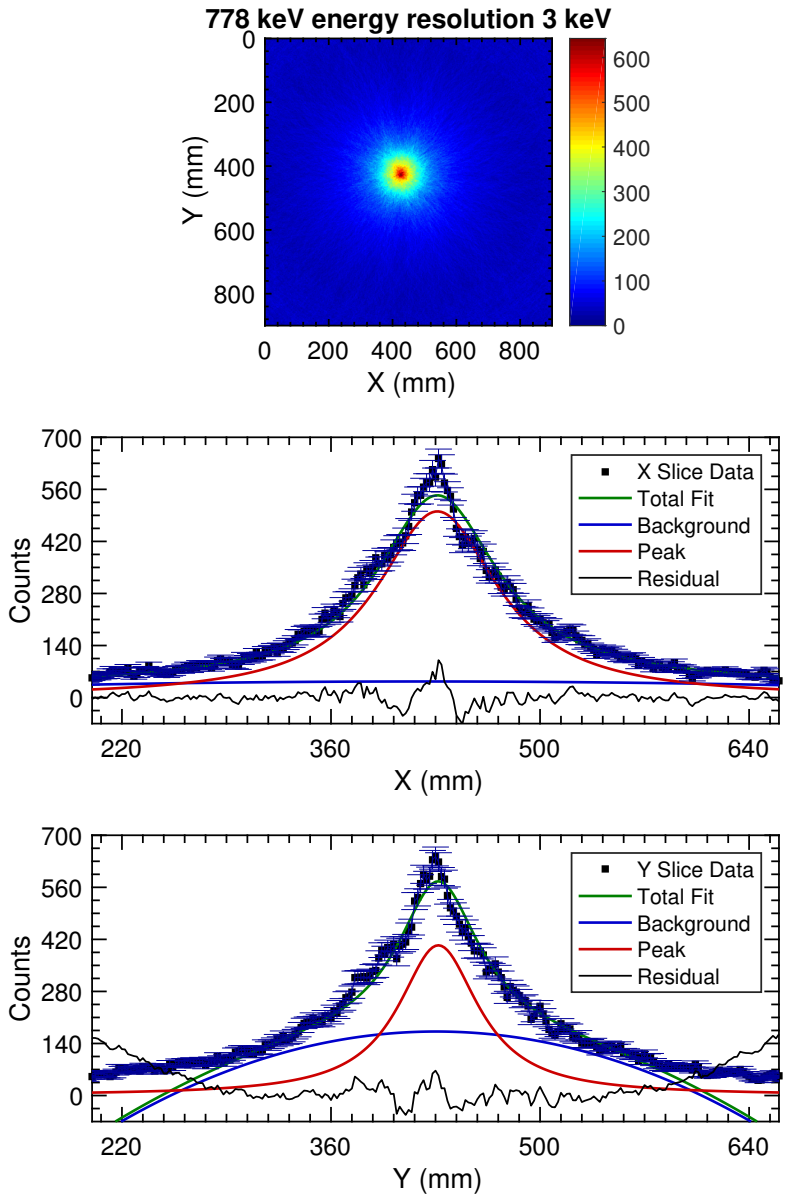

Figure 5.7: Compton image reconstruction for a simulated γ-ray energy of 778 keV, with ΔE = 3 keV and Δpos_{xy} = 2 mm, Δpos_z = 10 mm. A cross section of the reconstruction at z = 120 mm is shown in addition to a slice through the highest intensity region in both X (middle) and Y (bottom). A Lorentzian plus a quadratic background is fitted to the data with a residual calculated for the difference between the data and the fit.

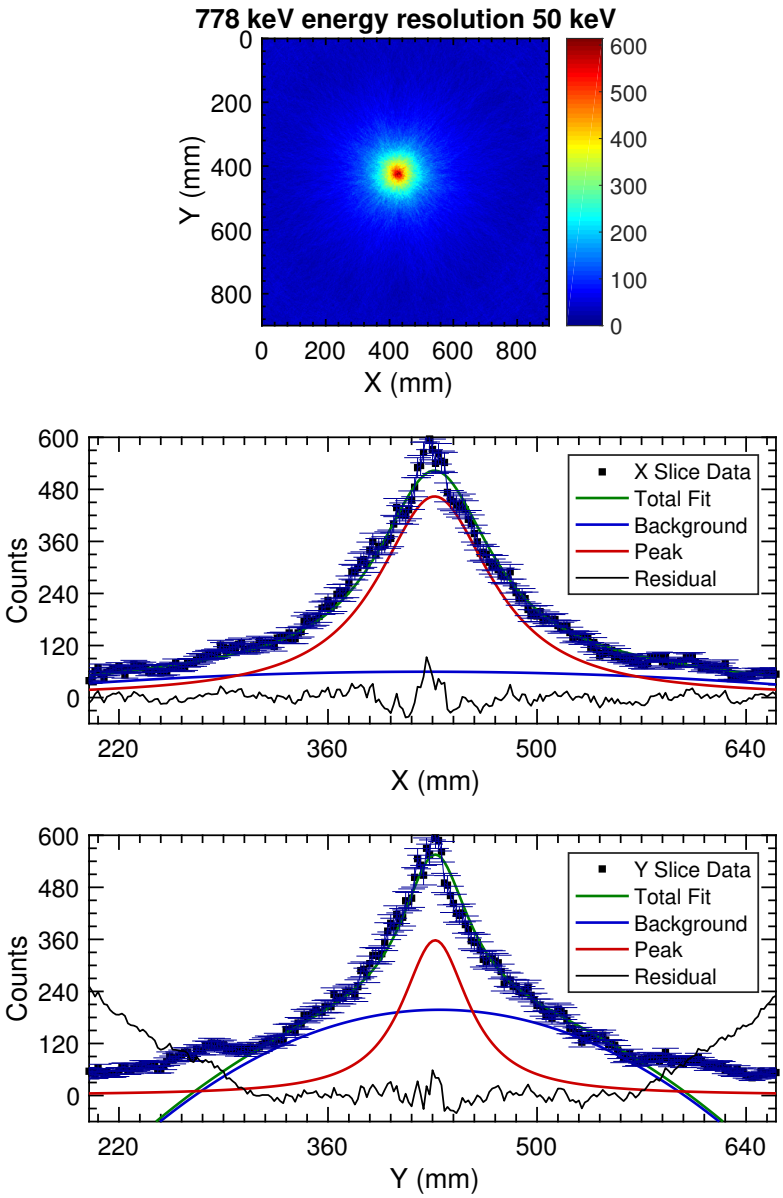

Figure 5.8: Compton image reconstruction for a simulated γ-ray energy of 778 keV, with ΔE = 50 keV and Δpos_{xy} = 2 mm, Δpos_z = 10 mm. A cross section of the reconstruction at z = 120 mm is shown in addition to a slice through the highest intensity region in both X (middle) and Y (bottom). A Lorentzian plus a quadratic background is fitted to the data with a residual calculated for the difference between the data and the fit.

Table 5.2: Summary of Compton image reconstruction results for position resolution simulations for an initial γ-ray energy of 778 keV

Δp (mm^3)	Δx (mm)	Δy (mm)	x,y (mm)	Δx,y (mm)
1	27	29	(430,430)	(0, 0)
2	38	37	(429,431)	(-1, +1)
5	99	88	(423, 432)	(-7, +2)

position resolution afforded by the detector segmentation (5 mm) and the improved position resolution gained by using techniques such as PSA.

Figures 5.9 – 5.11 present the results for the Compton reconstruction, with the values extracted from the fits to these reconstructions given in Table 5.2. Figure 5.9 presents the results for a detector with a position resolution resolution of 1 mm, which is near the theoretical limits for a germanium semiconductor detector [24]. The source was found to be located at (x,y) = (430,430) mm, which matches perfectly with the known source location set at (x,y) = (430,430) mm. The resolution of the fit in both x and y was calculated to be FWHM$_x$ = 27 mm and FWHM$_y$ = 29 mm. The results for a position resolution of 2 mm are shown in Figure 5.10, with the centroid of the reconstruction located at (x,y) = (429,431) mm. The resolution in x was calculated to be FWHM$_x$ = 38 mm, with the resolution in y calculated as FWHM$_y$ = 37 mm. Finally, the results for a voxel size of 5 mm^3 are presented in Figure 5.11, with the reconstructed source located at (x,y) = (423,432) mm. The x and y fits returned values of FWHM$_x$ = 99 mm and FWHM$_y$ = 88 mm respectively.

These results show much more variation than those presented for the energy resolution, with both the source location and also position resolution improving as the voxel size decreases. The reconstruction of the source location degraded as the position sensitivity decreased, with the 1mm resolution perfectly reconstructing source position, whereas the 5 mm results were off by 7 mm in x and 2 mm in y. This result is to be expected since the positions of the two interactions determine the axis with which the reconstruction is performed on. With a finer grid, the

positions of the interactions can be better located, thus enabling the cones to be projected in the correct plane. In combination with the source location results from earlier, it is clear the the position resolution has a much larger effect of the reconstructed location than the energy resolution of the detector.

In addition to the accuracy of the source location, the position resolution in both x and y improves drastically from 5 mm to 1 mm position resolution. From a qualitative standpoint, the reconstructed image in Figure 5.11 appears much more diffuse than those in Figures 5.9 and 5.10. The fits to the data are consistent for all simulations, with excellent agreement between the total fit and real data for all values of x and y, providing more confidence in the validity of the extracted parameters. In terms of the FWHM of the fit, the values for the 1 mm simulation are $\sim$1/3 of those calculated for the 5 mm simulation. This is an enormous improvement, and a clear indication that the position resolution of the detector is the most significant parameter for improving performance in this system.

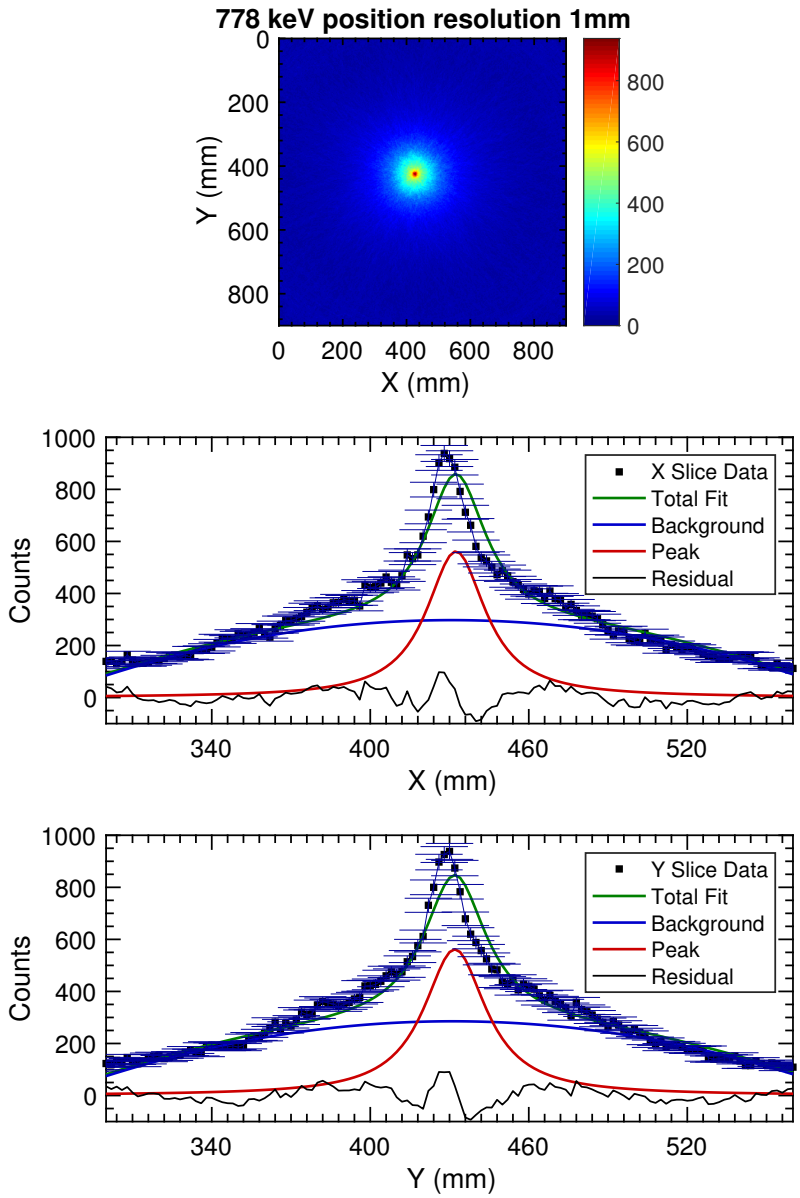

Figure 5.9: Compton image reconstruction for a simulated γ-ray energy of 778 keV, with ΔE = 5 keV and Δpos_{xyz} = 1 mm. A cross section of the reconstruction at z = 120 mm is shown in addition to a slice through the highest intensity region in both X (middle) and Y (bottom). A Lorentzian plus a quadratic background is fitted to the data with a residual calculated for the difference between the data and the fit.

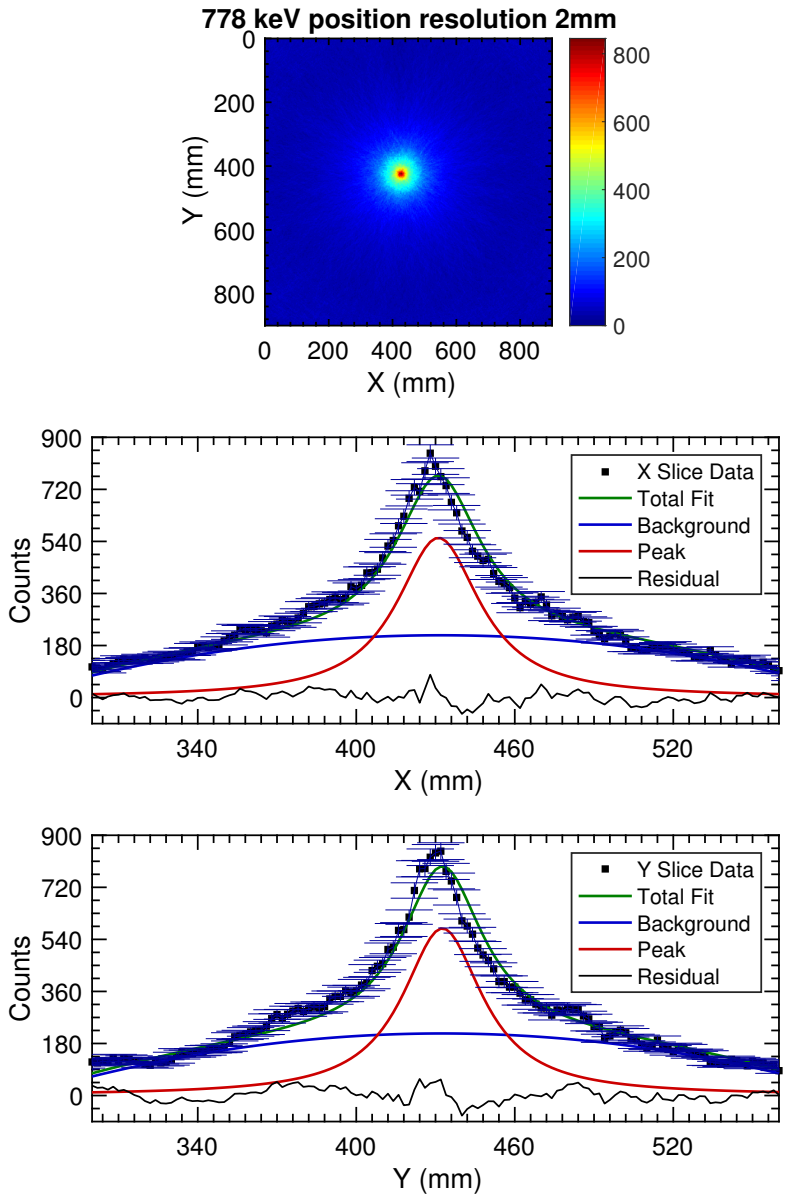

Figure 5.10: Compton image reconstruction for a simulated γ-ray energy of 778 keV, with ΔE = 5 keV and Δpos_{xyz} = 2 mm. A cross section of the reconstruction at z = 120 mm is shown in addition to a slice through the highest intensity region in both X (middle) and Y (bottom). A Lorentzian plus a quadratic background is fitted to the data with a residual calculated for the difference between the data and the fit.

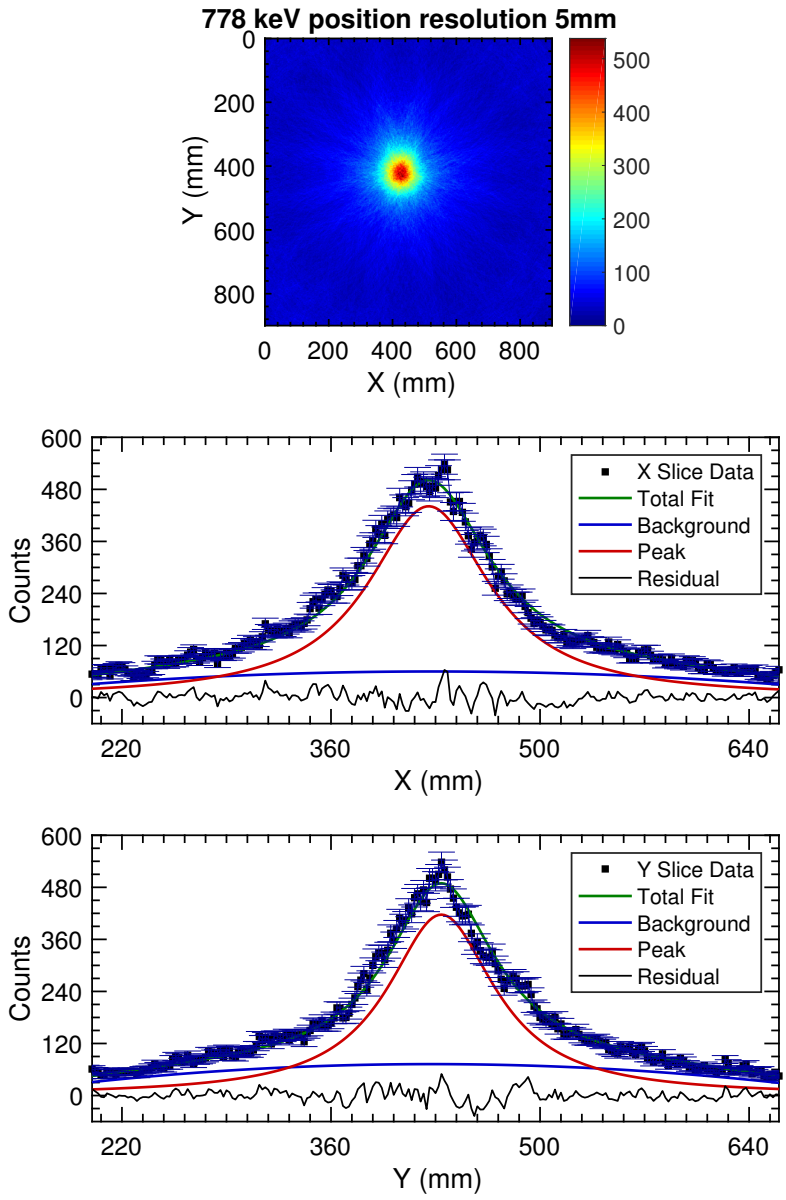

Figure 5.11: Compton image reconstruction for a simulated γ-ray energy of 778 keV, with ΔE = 5 keV and Δpos_{xyz} = 5 mm. A cross section of the reconstruction at z = 120 mm is shown in addition to a slice through the highest intensity region in both X (middle) and Y (bottom). A Lorentzian plus a quadratic background is fitted to the data with a residual calculated for the difference between the data and the fit.

6 Conclusion

The feasibility of single element Compton imaging using a DSGSD has been examined. The results generated with the raw detector information struggled to correctly reproduce the source location, with multiple hotspots generated for a single source. The causes of these features have been examined and are understood to be a consequence of poor depth information. The effects of applying PSA have also been studied, with the initial results looking promising. The reconstructed images correctly reproduce the source location, to within a few mm, however the position resolution of the final image is still relatively poor. This should be improved in future work as the selection criteria are reduced.

Experimental measurements were taken using a DSGSD with digital electronics to enable storage of pulse shapes from each detector strip. Throughout the experimental run, results were taken for both ^{152}Eu and ^{60}Co, enabling a wide spread of γ-ray energies to be studied. The data were subsequently sorted to locate events of interest.

Detailed electric field simulations were performed, followed by a Monte Carlo simulation to simulate the charge collection for interactions occurring at different positions within the detector. Using this, a simulated pulse shape database has been generated using the ADL software package down to a 1 mm grid size. Comparisons between experimental and simulated pulses have been made using a grid search algorithm to improve the position sensitivity of the detector, thus improving the position resolution of the reconstructed images.

Additionally, simulations have been performed using the simulation package GAMOS, to determine the expected response of the detector with and without the application of PSA. Results from these simulations were found to be in agreement with the experimental data. In addition, simulations were performed to study the features present in the reconstructed images, with excellent agreement between the theoretical interpretation and the simulated results.

Finally, the effects of varying energy and position resolution have been studied using an adaptation of the GAMOS model used earlier. The results of these sim-

ulations showed that the energy resolution has little effect on the reconstructed location, however it does have an effect on the background spread of the image, resulting in difficulties when trying to apply a fit to the data. The position resolution simulations displayed significant changes between the three voxel sizes chosen, with both the reconstructed source location and the resolution of the reconstructed image improving with reduced voxel size.

Future work should aim to remove the requirement for a strip separation of larger than 10 mm, working to develop a grid search algorithm capable of deconvolving pulses and image charges. This would dramatically improve the efficiency of the process, thus enabling use in decay spectroscopy experiments. In addition, longer experimental runs would provide greater statistics, enabling a lower FoM cutoff to be applied, further improving the position sensitivity.

In conclusion, the results of this experiment provide a solid grounding for future work on this project, with the prospects of single element Compton imaging using a DSGSD looking promising. The concept has been proved viable, with further work required to improve the efficiency of the process.

References

[1] P.J. Twin et al. Observation of a Discrete-Line Superdeformed Band up to $60\hbar$ in ^{152}Dy. *Phys. Rev. Lett.*, 57, 1986.

[2] S.W. Ødegård et al. Evidence for the Wobbling Mode in Nuclei. *Phys. Rev. Lett.*, 86:5866–5869, 2001.

[3] National Research Council. *Nuclear Physics: Exploring the Heart of Matter.* The National Academies Press, 2013.

[4] J. Simpson. The AGATA Project. *J. Phys. G*, 31:S1801, 2005.

[5] I.Y. Lee et al. GRETINA: A Gamma Ray Energy TrackINg Array. *Nucl. Phys. A*, 746:255c–259c, 2004.

[6] B. Rubio. Decay Spectroscopy (DeSpec) at the New FAIR-NuSTAR Facility. *Int. Jour. Mod. Phys. E*, 15:1979–1988, 2006.

[7] S. Moon et al. Compton Imaging with AGATA and SmartPET for DESPEC. *Journal of Instrumentation*, 12:C12048, 2012.

[8] H.C. Boston et al. Characterisation of the SmartPET Planar Germanium Detectors. *Nucl. Instr. Meth. A*, 579:104–107, 2007.

[9] H. Geissel et al. The Super-FRS Project at GSI. *Nucl. Intstr. Meth. Phys. B*, 204:71–85, 2003.

[10] NUSTAR. Technical Report for the Design, Construction and Commissioning of the DESPEC Germanium Array Spectrometer DEGAS, 2014. Online; accessed 10-Mar-2016.

[11] M. Doncel et al. Conceptual design of a high resolution Ge array with tracking and imaging capabilities for DESPEC (FAIR) experiment. *Journ. of Instr.*, 10:P06010, 2015.

[12] PHDS Co. GeGI, 2016.

[13] H3D. Polaris H, 2016.

[14] G.F. Knoll. *Radiation Detection and Measurement*. John Wiley and Sons, 4th edition, 2010.

[15] B. Bruyneel. Mobilities in Germanium. Available at `http://ns.ph.liv.ac.uk/EGAN/files/tuesday/Bruyneel-EGAN-School-P2`, 2011.

[16] W. Shockley. Currents to Conductors Induced by a Moving Point Charge. *J. Appl. Phys*, 9:635, 1938.

[17] S. Ramo. Currents Induced by Electron Motion. *Proceedings of the I.R.E*, September:584, 1939.

[18] R.B. Todd, J.M. Nightingale, and D.B. Everett. A Proposed Gamma Camera. *Nature*, 251:132–134, 1974.

[19] G.J. Schmid et al. Gamma-ray Compton Camera Imaging with a Segmented HPGe. *Nucl. Instr. Meth. A*, 459:565–576, 2001.

[20] T. Niedermayr et al. Gamma-ray Imaging with a Coaxial HPGe Detector. *Nucl. Instr. Meth. A*, 553:501–511, 2005.

[21] L. Mihailescu et al. SPEIR: A Ge Compton Camera. *Nucl. Instr. Meth. A*, 570:89–100, 2007.

[22] CAEN. CAEN Digitizer, 2015. Online; accessed 27-Dec-2015.

[23] CAEN. CAEN Digitizer, 2015. Online; accessed 27-Dec-2015.

[24] K. Vetter et al. Three-dimensional Position Sensitivity in Two-dimensionally Segmented HPGe Detectors. *Nucl. Instr. Meth. A*, 452:223–238, 2000.

[25] B. Bruyneel and B. Birkenbach. AGATA Detector Simulation Library (ADL) v 3.0. Available at `https://www.ikp.uni-koeln.de/research/agata/index.php?show=download`.

[26] B. Bruyneel, B. Birkenbach, and P. Reiter. Pulse shape analysis and position determination in segmented HPGe detectors: The AGATA detector library. *Eur. Phys. Jour. A*, 52:70, 2016.

[27] B. Birkenbach. Gamma ray Tracking with the AGATA Demonstrator - A Novel Approach for In-beam Spectroscopy. 2014.

[28] K. Vetter et al. Performance of the GRETA Prototype Detectors. *Nucl. Instr. Meth. A*, 452:105–114, 2000.

[29] Canberra UK. Private Communication, 2015.

[30] D.B. Everett et al. Gamma-radiation Imaging System Based on the Compton Effect. *Proc. IEE*, 124:995–1000, 1977.

[31] D.S. Judson. To Be Published.

[32] R.J. Cooper. Performance of the SmartPET Positron Emission Tomography System for Small Animal Imaging. page 148, 2007.

[33] P. Arce et al. GAMOS: a GEANT4 Based Easy and Flexible Framework for Nuclear Medicine Applications. *IEEE Nuclear Science Symposium Conference Record*, 53:3162–3168, 2008.

[34] S. Agostinelli et al. Geant4 - A Simulation Toolkit. *Nucl. Instr. Meth. A*, 506:250–303, 2003.

[35] J. Allison et al. Geant4 Developments and Applications. *IEEE Transactions of Nuclear Science*, pages 270–278.

A Simulation Code

```
#include "SIMION_Geometry_PLANAR.h"

//setup geometry
INTEGER PLANAR_G_TopContactDepth = 0;
INTEGER PLANAR_G_Height          = 0;
INTEGER PLANAR_G_BotContactDepth = 0;
INTEGER PLANAR_G_Spacing         = 0;
INTEGER PLANAR_G_ExtGroundWidth  = 0;
INTEGER PLANAR_G_StripWidth      = 0.0;
INTEGER PLANAR_G_StripGap        = 0.0;
INTEGER PLANAR_G_NumOfStrips     = 0.0;
INTEGER PLANAR_G_NumOfGaps       = 0.0;
DOUBLE PLANAR_G_ImpTop           = 0.0;
DOUBLE PLANAR_G_ImpBot           = 0.0;

INTEGER SIMION_Setup_GEOMETRY_PLANAR(char *filename_setupfile) {

        INTEGER i,len, err=1;
        DOUBLE temp=0;
        struct ADL_KEYWORD **Kwords;

        //get list of keywords from file:
        if (strlen(filename_setupfile)>1) {// if a filename is supplied, parse it
                Kwords = ADL_parse_file (filename_setupfile);

                //overwrite keywords with parsed values:
                //first scan for gridsize!
                len = Kwords[1]->linenumber;
                err = Kwords[len+2]->linenumber;
                for (i=0;i<len;i++) {
                        if (strcmp(Kwords[2+i]->keyword,"SIMION_G_GridSize")==0)
                                sscanf(Kwords[2+i]->svalue,"%lf",&SIMION_G_GridSize);
                        if (strcmp(Kwords[2+i]->keyword,"SIMION_G_Dimension")==0)
                                sscanf(Kwords[2+i]->svalue,"%i",&SIMION_G_Dimension);
                        if (strcmp(Kwords[2+i]->keyword,"SIMION_G_Voltage")==0)
                                sscanf(Kwords[2+i]->svalue,"%lf",&SIMION_G_Voltage);
                        if (strcmp(Kwords[2+i]->keyword,"SIMION_G_Description")==0)
                                sscanf(Kwords[2+i]->svalue,"%s",SIMION_G_Description);
                        if (strcmp(Kwords[2+i]->keyword,"SIMION_G_EpsScale")==0)
                                sscanf(Kwords[2+i]->svalue,"%lf",&SIMION_G_EpsScale);
                        if (strcmp(Kwords[2+i]->keyword,"SIMION_G_EpsExtScale")==0)
                                sscanf(Kwords[2+i]->svalue,"%lf",&SIMION_G_EpsExtScale);
                }
                for (i=0;i<len;i++) {
                        if (strcmp(Kwords[2+i]->keyword,"PLANAR_G_BotContactDepth")==0){
                                sscanf(Kwords[2+i]->svalue,"%lf",&temp);
                                PLANAR_G_BotContactDepth=SIMION_grid(temp, SIMION_G_GridSize);
                        }
                        if (strcmp(Kwords[2+i]->keyword,"PLANAR_G_Height")==0){
                                sscanf(Kwords[2+i]->svalue,"%lf",&temp);
                                PLANAR_G_Height=SIMION_grid(temp, SIMION_G_GridSize);
                        }
                        if (strcmp(Kwords[2+i]->keyword,"PLANAR_G_TopContactDepth")==0){
                                sscanf(Kwords[2+i]->svalue,"%lf",&temp);
                                PLANAR_G_TopContactDepth=SIMION_grid(temp, SIMION_G_GridSize);
                        }
                        if (strcmp(Kwords[2+i]->keyword,"PLANAR_G_Spacing")==0){
                                sscanf(Kwords[2+i]->svalue,"%lf",&temp);
                                PLANAR_G_Spacing=SIMION_grid(temp, SIMION_G_GridSize);
                        }
```

```
                        if (strcmp(Kwords[2+i]->keyword,"PLANAR_G_ExtGroundWidth")==0){
                                sscanf(Kwords[2+i]->svalue,"%lf",&temp);
                                PLANAR_G_ExtGroundWidth=SIMION_grid(temp, SIMION_G_GridSize);
                        }
                        if (strcmp(Kwords[2+i]->keyword,"PLANAR_G_NumOfStrips")==0){
                                sscanf(Kwords[2+i]->svalue,"%lf",&temp);
                                PLANAR_G_NumOfStrips=SIMION_grid(temp, 1);
                        }
                        if (strcmp(Kwords[2+i]->keyword,"PLANAR_G_NumOfGaps")==0){
                                sscanf(Kwords[2+i]->svalue,"%lf",&temp);
                                PLANAR_G_NumOfGaps=SIMION_grid(temp, 1);
                        }
                        if (strcmp(Kwords[2+i]->keyword,"PLANAR_G_StripWidth")==0){
                                sscanf(Kwords[2+i]->svalue,"%lf",&temp);
                                PLANAR_G_StripWidth=SIMION_grid(temp, SIMION_G_GridSize);
                        }
                        if (strcmp(Kwords[2+i]->keyword,"PLANAR_G_StripGap")==0){
                                sscanf(Kwords[2+i]->svalue,"%lf",&temp);
                                PLANAR_G_StripGap=SIMION_grid(temp, SIMION_G_GridSize);
                        }
                        if (strcmp(Kwords[2+i]->keyword,"PLANAR_G_ImpTop")==0)
                                sscanf(Kwords[2+i]->svalue,"%lf",&PLANAR_G_ImpTop);
                        if (strcmp(Kwords[2+i]->keyword,"PLANAR_G_ImpBot")==0)
                                sscanf(Kwords[2+i]->svalue,"%lf",&PLANAR_G_ImpBot);
                }
        }
        return err;
}

struct SIMION_PA *SIMION_newPA_PLANAR(void){
        //adding 1.0 for taking care of indices (NX>imax) and 0.5 for correct rounding
        INTEGER npot=3;
        INTEGER NX=2*PLANAR_G_ExtGroundWidth + 2*PLANAR_G_Spacing + PLANAR_G_NumOfStrips*
            ↪ PLANAR_G_StripWidth + PLANAR_G_NumOfGaps*PLANAR_G_StripGap + 0.5;
        INTEGER NY=2*PLANAR_G_ExtGroundWidth + 2*PLANAR_G_Spacing + PLANAR_G_NumOfStrips*
            ↪ PLANAR_G_StripWidth + PLANAR_G_NumOfGaps*PLANAR_G_StripGap + 0.5;
        INTEGER NZ=PLANAR_G_BotContactDepth + PLANAR_G_Height + PLANAR_G_TopContactDepth +
            ↪ 0.5;
        struct SIMION_PA * pa = new_SIMION_PA(SIMION_G_Description, npot, SIMION_G_GridSize,
            ↪ NX, NY, NZ);
        return pa;
}

INTEGER SIMION_CalcPoint_PLANAR(INTEGER nx, INTEGER ny, INTEGER nz, INTEGER i){
        if (i>2*PLANAR_G_NumOfStrips && i!=0)
        {
                printf("\nWARNING_IN_SIMION_CalcPoint_PLANAR:_Wrong_contact_number!_%i_\n", i)
                    ↪ ;
        }
        INTEGER j;
        for(j=0;j<PLANAR_G_NumOfStrips;j++){
                INTEGER k = j+12;

                //----------DEFINES FRONT PANEL OF CASING----------------//
                if(     nz < PLANAR_G_BotContactDepth + PLANAR_G_Height +
                    ↪ PLANAR_G_TopContactDepth &&
                        ny < PLANAR_G_ExtGroundWidth)
                        return EXT_GROUND;
                //----------DEFINES LEFT PANEL OF CASING-----------------//
                else if(nz < PLANAR_G_BotContactDepth + PLANAR_G_Height +
                    ↪ PLANAR_G_TopContactDepth &&
                        ny >= PLANAR_G_ExtGroundWidth &&
                        ny < PLANAR_G_ExtGroundWidth + 2*PLANAR_G_Spacing +
```

```
            ↪ PLANAR_G_NumOfStrips*PLANAR_G_StripWidth + PLANAR_G_NumOfGaps*
            ↪ PLANAR_G_StripGap &&
        nx < PLANAR_G_ExtGroundWidth)
        return EXT_GROUND;
//----------DEFINES BACK PANEL OF CASING----------//
else if(nz < PLANAR_G_BotContactDepth + PLANAR_G_Height +
    ↪ PLANAR_G_TopContactDepth &&
        ny >= PLANAR_G_ExtGroundWidth + 2*PLANAR_G_Spacing +
            ↪ PLANAR_G_NumOfStrips*PLANAR_G_StripWidth + PLANAR_G_NumOfGaps*
            ↪ PLANAR_G_StripGap)
        return EXT_GROUND;
//----------DEFINES RIGHT PANEL OF CASING----------//
else if(nz < PLANAR_G_BotContactDepth + PLANAR_G_Height +
    ↪ PLANAR_G_TopContactDepth &&
        ny >= PLANAR_G_ExtGroundWidth &&
        ny < PLANAR_G_ExtGroundWidth + 2*PLANAR_G_Spacing +
            ↪ PLANAR_G_NumOfStrips*PLANAR_G_StripWidth + PLANAR_G_NumOfGaps*
            ↪ PLANAR_G_StripGap &&
        nx >= PLANAR_G_ExtGroundWidth + 2*PLANAR_G_Spacing +
            ↪ PLANAR_G_NumOfStrips*PLANAR_G_StripWidth + PLANAR_G_NumOfGaps*
            ↪ PLANAR_G_StripGap)
        return EXT_GROUND;

//---------DEFINES LEFT SPACING----------//
else if(nz < PLANAR_G_BotContactDepth + PLANAR_G_Height +
    ↪ PLANAR_G_TopContactDepth &&
        nx >= PLANAR_G_ExtGroundWidth &&
        nx < PLANAR_G_ExtGroundWidth + PLANAR_G_Spacing &&
        ny >= PLANAR_G_ExtGroundWidth &&
        ny < PLANAR_G_ExtGroundWidth + 2*PLANAR_G_Spacing +
            ↪ PLANAR_G_NumOfStrips*PLANAR_G_StripWidth + PLANAR_G_NumOfGaps*
            ↪ PLANAR_G_StripGap)
        return OUTSIDE;
//---------DEFINES RIGHT SPACING----------//
else if(nz < PLANAR_G_BotContactDepth + PLANAR_G_Height +
    ↪ PLANAR_G_TopContactDepth &&
        nx >= PLANAR_G_ExtGroundWidth + PLANAR_G_Spacing +
            ↪ PLANAR_G_NumOfStrips*PLANAR_G_StripWidth + PLANAR_G_NumOfGaps*
            ↪ PLANAR_G_StripGap &&
        nx < PLANAR_G_ExtGroundWidth + 2*PLANAR_G_Spacing +
            ↪ PLANAR_G_NumOfStrips*PLANAR_G_StripWidth + PLANAR_G_NumOfGaps*
            ↪ PLANAR_G_StripGap &&
        ny >= PLANAR_G_ExtGroundWidth &&
        ny < PLANAR_G_ExtGroundWidth + 2*PLANAR_G_Spacing +
            ↪ PLANAR_G_NumOfStrips*PLANAR_G_StripWidth + PLANAR_G_NumOfGaps*
            ↪ PLANAR_G_StripGap)
        return OUTSIDE;
//---------DEFINES FRONT SPACING----------//
else if(nz < PLANAR_G_BotContactDepth + PLANAR_G_Height +
    ↪ PLANAR_G_TopContactDepth &&
        ny >= PLANAR_G_ExtGroundWidth &&
        ny < PLANAR_G_ExtGroundWidth + PLANAR_G_Spacing &&
        nx >= PLANAR_G_ExtGroundWidth + PLANAR_G_Spacing &&
        nx < PLANAR_G_ExtGroundWidth + PLANAR_G_Spacing + PLANAR_G_NumOfStrips
            ↪ *PLANAR_G_StripWidth + PLANAR_G_NumOfGaps*PLANAR_G_StripGap)
        return OUTSIDE;
//---------DEFINES REAR SPACING----------//
else if(nz < PLANAR_G_BotContactDepth + PLANAR_G_Height +
    ↪ PLANAR_G_TopContactDepth &&
        ny >= PLANAR_G_ExtGroundWidth + PLANAR_G_Spacing +
            ↪ PLANAR_G_NumOfStrips*PLANAR_G_StripWidth + PLANAR_G_NumOfGaps*
            ↪ PLANAR_G_StripGap &&
        ny < PLANAR_G_ExtGroundWidth + 2*PLANAR_G_Spacing +
```

```
                    ↪ PLANAR_G_NumOfStrips*PLANAR_G_StripWidth + PLANAR_G_NumOfGaps*
                    ↪ PLANAR_G_StripGap &&
                nx >= PLANAR_G_ExtGroundWidth + PLANAR_G_Spacing &&
                nx < PLANAR_G_ExtGroundWidth + PLANAR_G_Spacing + PLANAR_G_NumOfStrips
                    ↪ *PLANAR_G_StripWidth + PLANAR_G_NumOfGaps*PLANAR_G_StripGap)
                return OUTSIDE;

            //----------DEFINING BOTTOM CONTACT STRIPS-------//
            else if(nz < PLANAR_G_BotContactDepth &&
                nx >= PLANAR_G_ExtGroundWidth + PLANAR_G_Spacing + (j+1)*
                    ↪ PLANAR_G_StripWidth + j*PLANAR_G_StripGap &&
                nx < PLANAR_G_ExtGroundWidth + PLANAR_G_Spacing + (j+1)*
                    ↪ PLANAR_G_StripWidth + (j+1)*PLANAR_G_StripGap &&
                ny >= PLANAR_G_ExtGroundWidth + PLANAR_G_Spacing &&
                ny < PLANAR_G_ExtGroundWidth + PLANAR_G_Spacing + PLANAR_G_NumOfStrips
                    ↪ *PLANAR_G_StripWidth + PLANAR_G_NumOfGaps*PLANAR_G_StripGap)
                return BULK;
            else if(nz < PLANAR_G_BotContactDepth &&
                nx >= PLANAR_G_ExtGroundWidth + PLANAR_G_Spacing + j*
                    ↪ PLANAR_G_StripWidth + j*PLANAR_G_StripGap &&
                nx < PLANAR_G_ExtGroundWidth + PLANAR_G_Spacing + (j+1)*
                    ↪ PLANAR_G_StripWidth + j*PLANAR_G_StripGap &&
                ny >= PLANAR_G_ExtGroundWidth + PLANAR_G_Spacing &&
                ny < PLANAR_G_ExtGroundWidth + PLANAR_G_Spacing + PLANAR_G_NumOfStrips
                    ↪ *PLANAR_G_StripWidth + PLANAR_G_NumOfGaps*PLANAR_G_StripGap)
                if (i==j) return V_CONT;
                else if (j!=i && j<PLANAR_G_NumOfStrips) return V_CONT2;
                else return Z_CONT;
            //----------DEFINES BULK OF DETECTOR---GE CRSTAL----------//
            else if(nz >= PLANAR_G_BotContactDepth &&
                nz < PLANAR_G_BotContactDepth + PLANAR_G_Height)
                return BULK;
            //----------DEFINES TOP CONTACT STRIPS----------//
            else if(nz >= PLANAR_G_BotContactDepth + PLANAR_G_Height &&
                nz < PLANAR_G_BotContactDepth + PLANAR_G_Height +
                    ↪ PLANAR_G_TopContactDepth &&
                ny >= PLANAR_G_ExtGroundWidth + PLANAR_G_Spacing + (j+1)*
                    ↪ PLANAR_G_StripWidth + j*PLANAR_G_StripGap &&
                ny < PLANAR_G_ExtGroundWidth + PLANAR_G_Spacing + (j+1)*
                    ↪ PLANAR_G_StripWidth + (j+1)*PLANAR_G_StripGap &&
                nx >= PLANAR_G_ExtGroundWidth + PLANAR_G_Spacing &&
                nx < PLANAR_G_ExtGroundWidth + PLANAR_G_Spacing + PLANAR_G_NumOfStrips
                    ↪ *PLANAR_G_StripWidth + PLANAR_G_NumOfGaps*PLANAR_G_StripGap)
                return BULK;
            else if(nz >=  PLANAR_G_BotContactDepth + PLANAR_G_Height &&
                nz < PLANAR_G_BotContactDepth + PLANAR_G_Height +
                    ↪ PLANAR_G_TopContactDepth &&
                ny >= PLANAR_G_ExtGroundWidth + PLANAR_G_Spacing + j*
                    ↪ PLANAR_G_StripWidth + j*PLANAR_G_StripGap &&
                ny < PLANAR_G_ExtGroundWidth + PLANAR_G_Spacing + (j+1)*
                    ↪ PLANAR_G_StripWidth + j*PLANAR_G_StripGap &&
                nx >= PLANAR_G_ExtGroundWidth + PLANAR_G_Spacing &&
                nx < PLANAR_G_ExtGroundWidth + PLANAR_G_Spacing + PLANAR_G_NumOfStrips
                    ↪ *PLANAR_G_StripWidth + PLANAR_G_NumOfGaps*PLANAR_G_StripGap)
                if (i==k) return Z_CONT2;
                else if (k!=i && k>=PLANAR_G_NumOfStrips) return Z_CONT;
                else return V_CONT2;
        }
}
DOUBLE SIMION_CalcCharge_PLANAR(INTEGER nx, INTEGER ny, INTEGER nz, INTEGER i){
        return PLANAR_G_ImpBot+(PLANAR_G_ImpTop-PLANAR_G_ImpBot)*((nz-PLANAR_G_Spacing-
            ↪ PLANAR_G_BotContactDepth-PLANAR_G_ExtGroundWidth)/PLANAR_G_Height);
}
```